BRNO UNIVERSITY OF TECHNOLOGY

VYSOKÉ UČENÍ TECHNICKÉ V BRNĚ

FACULTY OF MECHANICAL ENGINEERING

FAKULTA STROJNÍHO INŽENÝRSTVÍ

ENERGY INSTITUTE

ENERGETICKÝ ÚSTAV

DESIGN AND REALIZATION OF AN AERODYNAMIC TUNNEL FOR SPRAYING NOZZLES

NÁVRH A REALIZACE AERODYNAMICKÉHO TUNELU PRO ROZSTŘIKOVACÍ TRYSKY

MASTER'S THESIS

DIPLOMOVÁ PRÁCE

AUTHOR AUTOR PRÁCE	Bc. Ondřej Cejpek
SUPERVISOR VEDOUCÍ PRÁCE	prof. Ing. Jan Jedelský, Ph.D.

BRNO 2020

Zadání diplomové práce

Ústav:	Energetický ústav
Student:	**Bc. Ondřej Cejpek**
Studijní program:	Strojní inženýrství
Studijní obor:	Technika prostředí
Vedoucí práce:	**prof. Ing. Jan Jedelský, Ph.D.**
Akademický rok:	2019/20

Ředitel ústavu Vám v souladu se zákonem č.111/1998 o vysokých školách a se Studijním a zkušebním řádem VUT v Brně určuje následující téma diplomové práce:

Návrh a realizace aerodynamického tunelu pro rozstřikovací trysky

Stručná charakteristika problematiky úkolu:

Rozstřikovací trysky jsou často používány v aplikacích, kde dochází k proudění okolního prostředí, např. automobilní trysky, trysky v turbínových motorech a hořácích, v zemědělství apod. Předmětem práce je návrh malého aerodynamického tunelu, který umožní provoz trysek v proudícím vzduchu v příčném a souproudém uspořádání. Sprej z trysek bude v tunelu studován pomocí optických metod. Je nutné provést rešerši dostupných technických řešení tunelů pro studium trysek v proudícím vzduchu optickými metodami, vybrat vhodnou koncepci tunelu, provést koncepční návrh a následně výrobní dokumentaci. Po výrobě budou ověřeny vlastnosti tunelu.

Cíle diplomové práce:

1. Analýza publikovaných technických řešení tunelů pro studium rozstřikovacích trysek v proudícím vzduchu optickými metodami (provozní parametry, konstrukce, zkoumané problémy, použité optické metody) (teorie a přehled aerodynamických tunelů, databáze dostupných publikací)
2. Popis konstrukčních celků, které musí navrhovaný tunel obsahovat, kritéria návrhu pro jednotlivých sekcí a komponent
3. Možná technická řešení tunelu, výběr vhodné koncepce, důraz na návrh testovací sekce, polohování trysky a odlučování kapek před odtahem
4. Návrh malého otevřeného aerodynamického tunelu, který umožní provoz trysek v proudícím vzduchu v příčném a podélném uspořádání. Sprej z trysek bude v tunelu studován pomocí optických metod. Parametry budou dále upřesněny
5. Výpočet tlakové ztráty, výběr ventilátoru
6. Výběr komerčně dostupných a konstrukce zbylých komponent tunelu, výrobní dokumentace tunelu, ekonomická rozvaha
7. Detekce a odstranění případných problematických jevů (např. pulzace proudění vlivem nerovnoměrnosti dodávky ventilátorem, přítomnost lopatkové frekvence, vibrace indukované prouděním či nevyváženostím rotoru)
8. Návrh systému pro řízení tunelu a monitorování/měření provozních parametrů (výběr potřebných snímačů a aktuátorů, jejich umístění, osazení, zapojení, SW aplikace, volba HW komponent)
9. Konstrukční úpravy nastavení tunelu s ohledem na požadované provozní vlastnosti (rovnoměrnost rychlostního profilu, intenzita turbulence a fluktuací rychlosti, rozsah rychlosti proudění, odtah aerosolu)
10. Ověření vlastností tunelu, zejména proudové charakteristiky (rychlostní profil, intenzita turbulence, stanovení charakteristik tunelu / bezrozměrných kritéria). Ověření splnění specifikace (rozsah průtoků, tlaková ztráta)
11. Optimalizace optického přístupu a nastavení optických metod (PDA, VR vizualizace) pro měření sprejů v tunelu
12. Provedení a dokumentace ukázkových testů trysky s použitím vybrané optické metody
13. Sumarizace praktických zkušeností z provozu tunelu

Seznam doporučené literatury:

LEFEBVRE, A. H., a V. G. McDONELL, Atomization and sprays, CRC press, 2017.

ZHANG, Z., LDA Application Methods: Laser Doppler Anemometry for Fluid Dynamics, Springer, 2010.

URUBA, V., Turbulence, ČVUT Praha, Počet stran: 130, 2., přeprac. vyd., ISBN: 978-80-0105-600-4, EAN: 9788001056004, 2014.

SEIDEL, M., Construction 1976-1980, Design, manufacturing, calibration of the German-Dutch windtunel, Germany, 1982.

BRENNEN, Ch. E., Fundamentals of multiphase flow, Cambridge Univ. Press, 2005.

Termín odevzdání diplomové práce je stanoven časovým plánem akademického roku 2019/20

V Brně, dne

L. S.

doc. Ing. Jiří Pospíšil, Ph.D. ředitel ústavu	doc. Ing. Jaroslav Katolický, Ph.D. děkan fakulty

Summary

Working conditions of atomizers in engineering applications differ from those in laboratory, where the atomizers are tested. The usage of a wind tunnel can simulate more realistic conditions. The wind tunnel is used to investigate the atomizers in cross and co-flowing air stream. The investigation of a spray in the wind tunnel can bring an insight into the spray behaviour in cross and co-flow. The present master thesis deals with a design of a small-scale, low-speed wind tunnel for the experiments with sprays created by the pressure swirl atomizer with spill-line in cross and co-flow conditions. Many wind tunnel designs were proposed; however, the most suitable wind tunnel design for spray study is an open type wind tunnel in blow down arrangement with closed test section. The wind tunnel is composed of several sections and components; each component is designed to obtain a good flow quality in the test section. The spray is investigated by using Phase Doppler anemometry (PDA), Laser Doppler anemometry (LDA), Particle image velocimetry (PIV), and by high–speed imaging. These optical techniques pose particular design requirements on the wind tunnel. A design procedure of small-scale, low-speed wind tunnel is described, and the flow quality in the test section is verified. Velocity of the flow in the test section is in the range from 0 m/s to 40 m/s with turbulent intensity below 0.7%. In the chapter 7, high–speed visualization of a spray in cross-flow is presented. The flowing air changes the breakup length, cone angle, and spray shape. The smallest droplets are carried away by the flow.

Key words

Small-scale, low-speed, wind tunnel, wind tunnel design, spray in cross-flow, pressure swirl atomizer

Abstrakt

Pracovní podmínky atomizérů v reálných operacích v průmyslu a zemědělství se liší od podmínek laboratorních, ve kterých jsou atomizéry testovány. Částečné přiblížení k realističtějším podmínkám nám může poskytnout použití větrného tunelu. Větrný tunel se používá k simulaci okolního proudění. Studium spreje ve větrném tunelu nám poskytne realističtější představu o chování spreje. Tato diplomová práce se zabývá návrhem malého, nízko rychlostního větrného tunelu pro experimenty s tlakovými vířivými tryskami s obtokem v příčném a podélném proudění. Existuje mnoho typů větrných tunelů, ale jako nejvhodnější typ byl zvolen otevřený, výtlačný větrný tunel s uzavřenou testovací sekcí. Výhodou jsou jeho kompaktní rozměry, ochrana částí tunelu před kapičkami spreje a poměrně jednoduchý návrh. Konstrukce větrného tunelu se skládá z několika částí, každá část je zkonstruována tak, aby bylo dosaženo co nejlepší kvality proudu v testovací sekci. Sprej je zkoumán pomocí optických metod Fázové Dopplerovské anemometrie (PDA), Laserové Dopplerovské anemometrie (LDA), Integrální laserová anemometrie (PIV) a pomocí vysokorychlostního záznamu. Tyto optické metody kladou speciální požadavky na konstrukci tunelu, především na konstrukci testovací sekce, která musí umožňovat optický přístup ke spreji a musí být pro tyto měřící techniky uzpůsobena. Rychlost v testovací sekci se pohybuje v rozmezí 0 až 40 m/s s intenzitou turbulence pod 0,7 %. V závěru práce je ukázka vizualizace spreje, v příčném proudění, pomocí vysokorychlostní kamery. Okolní proudění mění rozpadovou vzdálenost spreje, úhel kužele spreje i jeho tvar. Dochází k vymývání menších kapek, které jsou unášeny okolním proudem.

Klíčová slova

Návrh větrného tunelu, sprej v příčném proudění, tlakové vířivé trysky

Bibliographic citations

CEJPEK, Ondřej. *Návrh a realizace aerodynamického tunelu pro rozstřikovací trysky* [online]. Brno, 2020 [cit. 2020-06-18]. Dostupné z: https://www.vutbr.cz/studenti/zav-prace/detail/124871. Diplomová práce. Vysoké učení technické v Brně, Fakulta strojního inženýrství, Energetický ústav. Vedoucí práce Jan Jedelský.

Affirmation

I declare that this master thesis is the result of my own work led by prof. Ing. Jan Jedelský, Ph.D and all used sources are duly listed in the bibliography.

Bc. Ondřej Cejpek

Acknowledgements

I would like to express my gratitude to prof. Ing. Jan Jedelský Ph.D for his guidance and cooperation during the wind tunnel design, construction, and testing. Many thanks also belong to my colleagues, Ing. Milan Malý and Ing. Marcel Sapík, who helped me to deal with difficulties during the wind tunnel design. Thanks to Ing. Jan Šíp for helping me with the Constant temperature anemometry (CTA) measurement and Guilherme Augusto D. da Silva for helping me with vibration measurement of the wind tunnel construction. I would like to thank to Roman Partyka for the manufacture of some wind tunnel parts.

I would also like to thank to my girlfriend and my family for support during my studies at Brno University of Technology and while writing this thesis.

The realization of the master thesis was supported by the project no. GA18-15839S funded by the Czech Science Foundation and the project “Computer Simulations for Effective Low-Emission Energy Engineering” funded as project No. CZ.02.1.01/0.0/0.0/16_026/0008392 by Operational Programme Research, Development and Education, Priority axis 1: Strengthening capacity for high-quality research

CONTENTS

INTRODUCTION

Wind tunnels have been used for more than a century. The size of a wind tunnel can range from several to tens of meters. Wind tunnels are used for fluid flow research of e.g. turbine blades, ground vehicles, aeroplane, wings, fluid-structure interaction, and investigation of sprays. Tests of ground vehicles in wind tunnels can lead to energy savings and better aerodynamic properties of vehicles. Some early designs of wind tunnels suffer from a bad flow quality in the test section and disability to operate at low flow speed. A good flow quality within the wind tunnel test section is required (uniform velocity profile, low turbulent intensity).

The aim of this master thesis is to design a small-scale, low-speed wind tunnel. The wind tunnel can be used for spray investigations under cross and co-flow conditions and also for almost any flow study, e.g. fluid structure interaction, investigations of a flow around models of aeroplanes, cars, etc. Different atomizers can be tested in the wind tunnel. In our particular case, the spray is produced by a pressure swirl atomizer. Cross and co-flowing air simulates the conditions in the combustion chambers of turbines and automotive engines where the pressure swirl atomizers are used. The behaviour of a liquid spray is influenced by a cross and co-flowing air. There is a streamwise deflection of a spray, smaller penetration height, and the ambient flow of air also affects the combustion process performance and thus can have a negative impact on the production of emissions. Results from the investigations can lead to fuel savings, better combustion efficiency, reduction of NOx, and better ignition. Wind tunnel experiments can provide a better understanding of the spray behaviour. The required velocity span in the combustion chamber is approximately in the range from 1 to 30 m/s.

The spray is examined by the optical measurement techniques, such as PDA, PIV, and it is recorded by a high–speed camera. These techniques impose some design criteria on the wind tunnel construction. The tunnel is designed to obtain a good flow quality in the test section. There are also special size requirements to fit the wind tunnel to the Spray research laboratory at Brno University of Technology.

The present master thesis is divided into seven chapters. In the first chapter, the optimal wind tunnel construction is selected, and the essential parts of the wind tunnels are described. The second chapter deals with optical measurement systems used for investigation of sprays in cross-flow; some problems dealing with measurements in the wind tunnel are outlined. Pressure swirl nozzles, sprays, and influence of different variables on the spray behaviour are generally described in the next chapter. A design procedure of the wind tunnel is described and the properties of the flow in the wind tunnel are tested. The alignment of some measurement systems for wind tunnel measurements is described. The images from high–speed camera are shown, and a simple analysis of results is made.

1 WIND TUNNELS

In [1], some types of wind tunnels are described; there are many variations in the wind tunnel designs. Some similarities can be found, and two basic wind tunnel concepts arise; closed and open wind tunnels. According to the concept of test section, the open and closed test section designs can be found. Some advantages and disadvantages of each wind tunnel design are outlined in this thesis as well as the use of these designs for various purposes. Weerasuriya et al. [2] investigated the influence of twisted wind flows on the pedestrian-level wind field. The boundary layer wind tunnel was used for this investigation; it is a closed return type. The maximum flow velocity of 25 m/s was obtained. The size of a test section of this wind tunnel was approximately 5 × 4 m. Different wind profiles were used to investigate the effect of twisted flows. The boundary layer wind tunnels simulate the boundary layer near the earth surface and are mainly used to investigate building aerodynamics. The large size of the wind tunnel test section is suitable to prevent a flow reflection from the sidewalls. Beard et al. [3] used the wind tunnel to investigate the behaviour of falling drop in water saturated air. This wind tunnel consists of a horizontal air conditioning system (to control the humidity and temperature in the wind tunnel) and a vertical flow system. The vacuum pump was used as a driving mechanism. Vaz et al. [4] compared analytical equations for starting performance of a small wind turbine, with results obtained by experiments in the wind tunnel. The open type wind tunnel with open test section of cross-section of 1 × 1 m was used. The maximum wind speed in the test section was 19 m/s with turbulence intensity of 0.3%. Gebbink et al. [5] used a closed high–speed wind tunnel for validating the aerodynamic performance predictions for model of a business jet. The test section of cross-section of 2 × 1.8 m was used with Mach number in the range from 0.2 to 1.3. The experiments at elevated pressure and temperature are possible in this wind tunnel. Cerpentieri et al. [6] studied the tracer dispersion downwind from a physical model of a landfill. The environmental wind tunnel was used for the investigation. This tunnel is similar to the boundary layer wind tunnel. Damak et al. [7] used an open-circuit subsonic wind tunnel to investigate a newly designed helical Bach rotor. Kalmbach et al. [8] studied the fluid structure interaction in water tunnel channel. Wind tunnels are a useful tool for investigations of various types of flows and are used to simulate certain flow conditions. The speed of the flow in the test section can be hypersonic, supersonic, subsonic, and transonic or low-speed. Wegner et al. [9] examined a supersonic wind tunnel to determine the sphere drag at supersonic speeds and low Reynolds number. Prakash [10] used a subsonic wind tunnel to evaluate the flow characteristics over a symmetrical airfoil. Many studies deal with the wind tunnel design, for example Arifuzzaman et al. [11] described a design of a subsonic open type wind tunnel. Liu et al. [12] designed a closed type wind tunnel with open test section and performed a wind tunnel analysis. Some studies are concerned with design and investigation of specific wind tunnel components, for example Bell et al. [13] investigated contraction designs for a low speed wind tunnel. The pressure distribution along the wall was computed and prediction of the flow behind the contraction was made. Fang et al. [14] compared numerical results with experimental data for square to square contraction. Influence of contraction ratio on flow behaviour was investigated. Research into flow straighteners, honeycombs, and screens for turbulence reduction is very frequently carried on. Bradshaw [15] investigated the effect of screens on boundary layers. Kulkarni et al. [16] described some design aspects of honeycomb and screen combination on turbulent intensity in the test section.

1.1 Wind tunnel concepts

The closed-loop wind tunnel is illustrated in Figure 1. The main feature of this design is that the airflow circulates inside the wind tunnel so the tunnel is a circuit. A closed-loop wind tunnel can be used for the investigation of fluid-structure interaction. The closed-loop wind tunnel design is not suitable for spray flow research because the produced fluid from the atomizer can damage the fan wheel or clog the screens in the settling chamber. Discharged fluid can also cause corrosion on the metal parts of the wind tunnel

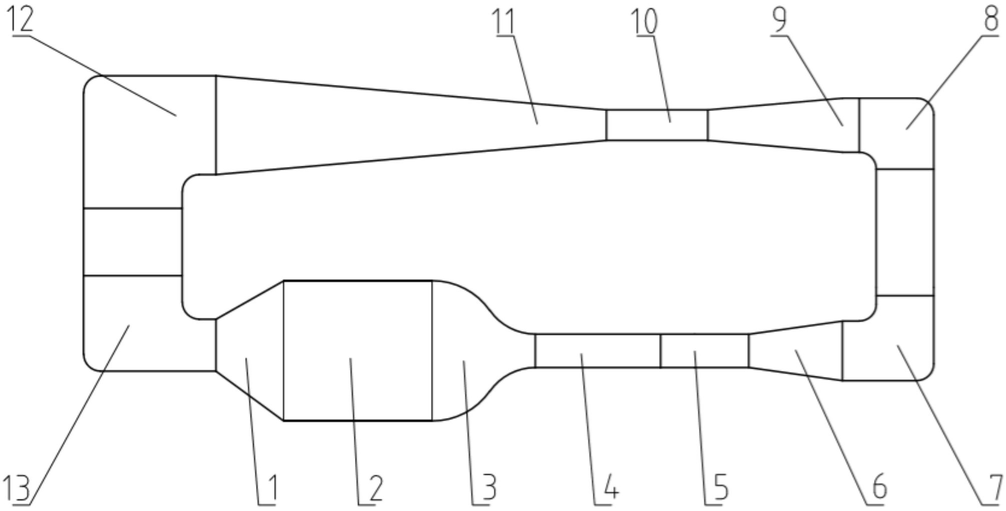

Figure 1 *Closed-loop wind tunnel, 1) Inlet diffuser, 2) Settling chamber, 3) Nozzle, 4) Laminarization section, 5) Test section, 6) Exit diffuser, 7) First corner, 8) Second corner, 9) Second nozzle, 10) Axial driving fan, 11) Diffuser, 12) Third corner, 13) Fourth corner*

Figure 2 illustrates the open-loop wind tunnel design. This design is simpler than the closed-loop wind tunnel because it contains fewer components. The driving fan position can differ from that seen in Figure 2. The driving fan is either placed on the windward side (blow-down wind tunnel) of the test section or on the leeward side of the test section (suck-down wind tunnel).

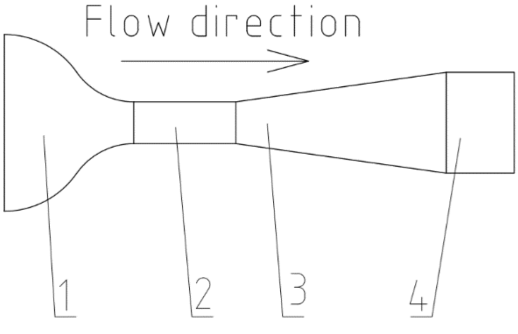

Figure 2 *Open-loop wind tunnel, 1) Nozzle, 2) Test section, 3) Diffuser, 4) Driving fan*

There are many wind tunnels that use pressurized air from a vessel as a driving mechanism. This design of the wind tunnel is illustrated in Figure 3. Some wind tunnels operate with high pressure or with increased temperature in the test section. Special safety requirements are imposed on the high pressure and temperature wind tunnels. High pressure and the desired velocity in the test section are usually maintained for a short period of time (diesel injection).

This design is not suitable for Spray research laboratory because it is not equipped with the pressure vessel of a sufficiently large size.

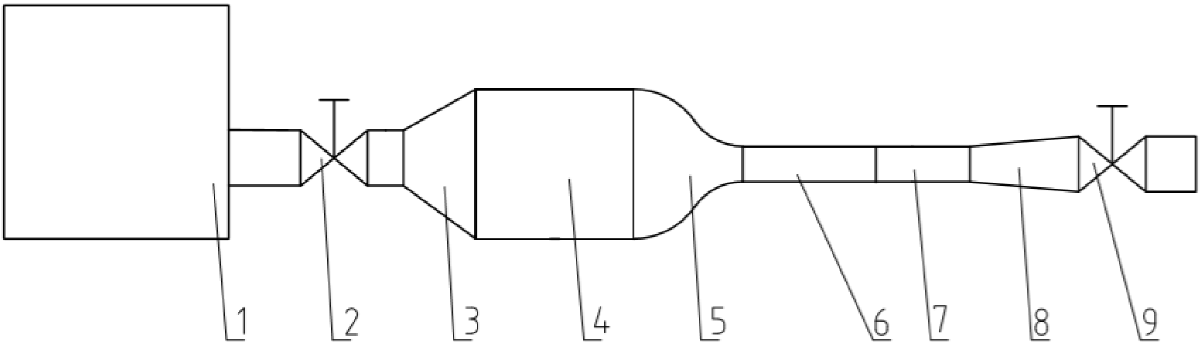

Figure 3 *Pressurized wind tunnel, 1) Pressure vessel, 2) Valve 1, 3) Inlet diffuser, 4) Settling chamber, 5) Nozzle, 6) Laminarization section, 7) Test section, 8) Exit diffuser, 9) Valve 2*

The most suitable wind tunnel design for spray research in Spray laboratory is the open-loop wind tunnel in blowdown arrangement. The design of this wind tunnel is shown in Figure 4.

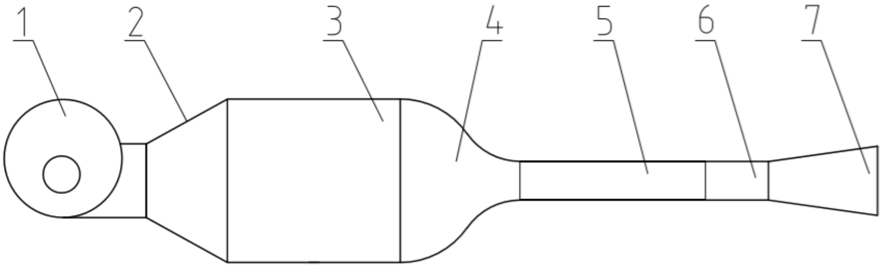

Figure 4 *Blowdown wind tunnel design, 1) Driving fan, 2) Entry diffuser, 3) Settling chamber, 4) Confusor, 5) Laminarization section, 6) Test section and 7) Exit diffuser.*

Basic wind tunnel classification is outlined in Figure 5.

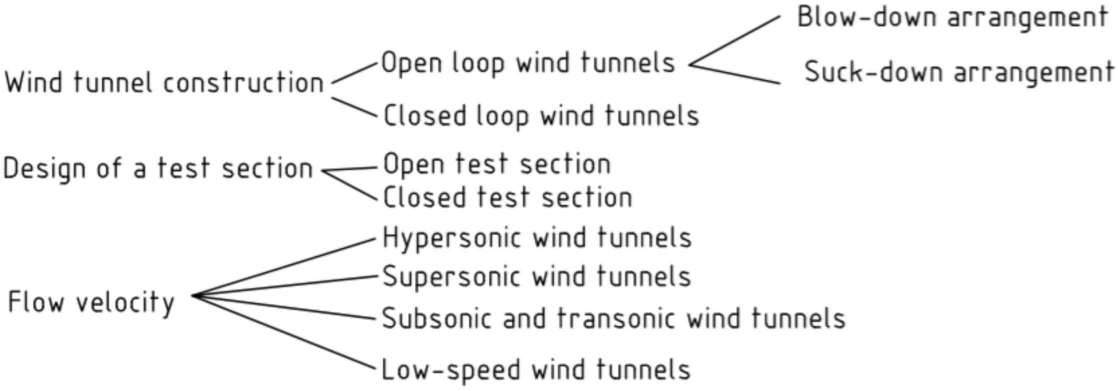

Figure 5 *Wind tunnel concepts*

1.2 Blowdown wind tunnel design

As was mentioned in the foregoing section, the blowdown wind tunnel is composed of several sections. The purpose of each wind tunnel section is to obtain required velocity conditions with uniform velocity profile and low turbulent intensity in the test section. Therefore, a precise design of each section is very important. There are many studies dealing with the blowdown wind tunnel design [17, 11].

Test section

The crucial part of wind tunnel is the test section. Uniform velocity profile and low turbulent intensity are required in this section. Main features of the test section are its cross-section and desired velocity (volume flux). In the test section, investigations of various flows take place. Intrusive or non-intrusive methods can be used to investigate the flow phenomena. A design of the test section depends on the type of simulated flow and investigated phenomenon and also on the experimental method used.

Laminarization section

This section helps with the final turbulent intensity reduction before it enters the test section. The laminarization section is designed with the identical cross-section as the test section to avoid vortex shedding on the connection of these sections. Length is normally designed as 10 times the hydraulic diameter of the section. In this component, the velocity profile is developed. The correct design of this section results in fully developed velocity profile in the test section. The design of laminarization section is illustrated in Figure 6.

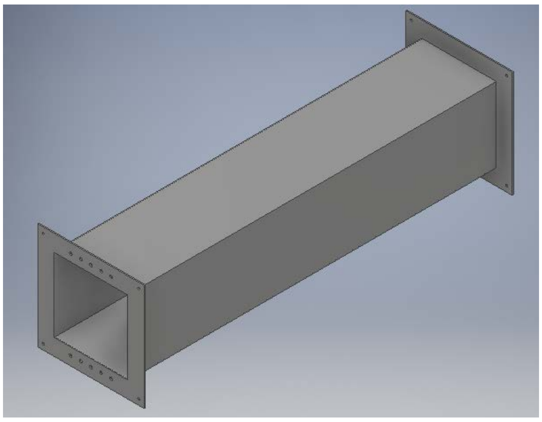

Figure 6 *Laminarization section design*

Confusor

The confusor is used to accelerate the flow and helps to suppress vortices in the flow; a higher velocity with a smaller turbulent intensity is obtained in the test section. Pressure distribution along confusor walls directly affects the boundary layer thickness, pressure losses, and non-uniformity of flow velocity through the test section [18]. Many problems with flow quality in the test section can arise from inappropriate confusor design. A combination of small contraction ratio (equation 1.2) together with small confusor length causes an increase in non-uniformity of the flow. The shape of the confusor is described by the equation 1.1. The shape of the confusor and parameters in equation 1.1 are described in Figure 7. The confusor design can be seen in Figure 8.

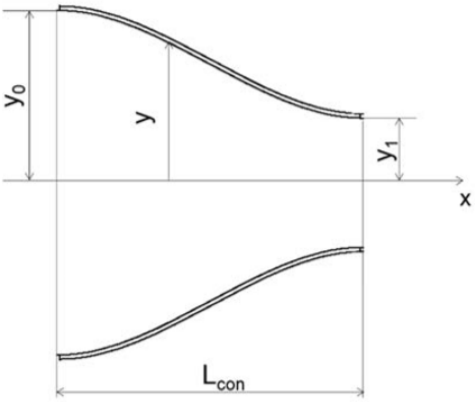

Figure 7 *Confusor shape [19]*

$$y = \frac{2(y_0 - y_1)}{L_{con}^3}x^3 + \frac{3(y_1 - y_0)}{L_{con}^2}x^2 + y_0 \tag{1.1}$$

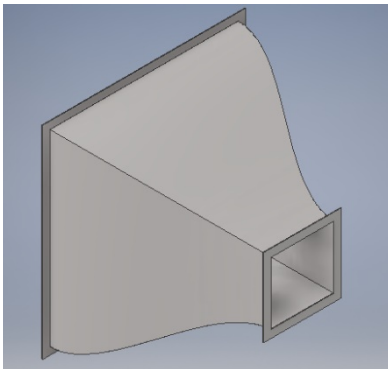

Figure 8 *Confusor design*

The parameter describing the nozzle is the contraction ratio defined by equation 1.2.

$$K = \frac{S_{in}}{S_{out}} \tag{1.2}$$

The larger is the contraction ratio, the higher is the velocity magnitude obtained at the cross-section output and the larger is the suppression of the vortices. According to [14, 20], $K = 9$ is sufficient to ensure a good flow quality in the test section.

Settling chamber

The settling chamber is a part of the wind tunnel where flow straighteners are placed. The cross-section of the settling chamber should be as large as possible to lower the velocity and pressure losses of flow straighteners. The length of the settling chamber is a function of number of flow straighteners.

Flow straighteners

Flow straighteners are an essential part of the wind tunnel. Two types of flow straighteners can be implemented in the wind tunnel (screens and honeycombs). Honeycombs reduce transverse fluctuations while screens reduce longitudinal fluctuations. A minimum distance between the flow straighteners is 0.2 × hydraulic diameter of the settling chamber. Many combinations of flow straighteners can be used. In [21], investigations of different combinations of flow straighteners and the influence of the flow straighteners on the flow quality in the test section are presented.

Honeycomb

This device is placed at the inlet of the settling chamber. The purpose of the honeycomb is to reduce transverse velocity fluctuations. It has small, long holes within the body.

According to [22], the hole length of at least nine times the holes hydraulic diameter is recommended. The honeycomb is made of light and durable material. In small wind tunnels, honeycombs are manufactured by 3D printer while in the large wind tunnels, honeycombs are usually made of wood or aluminium sheets. The design of the honeycomb is illustrated in Figure 9.

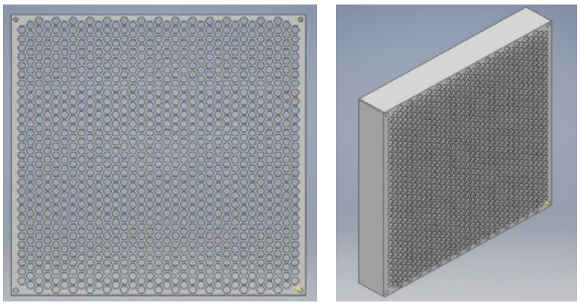

Figure 9 *Honeycomb design*

Screens

Screens are used to reduce longitudinal fluctuations. An important screen parameter is the screen solidity σ [-] defined by equation 1.4.

$$\sigma = \frac{S_{free}}{S_{all}} \tag{1.4}$$

For a proper function of the screen, the solidity must be kept below 0.5 ($\sigma \leq 0.5$). It is convenient to combine more screens with different solidity [23].

Pressure loss of the flow straightener can be computed by equation 1.5.

$$\Delta p = K_s \rho \frac{v^2}{2} \tag{1.5}$$

Pressure loss coefficient K_s for honeycomb, screen, and a combination of both can be found in [24, 25]. According to [21], the difference between the value of K_s predicted by theory and by experimental measurement can be up to 50%.

The flow in the settling chamber acts on the screens. Vibration can cause flow disturbances and additional turbulence. The wire in the screens should be tough, should not vibrate, and a tough connection with frames should be designed. If the solidity of the screen is higher than 0.5, screens can generate turbulence. The design of the screen can be seen in Figure 10.

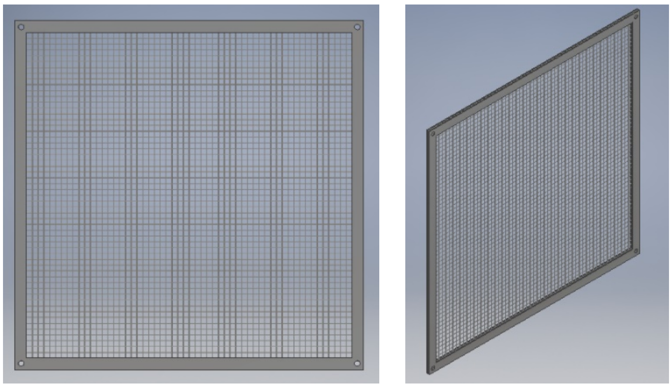

Figure10 *Design of screens*

Inlet diffuser

The inlet diffuser connects the cross-section of the driving fan with the cross-section of the settling chamber. When designing the diffuser, the key parameter is the length of the diffuser and the angle of inclination. The smaller is the angle, the larger is the length. When the length of a diffuser is not sufficiently large, the separation of the flow can be present in the diffuser. Flow separation has an adverse effect on the quality of the flow in the test section. Usually, the angle of inclination is smaller than 9 °.

Driving fan

The heart of wind tunnel is a driving fan. Two types of fans are mainly used in the wind tunnels; axial or radial fans.

For the proper design of the fan, the required volume flux (velocity) in the test section and pressure losses of the wind tunnel circuit are crucial. The driving fan influences the flow quality in the test section; it can cause pressure and velocity fluctuations of the flow. The turbulent intensity in the test section rises with the increase in velocity fluctuations. To reduce the velocity fluctuations, flow straighteners are used. The experiments are performed to investigate the influence of the fan on the flow quality (vane frequency).

In this chapter, components of blowdown wind tunnel were described. The design procedure of the blowdown wind tunnel with special requirements on the tunnel design is presented in chapter 4. The traverse system of the wind tunnel, droplet separator, and other parts designed for investigation of sprays in cross-flow are additionally described.

2 MEASUREMENT TECHNIQUES

The test section of the wind tunnel is designed for investigations of sprays by non-intrusive optical techniques. LDA, PDA, PIV and high–speed imaging are described in the following section.

LDA measures the velocity of the seeding particles in the flow; PDA is able to measure the velocity and diameter of the seeding particles. Both techniques are pointwise techniques. The extension to a plane measurement of velocity is provided by the PIV method which is able to measure the instantaneous velocity in the plane and also the seeding particle diameter. By high–speed imaging, the information on the flow velocity and the particle diameter in plane can be derived.

2.1 Laser Doppler anemometry

LDA was first described in 1964 [26]. The invention of laser played a crucial role in the development of the LDA and PDA techniques. Over many decades, various systems of LDA were proposed and tested. One of the first commercial LDA systems was available in 1970 [27].

LDA measures the velocity of particles in the flow evaluated based on the light scattered by particles. The gas laser or solid-state laser are used as a generator of high–intensity monochromatic light. A laser source generates light of the specific wavelengths - 514.5 nm-green, 488 nm-blue, etc. The specific wavelength corresponds to the specific frequency. The receiver measures the frequency of light refracted by particles. The measured frequency is different than the frequency of the laser source. This difference (frequency shift) is caused by the velocity of the particle in the flow. This effect is well known as a Doppler effect. The principle of LDA can be explained in two ways; by the Doppler effect and by a fringe model.

2.1.1 Doppler effect

LDA and PDA measurement techniques work on the principle of Doppler effect illustrated in Figure 11. The vector U in Figure 11 represents the velocity of the particle, unite vectors e_i and e_s represent the incoming light and the scattered light to the receiver directions, respectively. The incoming light with frequency f_i impacts the particle with velocity of light c. The moving particle scatters the light with frequency f_s. The scattered light is shifted by frequency f_s, because of the movement of the particle. The frequency shift also known as the Doppler shift is proportional to the particle velocity U. Light is scattered by the particle to all directions, but only the direction to the receiver is considered.

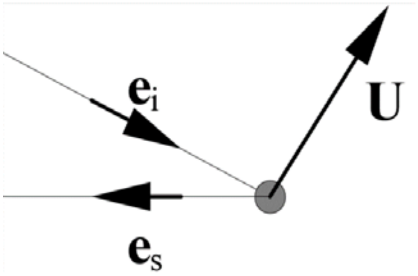

Figure 11 *Schematic of light scattering by the moving particle [28]*

Frequency of scattered light detected by the receiver (photodetector) can be calculated by equation 2.1.

$$f_s = f_i + f_i \frac{U(e_s - e_i)}{c} = f_i + \frac{U(e_s - e_i)}{\lambda_i} \tag{2.1}$$

The Doppler frequency is represented by the second term in equation 2.1. The Doppler frequency is usually several magnitudes lower than the frequency of light. This setup is suitable only for the measurement of high–speed moving particles. The commercially used 1D LDA system consists of two laser beams focused to the point, where the measurement volume is formed. The particle passes through this measurement volume and scatters the light of two incoming laser lights simultaneously [29]. This principle is illustrated in Figure 12. Incoming light beams with unite vectors e_1 and e_2 are scattered by the particle. Each light beam is scattered with different frequencies. The difference is caused by a different angle of the beams. The frequency of scattered light by the first beam, the second beam, and the frequency difference can be computed by equation 2.2, 2.3, and 2.4, respectively.

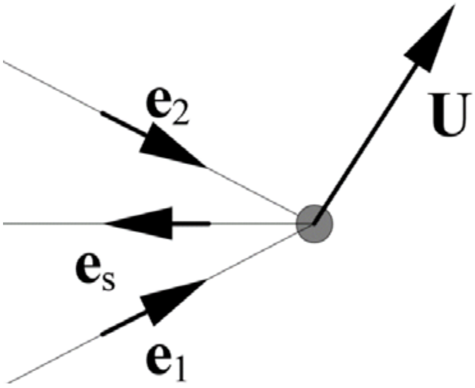

Figure 12 *Principle of scattering light by two incoming lights [30]*

$$f_{s,1} = f_1 \left[1 + \frac{U}{c}(e_s - e_1)\right] \tag{2.2}$$

$$f_{s,2} = f_2 \left[1 + \frac{U}{c}(e_s - e_2)\right] \tag{2.3}$$

$$f_D = f_{s,2} - f_{s,1} \tag{2.4}$$

Laser beams are emitted by the same laser, frequency f_1 and f_2 are equal. Then, the Doppler frequency can be written as equation 2.5 where we can see that the Doppler frequency is proportional to the velocity perpendicular to the measurement volume. θ is the angle between the incoming laser beams.

$$f_D = \frac{U(e_1 - e_2)}{\lambda_i} = \frac{2\sin(\theta/2)}{\lambda_i} u_x \tag{2.5}$$

2.1.2 Fringe model

The fringe model is commonly used in LDA as a simple visualisation producing the correct results [28].

When the two beams intersect and create a measurement volume, the interference pattern is present within the intersection. This pattern is composed of light and dark planes, so-called fringes. The important characteristic of the fringe pattern is the distance between the fringes; it can be computed by equation 2.6.

$$\delta_f = \frac{\lambda}{2\sin(\theta/2)} \tag{2.6}$$

Figure 13 shows the interference pattern within the intersection of two laser beams.

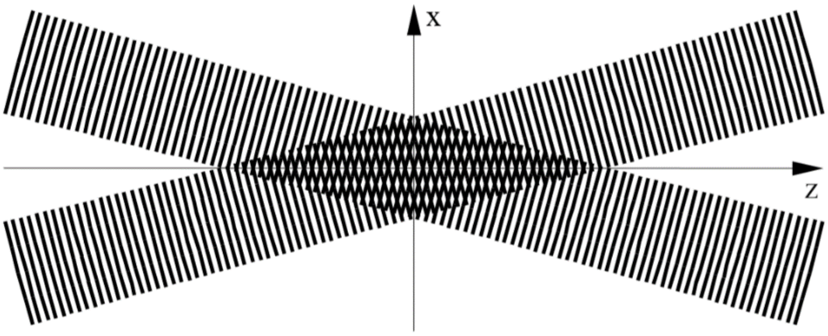

***Figure 13** Interference pattern in the volume of measurement [28]*

The fringes in Figure 13 are parallel to the x-axis. The frequency of scattered light will be proportional to the x component of the droplet velocity vector *U* moving across the volume of measurement (equation 2.7).

$$f_D = \frac{u_x}{\delta_f} \tag{2.7}$$

By combining equations 2.6 and 2.7, the same form as in equation 2.5 is obtained.

2.1.3 Measurement volume

From Figure 13, it is clearly visible that the velocity measurement of droplet velocities takes place in the measurement volume. The size of the measurement volume can be seen in Figure 14, and the dimension is described by equations 2.8, 2.9 and 2.10 for height, width, and length, respectively. Because of the small size of the measurement volume, the LDA/PDA measurement techniques were acknowledged as techniques with high spatial resolution in the flow field measurement [30].

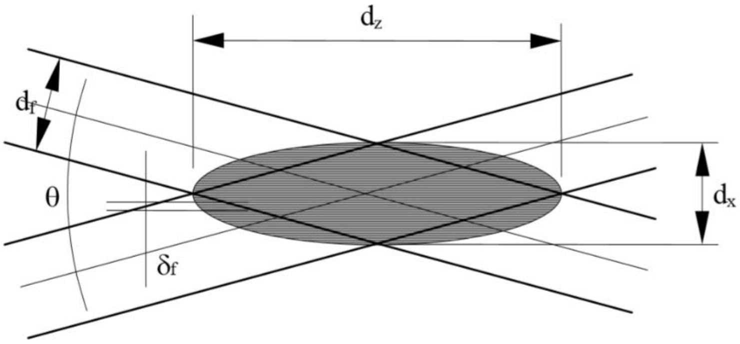

***Figure 14** Size of measurement volume [28]*

$$\mathrm{d_x} = \frac{\mathrm{d_f}}{\cos(\theta/2)} \tag{2.8}$$

$$\mathrm{d_y} = \mathrm{d_f} \tag{2.9}$$

$$\mathrm{d_z} = \frac{\mathrm{d_f}}{\sin(\theta/2)} \tag{2.10}$$

Beam intersection angle θ is usually small, d_x and d_y are approximately the same and are labelled as the diameter of the measurement volume. The laser beam intensity has a Gaussian distribution across the laser beam cross-section illustrated in Figure 15. Small droplets crossing the volume of measurement on the outer diameter may not be detected because these droplets will not scatter enough light.

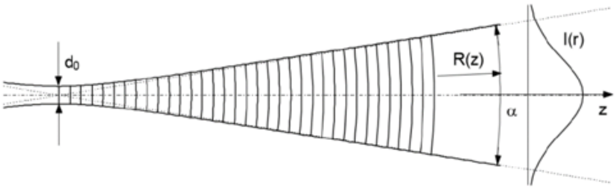

Figure 15 *Gaussian distribution of laser beam intensity I(r) [28]*

2.2 Phase Doppler anemometry

Extension of LDA for simultaneous measurement of particle velocity and particle diameter resulted in the development of PDA measurement technique. The measurement concept of PDA was proposed in 1975; many research groups have worked on improving the measurement system over several following decades [31]. PDA is now a standard technique for the fluid flow research, but the acceptance of this technique has taken several decades. During this period, the PDA was verified by other, well known, velocity measurement techniques (Constant temperature anemometry, Pitot tube).

PDA measures velocity and the particle diameter in the range from 0.5 µm to several millimetres. The LDA measurement technique uses only one photodetector. The PDA system uses more photodetectors, usually two or three. The signal reaches photodetectors with the same frequency f_d, but with the phase shift between the signals (Figure 16). The phase shift is caused by a different path of the scattered signal. The phase shift is dependent on the angular position of the receiver. Figure 17 illustrates the optical arrangement of two photodetectors in the PDA system.

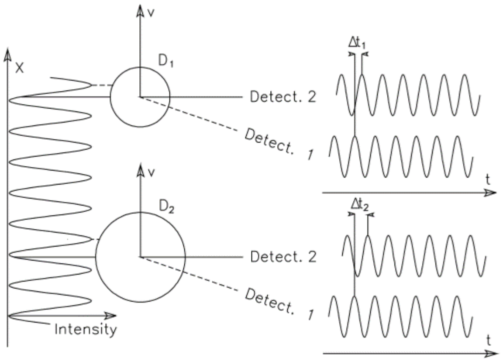

Figure 16 *Phase difference between two detectors at different angles [28]*

Figure 16 shows the increasing phase difference with increasing particle diameter. The phase shift can be computed by equation 2.11. The two-detector PDA system can distinguish the phase shift only in the range from 0 to 2π. The phenomenon called 2π ambiguity can arise. This phenomenon can be solved by three-photodetector arrangement.

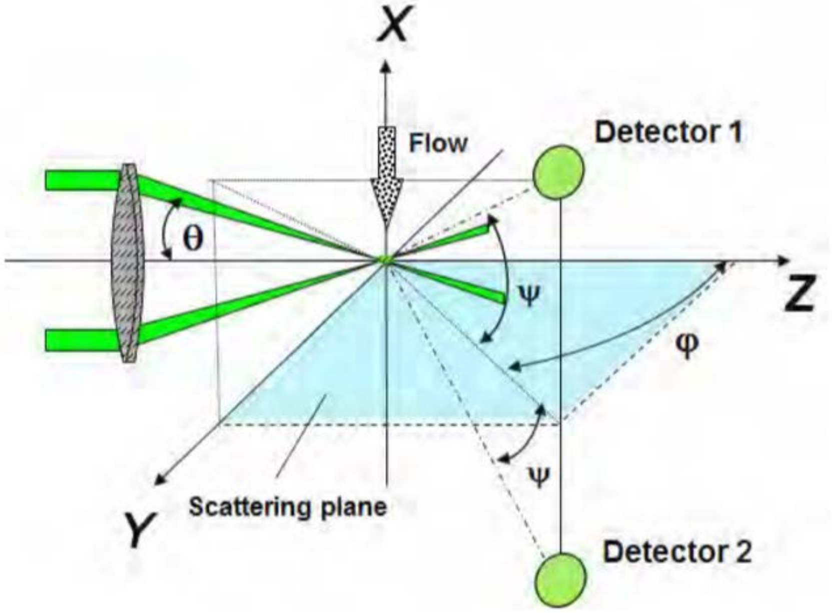

Figure 17 *Arrangement of PDA measurement system [32]*

$$\Delta\Phi_{12} = 2\pi f_d \Delta t \qquad (2.11)$$

2.2.1 Flow Measurement behind the plane window

LDA and PDA are optical measurement techniques. These techniques require a direct optical access to the flow. Some problems may occur during the flow probing behind the plane window. Fringe spacing distortion can occur when the plane window is not perpendicular to the transmitter head. The window for access to the inspected flow can be slightly distorted from the production (curved surface, not perfectly smooth). The curvature of the window can cause a shift in the measurement volume to the virtual position. The transmitter has to be perpendicular to the window, otherwise the shift of the measurement volume occurs as illustrated in Figure 18 [30].

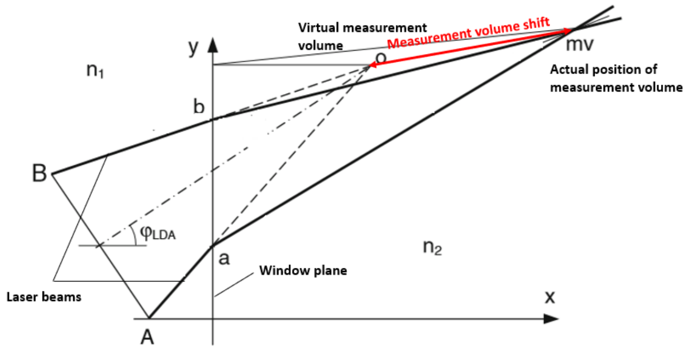

Figure 18 *Shift of measurement volume, adapted from [30]*

2.2.2 Measurement in Turbulent Flow with Spatial Velocity Gradient

The measurement volume is small enough, PDA measurement can be considered as the technique for measurement of local flow. The small size of the measurement volume permits us to presume the uniform velocity distribution across the measurement volume. This assumption is available for measurement far from the wall. The size of a viscous boundary layer has a comparable thickness as the measurement volume. During the measurement of the flow near the wall in the boundary region, the size of the measurement volume should be as small as possible to obtain good results. If it is not possible, the accuracy of measurement is lowered in the boundary region. The system measures a higher turbulence intensity (broadening effect), the sampling rate is proportional to the velocity of the flow, so the velocity distribution influences the measurement accuracy of the flow velocity. This phenomenon is known as the velocity bias. In this case, the velocity bias could not be simply assumed as the measurement error because it is the natural behaviour of the flow in the boundary region. This phenomenon is illustrated in Figure 19.

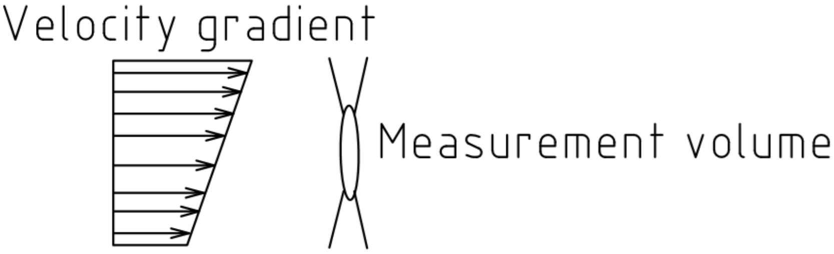

Figure 19 *Measurement in flows with a spatial velocity gradient*

2.3 Particle image velocimetry

PIV was developed from a very similar technique - Laser speckle velocimetry (LSV). LSV deals with the displacement of speckle patterns. The origin of LSV can be found in solid mechanics. The extension to fluid mechanics was presented in 1977. In most fluid flows, the observer could see particles not speckles, so PIV arise in 1984 and rapidly became a dominant method [33].

The PIV system consists of a double–pulsed laser, optics to form the light plane, camera, synchronizer, and a computer for data processing and analysis. The schematic layout of PIV system is illustrated in Figure 20.

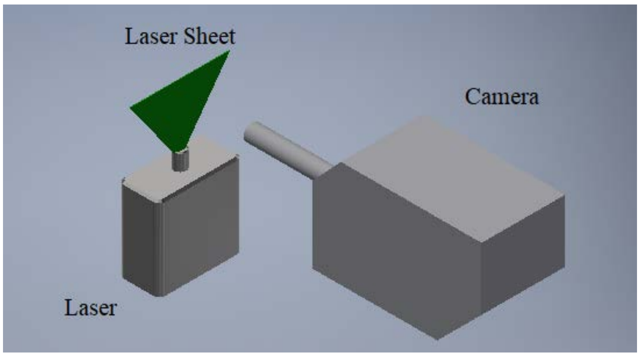

Figure 20 *Schematic layout of PIV system*

The double-pulsed laser creates two pulses with sufficient time step Δt [s] to illuminate the area of interest. The flow is seeded with particles which scatter the light towards the camera to record the image of the particles. Images are digitalized and processed. The result from the analysis of the instantaneous images is the particle displacement Δx [m]. The velocity of the particle v_p [m/s] can be computed by equation 2.12.

$$v_p = \frac{\Delta x}{\Delta t} \tag{2.12}$$

Calibration of the system needs to be performed prior to the measurement. The calibration target with equidistantly spaced dots is placed in the area of interest as illustrated in Figure 21. Calibration is used to correct the optical distortions of the camera and provide the magnification function to map the real-world coordinates x–y to the image coordinate system X–Y [34]. Three “doughnut” shaped dots determine the calibration target centre.

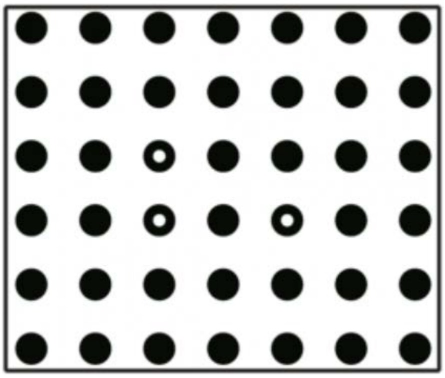

Figure 21 *Calibration target [35]*

Image processing consists of the following steps. The first step is recognition of the particles within the image. Some filters are used to spatially enhance the visibility of particles and to suppress the noise (median filtering, low-pass filter). Interrogation regions are created, and the displacement of the particle is determined. Single pulse, double frame images or single frame, double pulse images can be used. The image of the result obtained from PIV is illustrated in Figure 22.

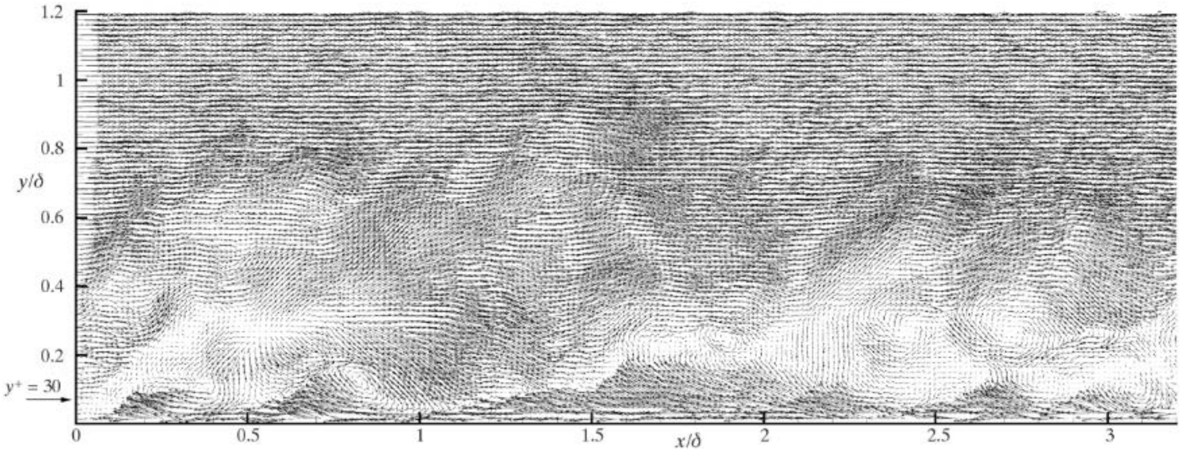

Figure 22 *PIV results (vector map) [33]*

2.4 High–speed imaging

High–speed imaging technique is possible because of the advancement in high–speed cameras. In 1886, Austrian physicist Peter Salcher captured the first image of a supersonic bullet. The first high–speed cameras used during the 1930s were able to run at 1000 frames per second. In 1940, a rotating mirror camera was invented; it was theoretically capable of 1 000 000 frames per second [36]. High–speed cameras used nowadays are capable of recording the images at 1 000 000 000 frames per second.

High–speed imaging allows to capture a detailed structure of fast changing fluid flows by acquiring a series of images. The system for high–speed imaging is composed of the illumination source (Xenon flash, LED lamp or a high-frequency lasers) and high–speed camera connected with the computer. The high–speed camera can be seen in Figure 23.

There are some parameters that have to be set before any high–speed imaging, such as frame rate, exposure time, and resolution.

The optimum frame rate f [Hz] can be estimated by equation 2.13. The optimum frame rate is based on the number of samples N [-] (number of images), velocity of the observed phenomena u [m/s], and the typical length scale l [m].

$$f = \frac{Nu}{l} \tag{2.13}$$

The proper choice of the shutter depends on the nature of the flow. When the exposure time is set too high, the acquired images are blurred. With reducing the exposure time, it is possible to obtain an image with good temporal resolution and to properly observe the flow behaviour. A shorter exposure time has more demands for the illumination source [37]. The spatial resolution of the image is another important parameter. It determines a good and sharp visibility of the smallest objects within the flow. The spatial resolution is usually reduced with the increase in the frame rate.

From the analysis of the instantaneous images, the information on the fluid flow structure and velocity in a plane can be obtained. For information on the flow in 3D, the setup with more cameras is needed. In recent years, volumetric systems capable of measuring all three components of velocity in the volume have been developed [8, 38].

***Figure 23** High–speed camera [39]*

3 BASICS OF LIQUID ATOMIZATION

In this section, different types of pressure atomizers are described, and atomization of liquid sheets is outlined. Pressure atomizers are the subject of research in Spray laboratory at Brno University of Technology. Spray behaviour and influence of different factors on liquid spray are outlined. It is convenient to understand the behaviour of the liquid atomization and breakup of liquid sheets in steady conditions. The behaviour of a liquid sheet in cross-flow may be different and more complicated than the behaviour in steady conditions. This section should help the reader to understand the basic processes during liquid sheet atomization and apply this knowledge to the liquid breakup in cross and co-flow conditions. The knowledge of working principle of pressure swirl atomizer is important for the design of a fuel circuit and of some parts of a wind tunnel.

Atomization increases the surface area of the fluid volume. This is of particular interest in combustion applications where atomization promotes evaporation of the fuel and mixing with the ambient air [40].

3.1 Pressure atomizer

The liquid is atomized through a small discharge orifice under high applied pressure. In the atomizer, the pressure energy of a liquid is converted into the kinetic energy (velocity) of an emerging spray. The velocity increases as the square root of pressure [41]. Most of the atomizers used in general applications are pressure atomizers. There are several designs of pressure atomizers, e.g. plain orifice, pressure swirl-simplex, square spray, duplex, dual orifice, spill return, and fan spray.

Plain orifice

A simple circular discharge orifice is used for injection of a round jet into the ambient environment. The diameter of the orifice governs the atomization quality. The smaller is the diameter of the orifice, the finer is the atomization. The difficulties with filtration of the liquid and the presence of impurities limit the diameter of the plane orifice. This type of pressure atomizer is often used in combustion applications, e.g. ramjet, rocket engines, diesel engines, and afterburners. A schematic layout of plain orifice atomizer is illustrated in Figure 24.

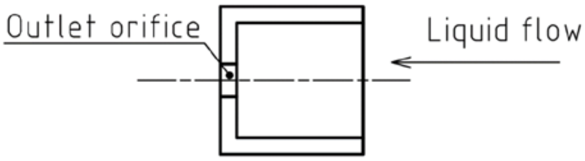

Figure 24 *Plain orifice atomizer*

Pressure swirl–simplex

A schematic layout of simplex pressure swirl atomizer is illustrated in Figure 25. This atomizer is composed of tangential inlets, swirl chamber, and discharge orifice. Via tangential ports, the atomizing liquid is supplied to the swirl chamber where the liquid gains a swirl velocity component and consequently flows through the exit orifice into the ambient environment. During this process, an air core is created in the swirl chamber. The air core extends from the discharge orifice to the rear back of the swirl chamber. Pressure swirl atomizers create a hollow cone type spray, where most of the liquid volume is concentrated on the outer periphery of the spray.

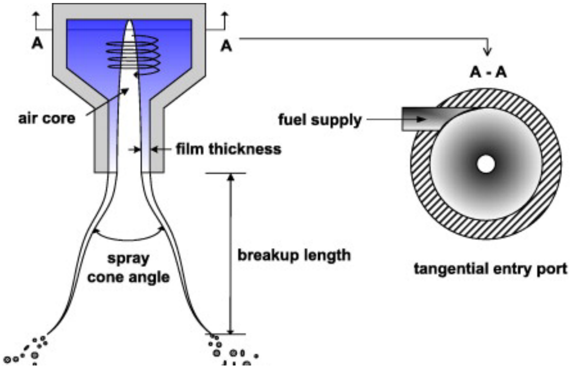

Figure 25 *Simplex pressure swirl atomizer [42]*

Square spray

This atomizer has a special shape of the exit orifice which produces almost a square spray. The atomization quality is not very good, but a large area can be covered by this spray. The square spray and the square spray nozzle are illustrated in Figure 26.

Figure 26 *Square spray and nozzle [43]*

Duplex

This nozzle has two sets of distributor slots with two feeding systems. Slots have a different cross-section area (smaller–primary, larger–secondary). These slots transport the liquid into the swirl chamber. If the liquid flow rate is low, the liquid flows through the primary slot. At higher flow rates, the liquid flows through both slots. The duplex atomizer provides good atomization over a wide range of flow rates with only a low pressure required for atomization. The duplex atomizer is illustrated in Figure 27.

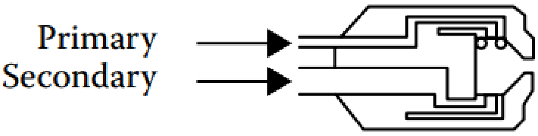

Figure 27 *Duplex atomizer [41]*

Dual orifice

This nozzle is almost identical to the duplex atomizer. A dual orifice has two concentrically placed swirl chambers within the atomizer body. At low flow rates, all liquids flow through the inner swirl chamber. With increasing flow rate the liquid is supplied mostly through the outer swirl chamber designed for higher flow rates. The dual orifice nozzle provides more flexibility than the duplex atomizer.

Spill–return

The spill–return atomizer is a modification of simplex atomizer. The spill–return atomizer contains a spill–line at the rear back of the swirl chamber. By the spill–line, the amount of liquid removed from the swirl chamber can be adjusted. This nozzle allows for a very high turndown ratio defined as the ratio of the maximum flow rate to the minimum flow rate. The spill–return atomizer is illustrated in Figure 28.

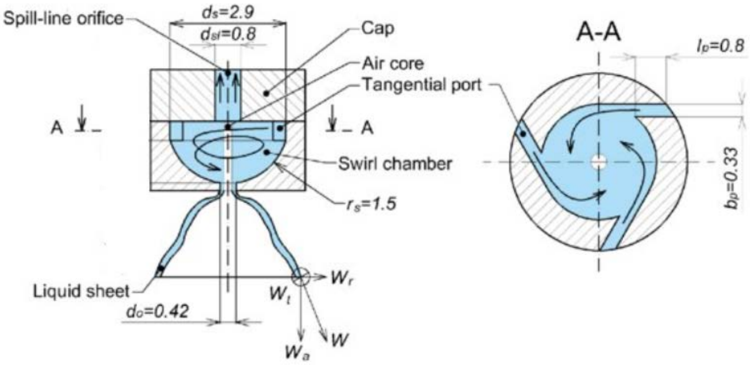

***Figure 28** Spill–return pressure swirl atomizer [44]*

Fan spray

Several different concepts are used to produce flat or fan-shaped sprays. A widely used type of nozzle is the one in which the orifice is formed by the intersection of a V groove with a hemispheric cavity communicating with a cylindrical liquid inlet [45]. The fan spray can be also produced by the collision of impingement jets. The fan spray is illustrated in Figure 29.

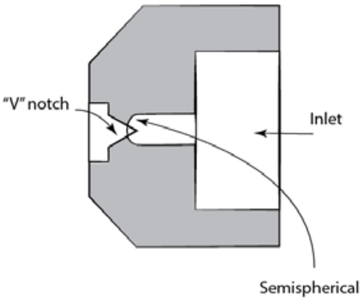

***Figure 29** Fan spray nozzle [46]*

3.2 Disintegration of liquid sheets

The liquid, discharged from the pressure swirl atomizer, forms a conical liquid sheet. The thickness of the liquid sheet influences the atomization quality. The more stable is the liquid sheet, the larger is the breakup length, and the atomization quality rises. Disintegration of the liquid sheet mainly depends on the relative velocity of the liquid and ambient gas. Three modes are recognized during disintegration of a liquid sheet; sheet disintegration due to perforation, sheet disintegration due to wave phenomena, and liquid atomization. The disintegration modes are illustrated in Figure 30.

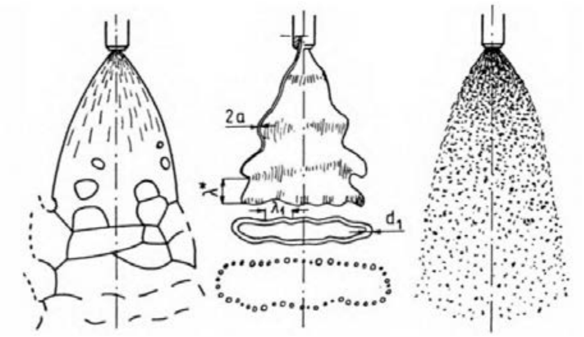

Figure 30 *Sheet disintegration [41]*

Three important forces act on the liquid sheet during disintegration. Viscous force, surface tension force, and inertia. Three dimensionless numbers are defined to represent these forces [47].

$$Re = \frac{\rho_l D v}{\mu_l} = \frac{Inertia}{Viscous\ forces} \tag{3.1}$$

$$We = \frac{\rho_l D v^2}{\sigma_l} = \frac{Inertia}{Surface\ tension\ force} \tag{3.2}$$

$$Oh = \frac{\mu_l}{\sqrt{\sigma_l \rho_l D}} = \frac{\sqrt{We}}{Re} \tag{3.3}$$

Equation 3.1 represents the Reynolds number, equation 3.2 the Weber number, and equation 3.3 represents the Ohnesorge number. Only D (characteristic dimensions) represents the atomizer, other parameters characterize the liquid [40].

3.2.1 Sheet disintegration due to perforation

This mode is present in the spray with a relatively small relative velocity (several meters per second). The sheet propagates downstream and is spread in the radial direction. The sheet thickness decreases. When the sheet thickness is sufficiently small, perforations occur. They grow and create a net of narrow jets which then disintegrate into the droplets. This mode of disintegration creates droplets with a relatively large diameter. The atomization quality is poor. Etteneni et al. [48] studied the perforation of impinged jets. They found that the formation and growth of perforation depend on the liquid jet velocities. Formation of perforations was evident with the Reynolds number higher than 200. The number of perforations increases with increasing velocity of jets. With the jet Reynolds number lower than 200, disintegration is governed mainly by capillary instability.

3.2.2 Sheet disintegration due to wave phenomena

At higher velocities, the sheet disintegrates due to wave phenomena. Waves grow on the sheet surface causing the sheet to break up into ligaments (primary breakup) and then the ligaments disintegrate into the droplets (secondary breakup). Figure 31 represents wave disintegration.

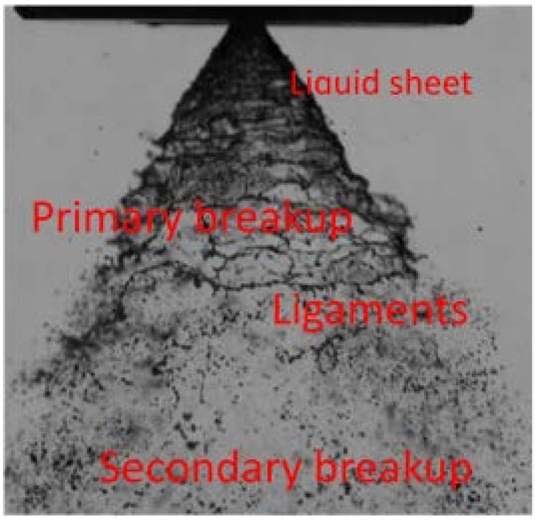

Figure 31 *Sheet disintegration due to wave phenomena*

3.2.3 Liquid atomization

For velocities of the liquid sheet, approximately larger than 100 m/s, the proper liquid atomization occurs. The short length waves are formed on the surface of the liquid sheet. These waves grow and cause a rapid breakup. The ambient medium may cause disturbances on the liquid sheet and can form the droplets before the waves are formed.

3.3 Effect of various factors on the mean drop size

In combustion applications, the information on the droplet sizes and droplet spatial distribution is very important. Droplet sizes determine the atomization quality, combustion performance of a spray, flame structure, ignition, produced emissions, and temperature distribution within the flames [49].

In combustion and mass transfer, a frequently used parameter to describe the droplets is Sauter mean diameter (*SMD* or D_{32}). It is the ratio of the volume of the droplets divided by the surface area of droplets (equation 3.4). There are other diameters of droplets, e.g. D_{10}, D_{20}. These diameters are not presented here.

$$SMD = D_{32} = \frac{\sum_{i=1}^{n} n_i D_i^3}{\sum_{i=1}^{n} n_i D_i^2} \tag{3.4}$$

The rheological properties of liquid, properties of the ambient medium, liquid pressure, and atomizer dimensions govern the atomization of pressure swirl atomizers. The liquid properties are viscosity, surface tension, and density of the liquid. In practice, the effect of surface tension and density can be negligible because the fuels used in industrial applications exhibit only a slight difference as for this property [50]. The more viscous is the fluid, the larger is the *SMD* because the viscous forces deteriorate the breakup and formation of smaller droplets. The effects of viscosity and surface tension on *SMD* are governed by equations 3.5 and 3.6, respectively.

$$SMD \propto \mu_L^a \tag{3.5}$$

$$SMD \propto \sigma^b \tag{3.6}$$

In equations 3.5 and 3.6, the exponents *a* and *b* are present. Different values for *a* and *b* were obtained by different researchers.

Pressure and temperature of the ambient medium (usually air) are the properties of interest. Usually, these two properties only influence the medium density. The influence of ambient air pressure on *SMD* is illustrated in Figure 32.

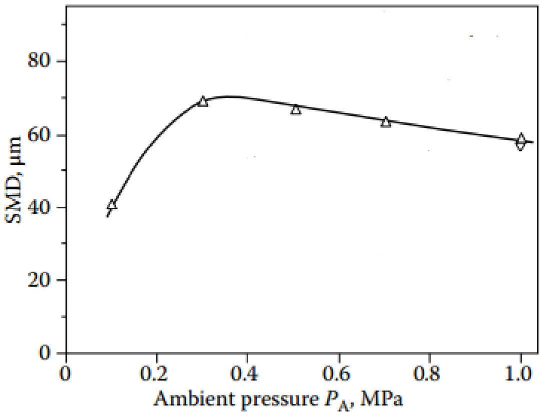

Figure 32 *Effect of ambient pressure on SMD [51]*

An increase of *SMD* in Figure 32 can be attributed to the droplet coalescence or to the change in the breakup mode. Rizk and Lefebvre [51] attributed this increase to the reduction of cone angle of the spray. With increasing ambient temperature, the liquid temperature is also increased, thus the viscosity of the liquid is decreased and *SMD* is reduced. The operating conditions of the pressure swirl atomizers in combustion applications are the increased pressure and high temperature with high gradients of velocity field.

3.4 External spray characteristics

The function of the atomizer is to atomize the bulk liquid into fine droplets and distribute these droplets uniformly into the ambient gas in the form of a symmetrical spray. In order to describe the spray, the external spray characteristics are used. Penetration, cone angle, radial and circumferential liquid distribution are the most important external spray characteristics.

3.4.1 Penetration

Penetration of a spray is defined as a maximum distance of a discharged liquid in an ambient environment measured from the nozzle tip. In a diesel engine, penetration is also a function of time, and spray penetration is investigated in different time steps. Penetration is promoted by increasing the liquid initial velocity (inlet pressure). The aerodynamic drag of ambient environment has an opposite effect on penetration. When the aerodynamic drag increases, penetration of the spray decreases. The initial velocity is usually high, but when the spray propagates further downstream, kinetic energy is dissipated by friction losses. Far from the nozzle tip, the kinetic energy of a liquid is almost zero and the trajectory of spray or droplets is mainly governed by the gravity force or by the movement of ambient gas.

Sprays with a narrower cone angle exhibit larger penetration than sprays with a wide cone angle. This is caused by a smaller surface area of the spray where kinetic energy is dissipated to the surrounding medium. The drag of the ambient medium changes with the spray propagation. In the beginning, the first droplet (the edge of liquid film) dissipates the energy to the surrounding medium which then starts to move with the spray. The relative velocity between the spray and the ambient environment is reduced and penetration of the spray increases. The spray induces the air movement in the near spray region. Air–liquid interaction of pressure swirl spray was studied by Jedelský et al. [52].

3.4.2 Cone angle

The ambient gas creates waves on the liquid sheet. Because of these waves, the spray contour is not a straight line, and determination of the spray cone angle is not an easy task. The commonly used procedure for determination of the spray cone angle is to record the spray by the high–speed camera. From images obtained by high–speed recording, the spray contour can be determined, and the spray cone angle is derived. It is recommended to describe how the spray cone angle was determined in any study concerning this topic.

The spray cone angle can change with the inlet pressure of discharged liquid. The increase in pressure also increases the spray cone angle. The spill-line opening also causes an increase in the spray cone angle in spill–return pressure atomizers. Measurement of the spray cone angle is described for example in the study of Milan Malý [53] or in the study conducted by Dikshit et al. [54].

3.4.3 Patternation

The spray produced by the pressure swirl atomizer is assumed to be symmetrical. In combustion applications, the asymmetrical spray may cause poor liquid-gas mixing. Temperature gradients and different heat loads within the spray may be present. Poor mixing affects the efficiency of the combustion and produces more emissions.

Spray asymmetries are caused by inappropriate surface finish of the swirl chamber wall, by clogging of the inlet tangential ports or discharge orifice. The symmetry of the spray is also influenced by the properties of the ambient medium.

For measuring of radial liquid distribution, a radial patternator illustrated in Figure 33 (left) is used. It consists of a number of tubes where the discharged liquid is collected. The amount of liquid in each tube determines the radial liquid distribution. For measuring of circumferential liquid distribution, different types of patternator are used (Figure 33 right). The function principle is similar.

Figure 33 *Radial patternator (left) and circumferential patternator (right) [41]*

3.5 Jet and liquid sheets in cross-flow

Atomizers operate in conditions where the ambient flow of air or gas is present. It is important to assess the external and internal spray characteristics in realistic conditions. The ambient flow influences the behaviour of a spray. Atomization performance, mixing of droplets, and combustion emissions are influenced. Usually, two approaches are used; investigation of a spray in cross-flow conditions or in co-flow conditions. The difference between these two approaches is illustrated in Figure 34. As we can see in Figure 34 left, the liquid is injected perpendicular to the direction of the flow, and the jet is bent in the direction of the flow, the penetration length is reduced by the momentum of cross-flowing air. The liquid distribution within the spray is different from the steady ambient conditions. The smaller droplets (droplets with less momentum) have a lower penetration length than the droplets with larger diameter, because they are entrained by the momentum of the flow. In Figure 34 right, the liquid jet in co-flowing air is illustrated. The direction of the injection is similar to that of the flowing air. If the co-flow velocity is higher than the droplet velocity, droplets are accelerated by the co-flow. Less drag is present because the relative velocity between the jet and the ambient flow is reduced.

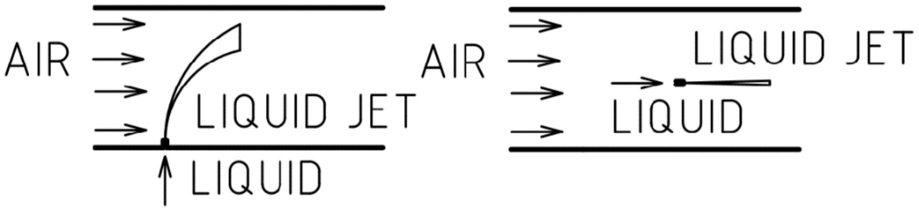

Figure 34 *Cross (left) and co-flow conditions (right)*

Many research activities were performed dealing with liquid jets injected to the cross-flow. For example, Aalburg et al. [55] studied deformation and breakup properties of nonturbulent round liquid jets in cross-flow. Experiments were intended to develop a numerical model for prediction of the jet behaviour in cross-flow. The experiments were carried out in subsonic wind tunnel with a test section of cross-section of 610 × 610 mm with transparent sides. Cross-flow velocity varied between 5 and 18 m/s at ambient pressure and temperature. The maximum injection pressure of round supercaviting nozzle was 1.5 MPa. Test conditions involved two different liquids (water and ethyl alcohol), liquid injector diameters of 0.5 and 1.0 mm and liquid jet velocities of 9–14 m/s. This yielded the following ranges of normalized test variables: liquid/gas density ratios of 806 and 997, liquid/gas viscosity ratios of 48 and 66, cross-flow Reynolds numbers of 345–1100, cross-flow Weber numbers of 0.6–12, liquid/gas momentum ratios of 170–6700, and jet Ohnesorge numbers of 0.003 and 0.013. Cross-flow Mach numbers were smaller than 0.1; therefore, compressibility effects were negligible. Bai et al. [56] studied the mixing of turbulent spray injected into gaseous cross-flow. A commercially available nozzle (1/4MK B80100S303-RW) was used. The nozzle produces spray with an angle of 80 ° and D_{32} = 80 µm. Gas Reynolds number varied in the range from 12 900 to 45 000, and different nozzle angles were applied (60, 90 and 120 °). The wind tunnel with the test section of 95 × 95 mm was used. The test section was composed of thin transparent ports in the transversal direction because the PIV measurement system was used. Adding of droplets into the cross-flow enhanced the turbulent intensity of cross-flow, and the spray created different-scales vortices (CVP-counterrotating vortex pair). Different types of atomizers in cross-flow were tested by Lee et al. [57], who investigated the behaviour of aerated liquid jet, created by an effervescent nozzle, and subjected to the cross-flow. Experiments were performed in the subsonic wind tunnel with the test cross-section of 0.3 × 0.3 m and cross-flow velocities up to 60 m/s. Double pulsed digital holographic microscopy (to overcome the small depth of focus) was used to investigate the spray. Spatial resolution was 5 µm, the smallest droplets were not recognized. A 3D velocity map, droplet size distribution in the near injector region (22.5 × 27 mm), was reconstructed. Behzad et al. [58] identified breakup processes of non-turbulent liquid jets. Numerical results are compared to the experimental data. Two breakup processes are identified; surface breakup, occurring close to the nozzle, and column breakup, present further in the cross-flow. Wu et al. [59] obtained a large amount of experimental data on the breakup process of a liquid jet in cross-flow. Test liquids, nozzle orifice diameter, and air Mach number varied. The liquid jets were tested in the subsonic wind tunnel with rectangular cross-section of 125 × 75 mm and length of 406 mm. The breakup structure was visualized and analysed using a pulsed shadowgraphic technique with Nd: Yag laser. The authors found that the distance from the nozzle tip to the column breakup point is in every test case approximately 8 times the nozzle orifice diameter and is independent of the jet injection conditions. Some studies deal with not only the effect of cross-flow but also with high temperature or pressure conditions. For example, Bunce et al. [60] studied the behaviour of the liquid jet at high temperature (650 °C) under cross-flow conditions. Two-dimensional Mie scattering imaging and a laser-line Mie scattering measurement were employed to characterize the behaviour of the liquid jet. Liquid jets were exposed to oscillating and non-oscillating flow conditions. The Jet-A was used as a working fluid. The test section of 38.1 × 25.4 mm was used. A combustor for burning the Jet-A fuel was placed after the test section. It was found that penetration is similar in both cases, oscillating and non-oscillating flow. Penetration height was different than that predicted in theory because of high temperature. Influence of temperature was not implemented in theory. Eslamian et al. [61] studied the jet injected into elevated pressure and temperature subsonic cross-flow; such conditions are present in lean premixed prevaporized combustor (LPP). The test section provides the optical access of 50 × 150 mm. Maximum temperature of 573 K, maximum pressure of 517 kPa and cross-flow velocities in the range of 22–156 m/s were tested. Water was used as a working fluid. PIV and PDPA were used to investigate the jet. Evaporation of the smallest droplets was not investigated. Two breakup modes were identified; shear breakup, present at high Weber number, and column breakup, present at low Weber number. When the temperature of the airstream is increased, penetration of jet decreases. Equations for jet trajectories were proposed considering different parameters of the flow. Guo et al. [62] investigated the behaviour of a spray in high pressure cross-flow. A specially designed high-pressure wind tunnel with pressurized tank and compressors was used. PIV and high–speed camera were used to investigate the jet. Maximum allowable pressure was 0.6 MPa with cross-flow velocity of 20 m/s. Spray penetration, spray profiles, and spray distortion were studied. Impingement of the jet was observed. Experiments with different angle of injection were carried out by Costa et al. [63]. They studied the spray characteristic of angled liquid injection subjected to cross-flow. Water was used as a working fluid. The size of the test section was 150 × 100 mm. Maximum air velocity was approximately 43 m/s. Liquid jet angles of 15, 30 and 45 ° were examined. With decrease of liquid injection angle, the shear stress acting on a jet surface also decreases; there is also a decrease in the relative velocity of the jet and the flow. To complement the experimental work, plenty of studies dealing with the simulation of jets can be found. Behzad et al. [64] studied the surface breakup of liquid jets injected into a gaseous cross-flow under high gas Weber number conditions present in combustion applications. Only numerical simulations were made in this research. The results show that infinitesimal disturbances are excited immediately after the jet is exposed to the gas flow. As the disturbances are transported along the jet trajectory, they start to grow due to the shear instability. Subsequently, a two-stage mechanism causes the jet surface to break up. In the first stage, the cross-flow drags the crests of waves in the downstream direction, which results in the formation of sheet-like structures protruding to the leeward of the jet. In the second stage, the sheet surrounded by a thick rim disintegrates into ligaments and, finally, into droplets due to the propagation of span-wise waves. Li et al. [65] used the Eulerian-Lagrangian scheme to numerically investigate the jet in cross-flow. Mach number of 1.94 was used. Kelvin-Helmholtz, Rayleigh-Taylor and Taylor Analogy Breakup were used. Numerical results were compared with experimental data. The liquid trailing phenomenon was observed within the experiment, numerically computed, and physics under this process was described.

Only a few studies focused on a pressure swirl spray (conical liquid sheet) in cross-flowing air. Prakash et al. [66] investigated pressure swirl sprays in cross-flow conditions utilizing a high–speed camera visualization for various Weber numbers and liquid-to-air momentum flux. Different breakup modes were recognized and mapped in this study. Lee et al. [67] studied the macro and microscopic pressure swirl spray parameters by a high–speed camera, under cross-flowing air (6–40 m/s). Rachner et al. [68] investigated the behaviour of a plain jet, created by an airblast atomizer, under conditions relevant to lean premixed prevaporized combustion in gas turbines. Zhang et al. [69] investigated dispersion and mixing of droplets in the far-field region. The investigation was done using a PIV technique. The lack of experimental data calls for further and comprehensive investigation of liquid sheets, formed by the pressure swirl atomizers with spill-line, in realistic conditions. For this study, only a conical liquid sheet in cross-flowing air will be described.

The behaviour of a swirling liquid sheet in cross-flow is a very complicated phenomenon. No single dimensionless parameter exists to describe the behaviour of a liquid sheet in cross-flow. Studies consider the aerodynamic Weber number and liquid-to-air momentum flux. The Weber number is described by equation 3.2 and the liquid to air momentum flux can be determined by equation 3.7.

$$Q = \frac{\dot{m}_{liquid} v_{liquid}}{\dot{m}_{air} v_{air}} \tag{3.7}$$

The calculation of Weber number is not an easy task. Due to a swirling motion of a liquid film, the air core is created, and the liquid flows as a thin film through the exit orifice. Due to a swirling motion of a liquid sheet, the relative Weber number is defined. It describes the nature of the flow more appropriately than the normal Weber number. The difference in the Weber number and the relative Weber number is the used velocity. The relative Weber number uses the relative velocity of the jet and cross-flow, the Weber number considers only a cross-flow velocity. The conical liquid sheet in cross-flow is illustrated in Figure 35.

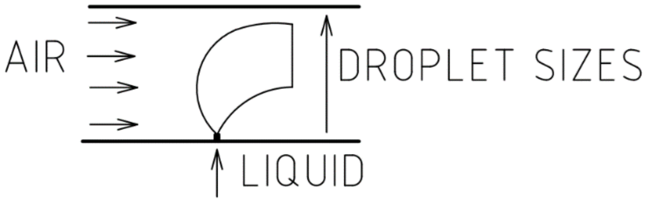

***Figure 35** Conical liquid sheet in cross-flow*

As was mentioned in the case of the liquid jet, the spray is bent in the direction of the cross-flow. The higher is the magnitude of the cross-flow velocity, the more rapidly the spray bends. The droplet distribution is changed by the cross-flow, the distribution of droplet sizes is illustrated in Figure 35. The cross-flow acting on a liquid sheet promotes/changes the liquid disintegration. The breakup length decreases because the disturbances are promoted by the cross-flow.

4 WIND TUNNEL DESIGN

In the first part of this thesis, the wind tunnels and especially blowdown wind tunnel components were briefly described. In this section, the design of the blowdown wind tunnel and the design procedure are described in detail. The first step in the wind tunnel design is a design of the test section because it is the most important part of every wind tunnel. The second step is the proper design of the flow straighteners which govern the turbulent intensity in the test section. The heart of the wind tunnel is a driving fan. The proper choice of the fan is important for the good flow quality in the test section. Before the wind tunnel is designed, the designer had to know the purpose of the wind tunnel, the required flow parameters in the test section and the maximum dimension (size) for the wind tunnel.

In chapter 1, a suitable design of the wind tunnel was selected, and essential parts of a wind tunnel were described. The open type wind tunnel in blowdown arrangement is the most suitable for our case. The schematic layout of this wind tunnel type is illustrated in Figure 4.

4.1 Test section

The investigated pressure swirl spray has a maximum cone angle of approximately 70 °. The area of interest is 120 × 120 mm in the spray centreline. The size of the test section is usually in the range from 80 to 300 mm. In the smallest test sections, a higher velocity flow is obtained. The penetration of spray is smaller at higher flow velocity. In some studies, concerning sprays in cross-flow, where the cross-section area was set to 150 × 150 mm, the droplet adherence to the test section sides was apparent, and the quality of high–speed visualization decreases. The size of the test section was set to 200×200 mm and also with respect to the volume flow rate (power of a driving fan). The size of the cross-section of the test section influences the volume flow rate according to equation 4.1. A schematic drawing of the spray in the test section is illustrated in Figure 36. The spray is investigated by means of optical techniques described in chapter 2. The test section is equipped with glass windows on each side. For the experiments with PDA and high–speed imaging, the optical access from two opposing sides is necessary. PDA requires the access for the laser beams from one side and for the receiver from the other side. The high–speed imaging requires the optical access for illumination and the camera. PIV requires the access for the laser sheet and, in the perpendicular plane, the access for the camera. More information on the setups of some measurement techniques are outlined in chapter 6. In most of the cases, the Pyrex glass, PMMA, Perspex glass or float glass are used to ensure a good optical access. In our case, float glass was used because of lower price, flatness, and low manufacture demand. The model of the test section can be seen in Figure 37.

A maximum velocity magnitude in the test section is set to 30 m/s. This velocity is present in combustion chambers. According to equation 4.1, the required volume flux of air is 1.2 m^3/s. This parameter is used for the driving fan design.

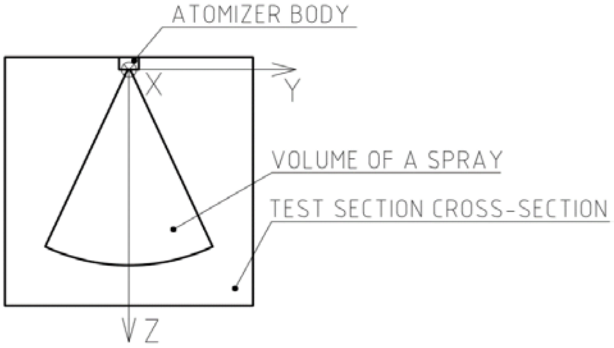

Figure 36 *Spray in the wind tunnel test section cross-section*

$$\dot{V} = vS \tag{4.1}$$

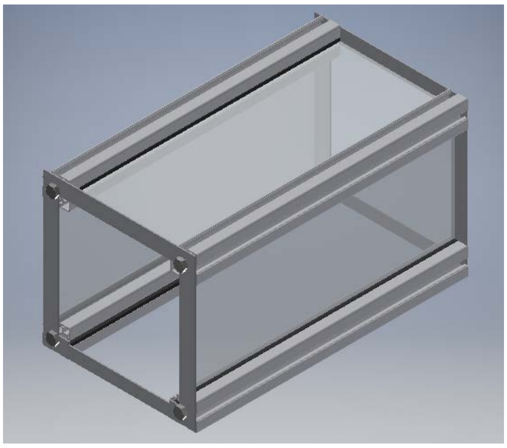

Figure 37 *Test section design*

The test section in Figure 37 is composed of four 30 × 30 mm profiles (ALUTEC KK s.r.o). Mounted on two steel frames with an inner cross-section of 200 × 200 mm. The windows are placed in the ALUTEC profile groove of approximately the same width as the glass to ensure that the windows are parallel. This test section design ensures a fast exchange of windows in the case of damage.

4.2 Laminarization section

The cross-section of laminarization section was set similar to the cross-section of the test section. The minimum recommended length is 10 times the characteristic length (hydraulic diameter). The length was set to 1000 mm, which corresponds to 5 times the characteristic length. Length is restricted by the working space in Spray research laboratory. The crucial for this section is the precise production. Any misalignment can lead to flow instabilities and a low flow quality in the test section.

4.3 Confusor design

As was mentioned in the first part of this thesis, the flow is accelerated in the confusor. The section should be smooth and symmetric. In equation 1.3, the contraction ratio is described. $S_{out} = 0.2 \times 0.2 = 0.04\,m^2$ and the contraction ratio was chosen as $K = 9$. The inlet cross-section area is $S_{in} = K \times S_{out} = 9 \times 0.04 = 0.36\,m^2$ and the length was set to 0.5 m.

4.4 Settling chamber

The cross-section area of the settling chamber is the same as that in the inlet cross-section of the confusor (600 × 600 mm). The size of 600 × 600 mm was set according to the pressure drop of the flow straighteners used in the settling chamber and the working space in the laboratory. It is convenient to use as large cross-section as possible, because the flow velocity and pressure loss decrease. The four flow straighteners are placed in the settling chamber. The first flow straightener is positioned at the inlet to this section. According to [70], the recommended space between the flow straighteners is $L_{req} = 0.2 \times L_{char} = 120\ mm$. The L_{char} is the characteristic length of the settling chamber, which was set to 600 mm. The cross-section of 600 × 600 mm reduces the velocity by a factor of 9 (contraction ratio) and pressure losses by a factor of 81.

Flow straighteners had to be still in the flow. In order to place the flow straighteners inside the settling chamber, the four threaded rods are welded to the inlet of the settling chamber. The inlet has a slightly smaller cross-section area in order to accommodate the rods. The position of the flow straighteners in the settling chamber can be easily modified on the rods.

4.5 Flow straighteners

A combination of flow straighteners is used to ensure a good flow quality in the test section. One honeycomb and three meshes with different solidity are used. The honeycomb is placed first at the inlet of the settling chamber. Three different meshes are placed according to their porosity in a descending order. The position of the flow straighteners is established by matrices.

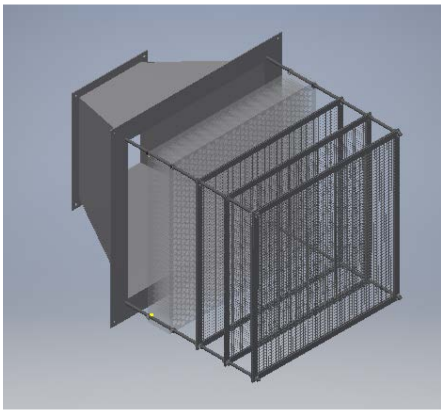

Figure 38 *Flow straighteners*

Honeycomb

The honeycomb cross-section is 600 × 600 mm with hexagonal holes. The thickness of the aluminium plates is 0.3 mm. The hole hydraulic diameter is approximately 5 mm. The width of the honeycomb structure is 50 mm. It was proposed by Bradshaw and Pankhurst [71] that honeycombs with length/diameter ratio of 10 have the greatest impact on flow straightening.

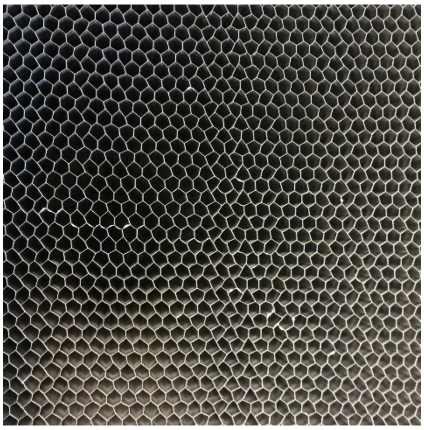

***Figure 39** Honeycomb design*

Screens

Three meshes in steel frames are used. The steel frame provides a better allocation of the screens in the settling chamber. Wire diameters used are 1.3, 0.75 and 0.5 mm. The meshes have a solidity bellow 0.58. Screens were described in the first chapter.

4.6 Inlet diffuser

The inlet diffuser is illustrated in Figure 40. The length was set to 340 mm to save the working space in the Spray research laboratory. The inlet diffuser connects the cross-section area of 250 × 355 mm with the settling chamber cross-section of 600 × 600 mm. The inclination angles are approximately 20 ° and 27 °.

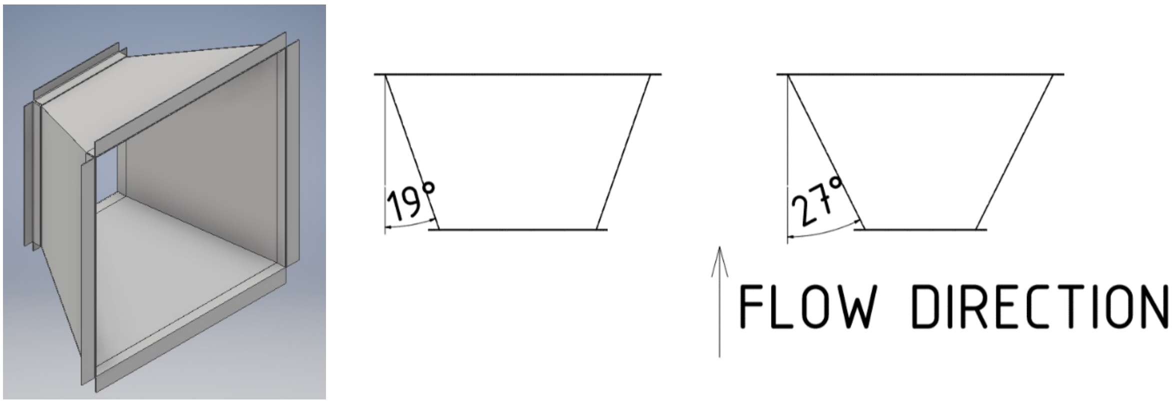

***Figure 40** Inlet diffuser*

4.7 Compensator

The PDA measurement system is a pointwise technique and requires traversing the whole spray across the measurement volume. In order to move with the spray, the whole construction of the wind tunnel is movable (except the driving fan). The driving fan is placed separately. To ensure the movement of wind tunnel construction, the compensator is used to connect the driving fan and the wind tunnel construction. This device allows for the movement of the tunnel construction in three dimensions, while the driving fan stays on the spot (reduce the load imposed on the traverse system). The compensator reduces spreading of vibrations from the fan to the body of the wind tunnel (the measurement of construction vibrations will be described later). The separation of vibrations is very important because any small shift can disrupt the measurement using the PDA system.

The required movement is ± 200 mm in the axial direction and ±100 mm in the lateral direction. This movement covers the whole volume of the test section. The compensator is designed to withstand the pressure difference of 1 kPa. A schematic layout of the fabric compensator is illustrated in Figure 41.

The influence of the compensator on the behaviour of the flow in the test section was investigated. The experiments are described in chapter 5.3.

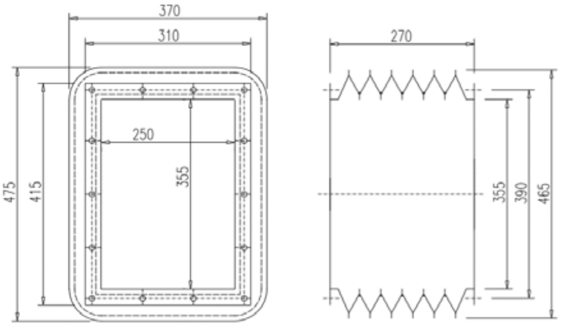

Figure 41 *Schematic layout of fabric compensator*

4.8 Driving fan

Table 4.1 summarizes the velocity and pressure losses of each section. These losses were computed for the maximum velocity of 30 m/s in the test section. For the wind tunnel construction, steel plates of a thickness of 1.2 mm were used with surface roughness $k = 0.1$ mm.

There are two types of pressure losses; friction pressure losses and local pressure losses. Friction losses are caused by friction between the fluid and walls. The amount of energy dissipated (amount of pressure losses) depends on the properties of the fluid and wall roughness. This type of pressure losses is given in equation 4.2. The second type of pressure losses is caused, for example, by some control elements (valves, measurement devices), change in the pipe diameter, etc. In the wind tunnel, this type of pressure losses is present in the nozzle, diffuser, grids, and honeycombs. To compute the local pressure losses, the equation 4.3 can be used. Crucial is the local pressure loss coefficient ζ_m.

$$\Delta p_f = \lambda_f \rho \frac{L}{d_h} \frac{v^2}{2} \tag{4.2}$$

$$\Delta p_m = \zeta_m \rho \frac{v^2}{2} \tag{4.3}$$

Table 4.1 *Pressure losses of wind tunnel*

Part	**Mean velocity [m/s]**	**Reynolds number [-]**	ζ_m **[-]**	Δp_f **[Pa]**	Δp_m **[Pa]**	**Total pressure loss [Pa]**
Test section	30.0	398406.4	-	32.4	0.0	32.4
Laminarization section	30.0	398406.4	-	40.5	0.0	40.5
Nozzle	7.5	99601.6	1.5	14.3	50.6	65.0
Settling chamber	3.3	132802.1	-	0.3	0.0	0.3
Honeycomb	3.3	132802.1	1.1	0.0	7.0	7.0
Screens	3.3	132802.1	2.1	0.0	14.0	14.0
Inlet diffuser	7.5	298804.8	0.2	5.9	4.3	10.2
Compensator	13.5	263060.4	-	21.2	0.0	21.2
Exit diffuser	19.2	373545.8	0.1	14.9	12.2	27.0

The overall pressure loss of the wind tunnel is $\Delta P = 216.4$ Pa at volume flow rate $\dot{V} = 1.2\ m^3/s$. As described in the first chapter, two types of fans can be used - axial and radial. The radial fan was chosen based on the parameters Δp, $\dot{V}$ and the rectangular shape of the compensator and inlet diffuser. It is suitable to use the fan with some reserve in the volume flow rate and allowable pressure differential. The radial fan RFC 355-15/3-3-L-Z illustrated in Figure 42 was used. The frequency shifter is used to control the frequency of the fan and the velocity in the test section. Type LS Industrial Systems SV040iG5A-4 for 4 kW was used.

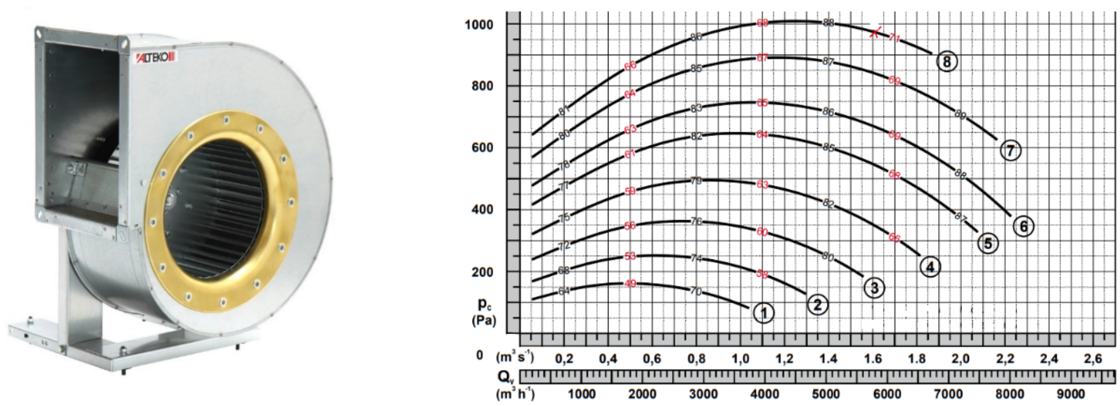

***Figure 42** Radial fan (left) fan characteristic (right) [72]*

In Figure 42 (right), P–Q characteristic is illustrated for different fan rotation speeds (1–8). The P–Q characteristic was determined by the company.

The flow velocity is measured by the differential pressure gauge. The pressure differential is measured between two points in the laminarization section (500 mm spacing). From the known pressure drop and the measured velocity of the flow in the test section, the relationship between the pressure drop and velocity is determined. The pressure drop for different wind tunnel speeds is illustrated in Figure 43. The blue dots are the experimental result. The green line denotes the fit of experimental data and the red line in Figure 43 represents theoretical results.

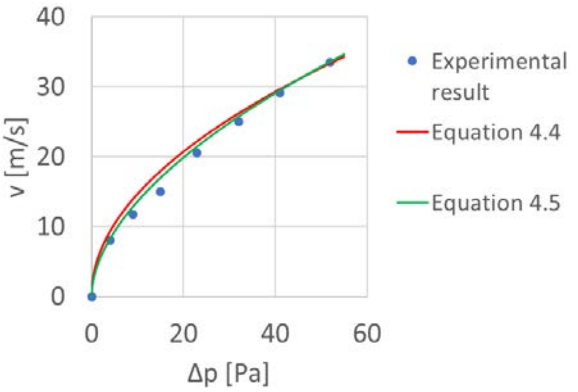

***Figure 43** Pressure drop for different velocities*

The theoretical relationship between the velocity and pressure drop can be described by equation 4.4.The green line is described by the equation 4.5. In the equations 4.4 and 4.5, the parameter d contains the diameter of a pipe, length, density of air, and friction coefficient. Equation 4.5 describes the velocity better for low pressure drop and is valid only in the velocity range of the wind tunnel. Pressure losses measured do not agree well with the value predicted by the theory. The difference can be caused by the rectangular shape of the section or the usage of maximum axial velocity for predicting the pressure loss. Many equations for friction coefficient were used, but a better agreement with experimental data has not been found.

$$v = d\Delta p^{0.5} \tag{4.4}$$

$$v = (d-10)\Delta p^{0.55} \tag{4.5}$$

4.9 Traverse system

The purpose of traverse system is to move with the entire construction of the wind tunnel to precisely measure the whole spray. There are three options for the traverse system movement. The traverse system moves with the measurement device, the system moves with the wind tunnel or the traverse system moves with the nozzle. The PDA/LDA measurement system is sensitive to any movement, so the option to move with the measurement device was not considered. The movement of the nozzle is possible because the nozzle is a small device and the existing traverse system in the Spray laboratory could be used. The movement of this nozzle needs some design changes in the test section. This type of movement requires the open test section type of wind tunnel to be used. According to [73], many wind tunnels of open test section type suffer from insufficient flow quality and require post construction diagnostics. It would be possible to open the test section only from one side, but it could change the flow behaviour in the test section either. The most suitable traverse system is to traverse with the wind tunnel construction. The existing traverse system can be used, and only a special support system should be designed to properly move with the wind tunnel construction. This traverse system can also provide a wider use for the wind tunnel.

The wind tunnel traverse system is comprised of two systems. The drive part, which is connected directly to the test section, and the supporting (driven) part, which supports the wind tunnel and allows for the wind tunnel to move freely in any direction. The step motors are used to ensure the precise movement in three directions (x, y, z). As the drive part, the Linear traverse system (ISEL AUSTRIA GMBH & CO. KG) was used. This system is illustrated in Figure 44. The linear system is controlled via the driver and the software with an accuracy less than 0.1 mm.

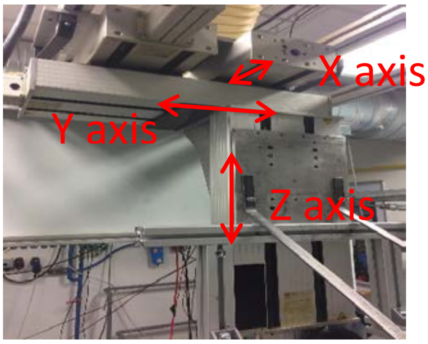

Figure 44 *Linear traverse system*

The supporting system is composed of the load bearing structure, linear screw jack, linear rail movement structure, and four stabilisers. Any slight movement of the traverse system causes the movement of the whole wind tunnel supported by the driven part. The supporting system is mounted to the settling chamber, where the centre of gravity of the wind tunnel is located. The supporting system is illustrated in Figure 45

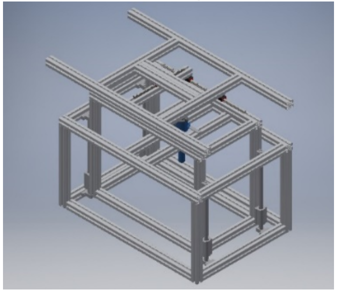

Figure 45 *Supporting system*

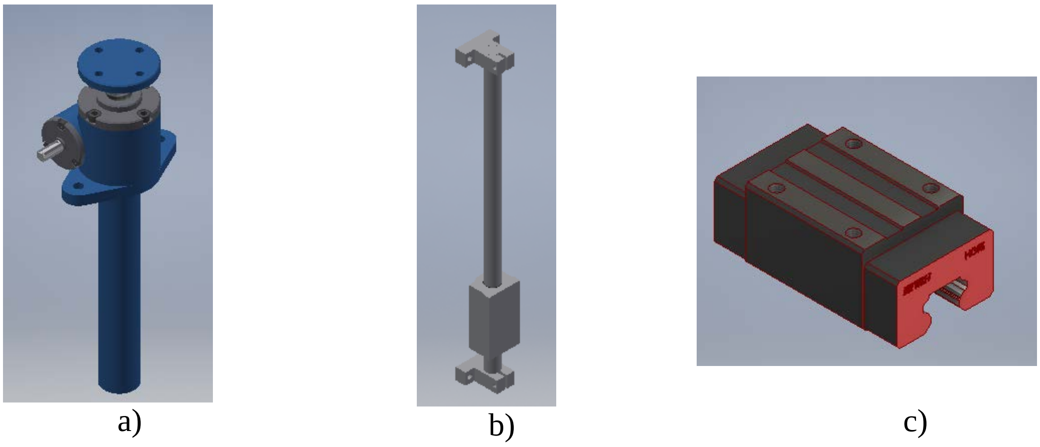

a) b) c)

Figure 46 *Parts of the supporting system a) Screw jack b) Linear support c) Rail support*

For the movement in the vertical axis, the screw jack illustrated in Figure 46 a) is used with a maximum load of 500 kg. The screw jack has 0.25 mm vertical shift per drive shaft rotation; this allows for the precise definition of the position of the wind tunnel. The step motor is connected to the screw jackshaft. The step motor is controlled via the drive software synchronized with the step motor of the driving mechanism. The rail support illustrated in Figure 46 c) allows for the movement in two horizontal axes. The rail support has a low friction and adds no force demands for the driving system.

4.10 Droplet separation

The droplets from the spray are carried away by the flow. The Jet A1 (kerosene) is used as a working fluid. It is not safe to connect the wind tunnel to the ventilation system because the fumes from the Jet A1 are explosive. The flow of air with a dispersed droplet of kerosene must be cleaned. The pressure swirl atomizer creates a wide size range of droplets (1–150 µm). It is convenient to separate as much liquid as possible with a device with a low pressure drop and sufficient size. This device is placed after the test section.

There are some options for droplet separation: filters, lamellar separator, and cyclone separator. In some studies, kerosene droplets were combusted in the burner placed after the test section. Each separation device works on a different principle. In the following section, this working principle is described.

4.10.1 Lamellar separator

This device is comprised of differently shaped lamellas that are arranged in blocks (Figure 47). The flow with kerosene droplets passing through the lamellar separator is forced to change the direction repeatedly. Larger droplets hit the lamellas and are driven away by the gravitational force. These droplets have larger inertia and do not follow the flow precisely, so the lamellar separator is able to collect them. Smaller droplets can pass through the lamellar separator without being captured. The number of turns reduces the number of smaller droplets passing through the separator. Droplets smaller than 10 µm are not captured. It is possible to modify the space between the lamellas and to reduce the captured droplet size. With reducing the lamellas spacing the pressure loss rises. The increase in velocity also reduces the number of droplets passing through the separator. The pressure loss for spacing of 18 mm is approximately 190 Pa (axial velocity 5 m/s) and the separator collects the droplets larger than 20 µm. The spacing of 23 mm has a pressure drop of 100 Pa and collects the droplets larger than 35 µm. A filter can be used in series with the droplet separator. Some filters may change the pressure resistance according to the number of droplets captured (change the pressure drop according to the humidity of the filter). Changing of pressure drop influences the flow in the test section during the experiments. One experimental regime with the pressure swirl atomizer has a duration of approximately 20 minutes, the maximum mass flow rate is approximately 7 kg/h. This gives us 2.3 kg of fuel discharged within one experiment. Assuming 50% efficiency of the droplet separation in the lamellar separator, the filter had to capture 1.16 kg of fuel. Fine filters have a great pressure drop. This arrangement is not suitable because of the change in pressure drop and low separation efficiency of the separator. The advantage of this setup is a simple design and relatively small sizes.

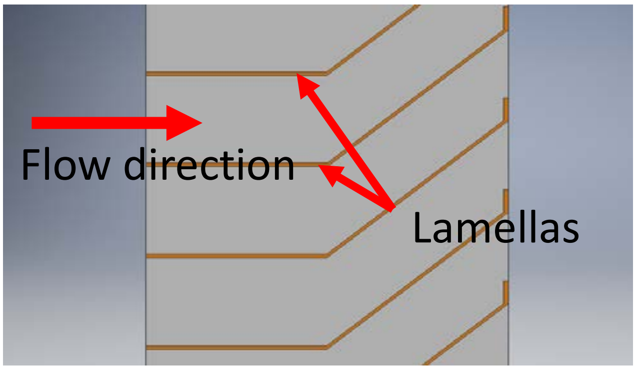

Figure 47 *Shaped lamellar separator*

4.10.2 Cyclone separator

The cyclone separator is the second device used to separate the droplets from the flow. The cyclone separator uses the centrifugal force acting on the flow in the separator body. By centrifugal force, droplets are collected on the walls and drained away from the flow. Three main factors influencing the efficiency of the separator are particle/flow velocity, collection area, and residence time in the cyclone. Aforementioned parameters are used to describe the performance of the separator, the pressure drop, and the fractional efficiency curve of the cyclone. The fractional efficiency curve is illustrated in Figure 48.

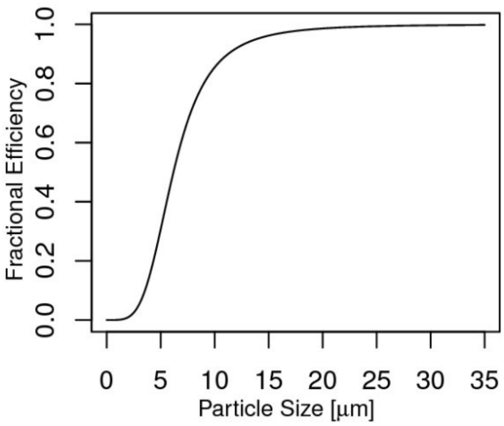

Figure 48 *Fractional efficiency curve [74]*

From the fractional efficiency curve, the separation characteristic of the cyclone is derived. The droplets with a diameter of 10 µm are separated with 80% efficiency. The droplets with a diameter larger than 15 µm are separated with almost 100% efficiency. The cyclone separator has a higher efficiency than the lamellar separator, but requires more space for similar pressure loss. There are many designs of the cyclone separator; some of them are described further. Main design features of these cyclone types are outlined. The basic design of the cyclone separator can be seen in Figure 49. A small working space in the Spray research laboratory restricts some parameters of the cyclone separator. The maximum cyclone separator diameter is $D_c = 1200$ mm with maximum cyclone separator height $H_c = 1500$ mm. Most common designs of the cyclones are referred to as 2D2D and 1D2D. *D* stands for the separator body diameter, 2D2D describes the length of a body (2 times *D*) and the length of a cylinder (2 times *D*). 1D2D is the cyclone with a body length of *D* and cylinder length of 2 times *D*.

Standard design

Two known dimensions of a cyclone are $D_c = 1200$ mm and $H_c = 1500$ mm. The inlet cross-section is rectangular with dimensions of 300 × 300 mm, the length of the cyclone body $L_b = H_c/2$ and the length of the cyclone cone $L_c = L_b$.

The first parameter is the number of effective turns N_t described by equation 4.6. The increase in the number of turns causes the increase in collection efficiency.

$$N_t = \frac{1}{H}\left(L_b + \frac{L_c}{2}\right) \tag{4.6}$$

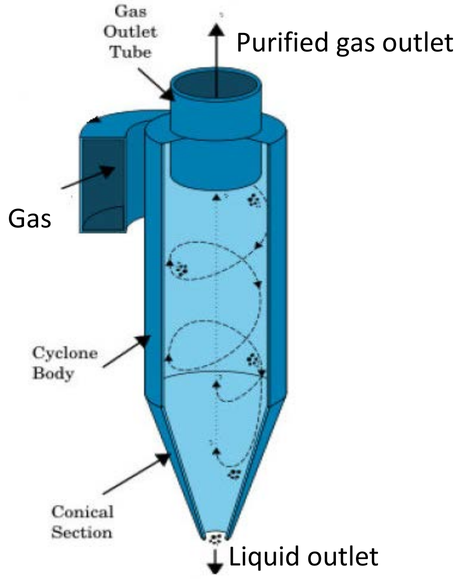

Figure 49 Basic cyclone separator design-adapted from [75]

Number of effective turns is N_t= 4.25.

The next parameter is the cut point diameter d_c. It is the aerodynamic equivalent diameter of the particle collected with 50% efficiency. The larger cut point diameter means the lower collection efficiency. The cut point diameter can be calculated by equation 4.7.

$$d_c = \left[\frac{9\mu W}{2\pi N_e V_i(\rho_p - \rho_{air})}\right]^{0.5} \tag{4.7}$$

The gas dynamic viscosity is μ = 18.3×10^{-6} kg/ms, the width of the inlet W = 0.3 m, the flow velocity V_i = 13.3 m/s, the density of droplets ρ_p = 796 kg/m^3 and density of flowing air ρ_{air} = 1.2 kg/m^3. These parameters resulted in the cut point diameter d_c = 13.2 µm.

Gas residence time is governed by equation 4.8.

$$t_r = \pi D_c N_t / V_i \tag{4.8}$$

Gas residence time is t_r = 1.1 s.

A cyclone pressure drop is computed by equations 4.9 and 4.10. These equations do not count with any vertical dimensions of the cyclone. According to equation 4.10, the shorter cyclone has the same pressure drop as the longer one. In equation 4.9, the parameter K occurs; this parameter depends on the cyclone design and operational conditions and is in the range from 12 to 18 for the standard cyclone design.

$$H_v = K\, HW / D_{ei}^2 \tag{4.9}$$

$$\Delta p = 0.5\rho_{air}V_i^2H_v \tag{4.10}$$

Equations 4.9 and 4.10 led to a pressure drop Δp = 1910 Pa. This pressure loss is not suitable for the selected driving fan.

Tangential inlet design

In this section, another design procedure of the cyclone separator is introduced. A design of the cyclone separator with outlined dimensions is illustrated in Figure 50.

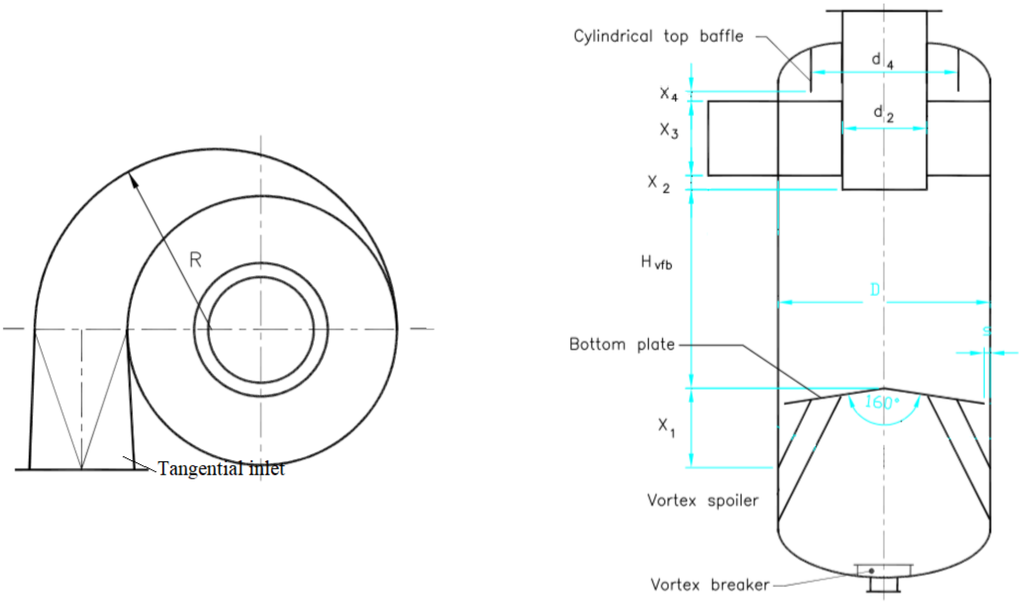

Figure 50 *Cyclone with tangential inlet design - adapted from [76]*

The dimensions of the inlet cross-section were selected as in the first case H = 300 mm and W = 300 mm. According to this design, the diameter of cyclone D_c >2.8 × H = 2.8 × 300 = 840 mm. In this case, the condition is fulfilled with D_c = 1200 mm. The distance $H_{vfb} \geq 0.5 \times D_c$, this condition is also fulfilled.

Overall height of the cyclone separator is computed by equation 4.11.

$$H_{ov} = h_{vfb} + X_1 + X_2 + X_3 + X_4 + l_h \tag{4.11}$$

The variables in equation 4.11 are represented in Figure 50. The variable l_h is the required height for a liquid hold up in the bottom part of the cyclone separator. The variables X_1, X_2, X_3, X_4 are expressed by equations 4.12–4.15

$$X_1 \geq 0.1 + 0.5D_c\tan(10°) \tag{4.12}$$

$$X_2 \geq 0.2H \tag{4.13}$$

$$X_3 \geq H \tag{4.14}$$

$$X_4 \geq 0.1H \tag{4.15}$$

H_{ov} = 1.2 m. Length of 1700 mm is sufficiently large.

The pressure drop of this cyclone design is computed according to equation 4.16.

$$\Delta p = 8\rho_{air} v_{air}^2 \tag{4.16}$$

The pressure drop is Δp = 1698 Pa, which is still high. The pressure drop in equation 4.16 is a function of the velocity of air in the tangential inlet. The solution to reduce the pressure drop is to expand the tangential inlet. The inlet dimensions of 400 × 400 mm reduce the pressure drop to Δp = 540 Pa. An increase in the inlet area reduces the velocity of the flow, the reduced velocity decreases the capture efficiency. This theory also does not count with the height of the cyclone separator.

There are some commercially available droplet separation devices. Some of them have a small capture efficiency; others have a large pressure drop. The most promising separator design was to use two cyclone separators in series. First, the larger cyclone separator to separate larger droplets and, secondly, the smaller one to separate the remaining smaller droplets. Space requirement for this design was high, and the separators could not fit in the Spray laboratory. As an alternative, the cyclone separator, designed by the aforementioned procedure, is used with the inlet cross-section of 400 × 400 mm with the fabric filter placed at the exit pipe. The cyclone separator is able to capture droplets with diameter higher than 20 µm, and the fabric filter captures the remaining droplets. The filter is placed far from the test section and is frequently changed to reduce the risk of pressure drop change.

4.11 Fuel circuit

To investigate the influence of the cross and co-flow on the behaviour of a spray, a circuit for fuel transport from the tank to the atomizer is required. The parameters measured are inlet and spill line pressure, inlet volume flow rate and spill-line volume flow rate. The schematic fuel circuit is illustrated in Figure 51. It is composed of the filter (1), pump (2), Coriolis flowmeter (3), inlet pressure sensor (4), atomizer (5) spill-line pressure sensor (6), spill-line flow meter (7), and storage tank (8).

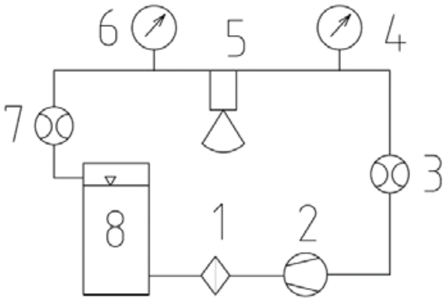

Figure 51 *Fuel circuit*

4.12 Wind tunnel control

The important parameter in every wind tunnel is the flow velocity. Every wind tunnel should be equipped with velocity control system. There are several options for the velocity flow measurement. For example, the Pitot tube or the propeller anemometer can be used. The velocity measurement should take place near the test section. The Pitot tube and the anemometer have to be inserted into the flow. The device in the flow could generate turbulence, and fluctuations of flow could occur in the test section. To prevent generating of turbulence, the flow velocity is measured by the pressure gauge, mentioned in chapter 4.8. The pressure sensor is connected to the LabView software, and the data about the pressure are converted to the velocity data which are collected and exported in the form of xlsx type file. The schematic layout of device connection is illustrated in Figure 52. BD Sensor DPS 300 815-0016-1-0-G-C-Y02-M-000 with measurement range from 0 to 1.6 mbar differential pressure was used.

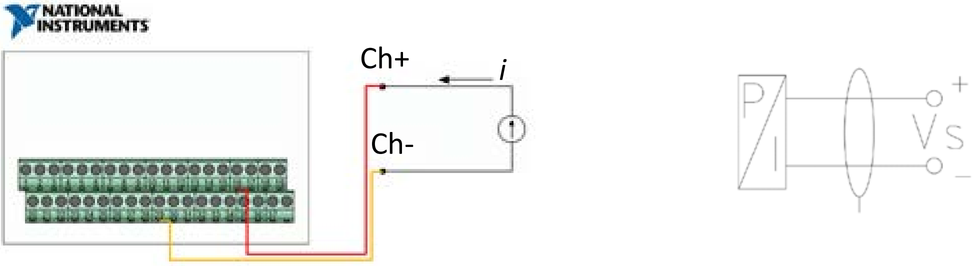

Figure 52 *Pressure gauge connection, LabView connection (left), device connection (right)*

To change the flow velocity, the frequency shifter LS Industrial Systems SV040iG5A-4 for 4 kW (see chapter 4.8) is used. The frequency shifter is connected to the radial fan. Three phase star connection is used. The frequency shifter is equipped with a digital panel and the frequency can be set easily. Remote control illustrated in Figure 53 can be used to set the frequency.

Figure 53 *Frequency shifter remote control*

To control the location of a wind tunnel, two systems described in chapter 4.9 are used. The drive part (ISEL AUSTRIA GMBH & CO. KG) is a commercially available system. The movement in three directions is ensured by step motors connected to the control unit. Displacement of the wind tunnel is managed via software.

To control the displacement of the support system in Z direction, the step motor with another control unit and software can be used. This setup is relatively expensive, and a cheaper variant will be described later. A laser sensor for displacement measurement can be used, for example LAS-T5-250 from WayCon company. The measurement range is 50 – 300 mm with resolution of 0.015 mm. The sensor can be placed on the traverse system (Figure 54) to precisely measure the displacement.

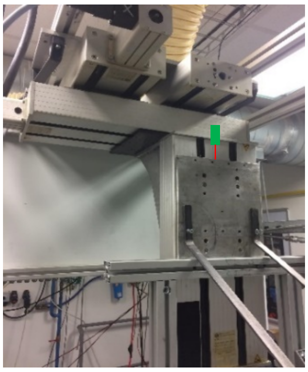

Figure 54 *Laser displacement measurement*

The sensor is represented by the green rectangle while the measured displacement is represented by the red line. The laser sensor is equipped with 4–20 mA output and the information on the displacement can be read via the LabView software. The Screw jack illustrated in Figure 46 is connected to the motor which is controlled via the LabView. The second laser displacement sensor can be placed on the supporting system to measure the displacement of the wind tunnel. The signal from both laser displacement devices is processed in the system. The motor is off, when the displacement is the same on both sensors, and on, when different values are measured. The motor shaft rotates in one direction, when the value difference is positive, and in the other direction, when the value is negative.

4.13 Economical balance

Commercially available wind tunnels cost approximately 400 000 Czech crowns (similar size and parameters). The presented wind tunnel does not contain the traverse system, droplet separator, flexible connection of driving fan, and fuel circuit for the nozzle. Some devices were available in the Spray research laboratory and the prices of these components are not counted to the final price of the wind tunnel. In Table 4.2, the price of the wind tunnel is outlined.

Table 4.2 *Price of a wind tunnel*

Item	*Price [CZK]*
Driving fan	21 574
Frequency shifter	7 220
Compensator	10 000
Wind tunnel construction	20 000
Test section	2 000
Supporting system	50 901
Velocity measurement system	3 000
Droplet separator	30 000
Wind tunnel control system	50 000
Total	194 695

The total price of the wind tunnel is approximately 195 000 Czech crowns. In the price, the work on the wind tunnel (salary) is not included. The price of this wind tunnel is still low, compared to the commercially available wind tunnels. Some important knowledge has been gained during the wind tunnel design, construction, and testing.

5 FLOW QUALITY IN THE TEST SECTION

The parameters of the flow are summarized in the appendix A of the thesis. The flow parameters were determined using LDA, PDA, CTA, and Pitot tube. The velocity of the flow was measured for different fan rotational speeds, the turbulent intensity in the centre of the test section was approximately 5%. However, the turbulent intensity in the test section in well-designed wind tunnels is under 1%. The goal of this chapter is to modify the wind tunnel design to obtain the low turbulent intensity with uniform velocity profile and to precisely define the conditions in the test section.

5.1 Design changes

To obtain the turbulent intensity lower than 1%, some design changes were made. The exit diffuser was designed and mounted at the end of the test section. First diffuser designs proposed were asymmetrical, and two lengths were used. The idea was to increase the mean velocity in the test section and reduce the turbulent intensity. The turbulent intensity is governed by equation 5.1.

$$Tu = \frac{u_{rms}}{u_{mean}} 100 \tag{5.1}$$

The axisymmetric diffuser increases the mean velocity in the test section but also increases the velocity fluctuations (u_{rms}). Increase in u_{rms} can be caused by better propagation of vortices because of decrease in the pressure loss. The schematic designs of diffusers are illustrated in Figure 55.

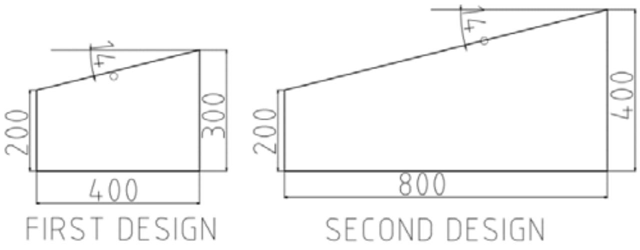

Figure 55 *Designs of axisymmetric diffusers*

Results from PDA measurement are outlined in Figure 56. The axial velocity and turbulent intensity were measured for four regimes defined by fan rotational speed (10, 20, 30 and 40 Hz). The results are presented only for one regime. The trends are similar for other regimes. The axial velocity increases with the presence and length of a diffuser. The turbulent intensity remains unchanged.

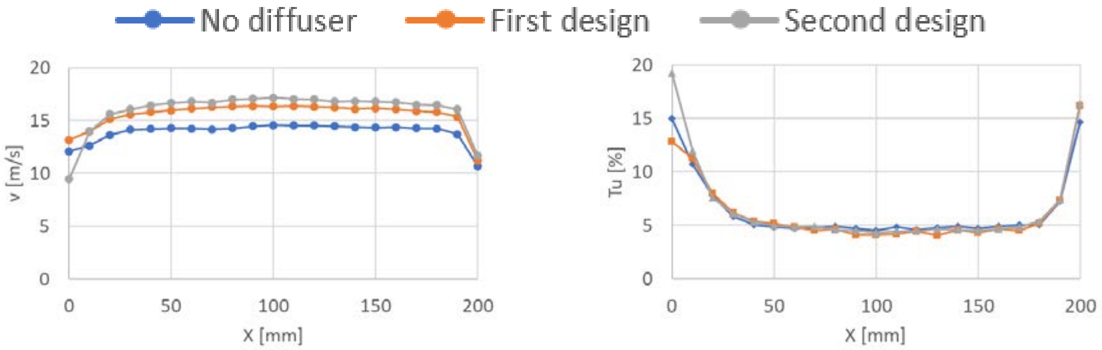

Figure 56 *Axial velocity (left) and Turbulent intensity (right) in the test section*

The axisymmetric diffuser does not decrease the turbulent intensity, so a new symmetrical diffuser was proposed. This design is illustrated in Figure 57. The length of a diffuser is 800 mm and the outlet cross-section area is 300 × 300 mm. The declination angle is approximately 4.6 °.

Flow straighteners were redesigned. Instead of the flow straighteners setup, illustrated in Figure 38, redesigned flow straighteners are used. A new setup is composed of denser wire mesh at the inlet of the settling chamber, see Figure 58, and three honeycombs equidistantly spaced in the settling chamber. D_m = 2 mm. Spacing between the flow straighteners is 120 mm.

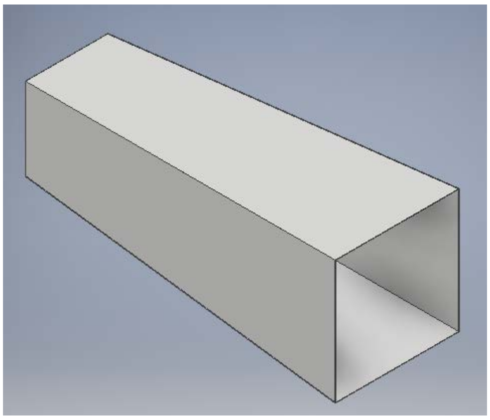

Figure 57 *Symmetric exit diffuser*

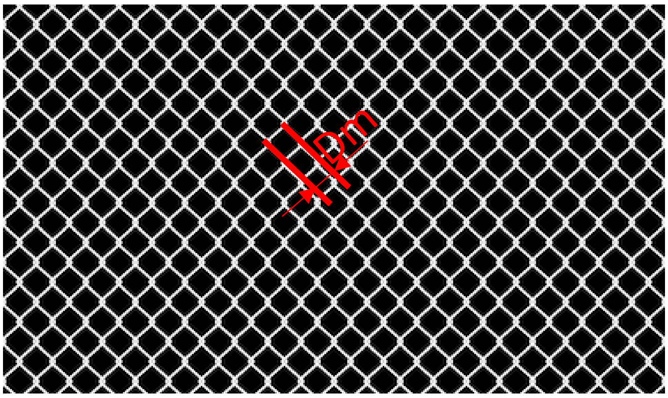

Figure 58 *Wire mesh*

The effect of new flow straighteners and symmetrical diffuser is illustrated in Figure 59. Axial velocity and turbulent intensity were measured for four different velocities in the test section. Results are illustrated only for one velocity (identical to Figure 56). In Figure 59 left, the effect of design changes on the velocity is illustrated. In Figure 59 right, the turbulent intensity can be seen. A huge difference is apparent from this figure. Many flow straighteners setups were tested; this setup exhibits a low turbulent intensity with uniform velocity profile across the test section.

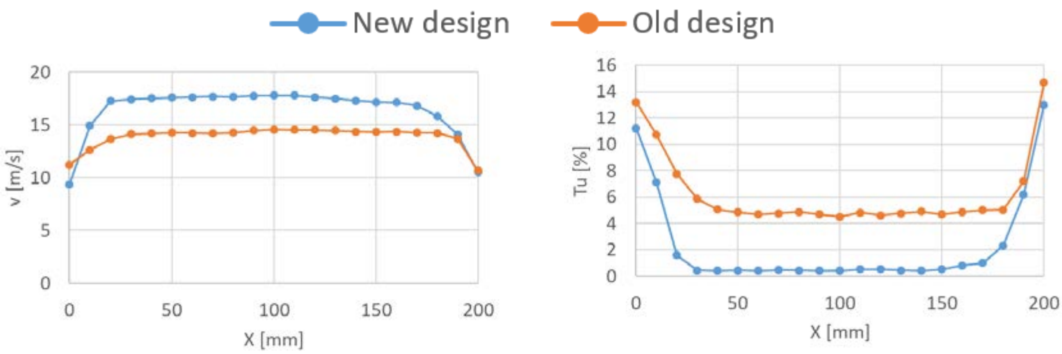

Figure 59 *Axial velocity (left), Turbulent intensity (right)*

For any experiment in the wind tunnel, well-defined flow parameters are required. The velocity in the test section is in the range from 0 to 40 m/s. The turbulent intensity is for all cases under 0.7% in the middle of the test section.

There are some components of the wind tunnel that may have an adverse effect on the flow quality in the test section. The influence of these components on the flow behaviour was assessed. The design of a driving fan and the used compensator influenced the flow quality in the test section. The experiments were performed to assess the influence of misalignments during the manufacture of the fan. The compensator can cause a nonuniform distribution of velocity in the test section. A design of wind tunnel parts is illustrated in drawing documentation. Drawing documentation is part of the attachment.

5.2 Influence of the driving fan

Two phenomena may occur in the flow because of inappropriate fan design. The fluctuations of the velocity field caused by the fan vanes or the impeller and vibration of the wind tunnel construction are investigated.

To assess the influence of the driving fan on the flow in the test section, experiments with the CTA measurement system (Dantec dynamics A/S) were performed. The measurement took place in the middle of the test section. The sampling frequency of 10 kHz was used with a duration of 60 s, 600 000 samples were obtained. 1D CTA probe was used.

There are 42 vanes in the fan. The vane frequency was determined by equation 5.2. The vane frequency was determined for four different frequencies of the frequency converter (10, 20, 30, 40 Hz). Results are outlined in Table 5.1.

$$f_v = \frac{RPM_{fan}}{60} n_v \tag{5.2}$$

Table 5.1 *Vane frequency*

f_f [Hz]	RPM_{fan} [$1/min$]	f_v [Hz]
10	287	201
20	574	402
30	861	603
40	1148	804

From the results obtained by 1D CTA measurement, frequency spectra were derived (see Figure 60).

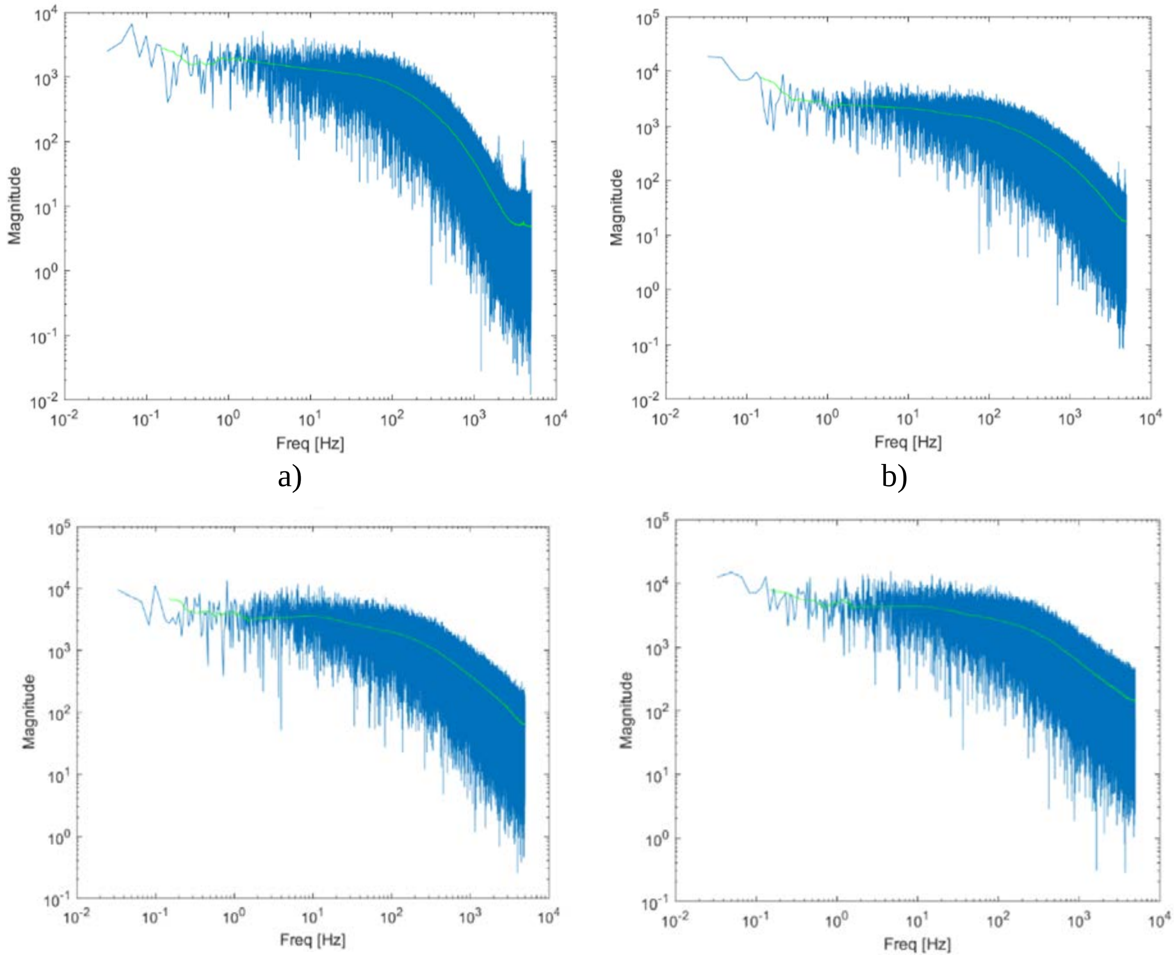

a) b) c) d)

Figure 60 *Velocity spectra for a) 10 Hz, b) 20 Hz, c) 30 Hz, d) 40 Hz*

In Figure 60 a), there are two dominant peaks on frequencies, 2015 Hz and 3995 Hz. In Figure 60 b), there is only one dominant peak with frequency of 3995 Hz. On other regimes, the peaks are not visible.

5.3 Influence of the compensator

The part which connects the fan and the movable wind tunnel construction may have an adverse effect on the flow quality in the test section. Disturbances of velocity profile might occur during the movement of the tunnel to the limiting positions. Extreme positions are illustrated in the test section in Figure 61. The influence of the compensator on the flow for one extreme position can be seen in Figure 62.

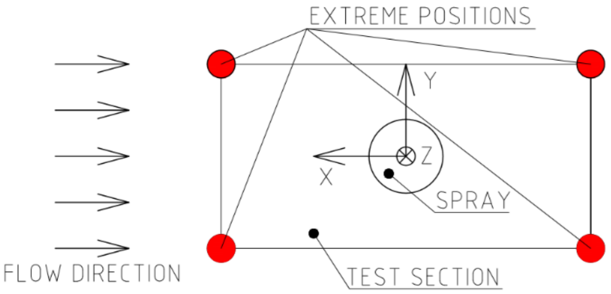

Figure 61 *Extreme position for movement*

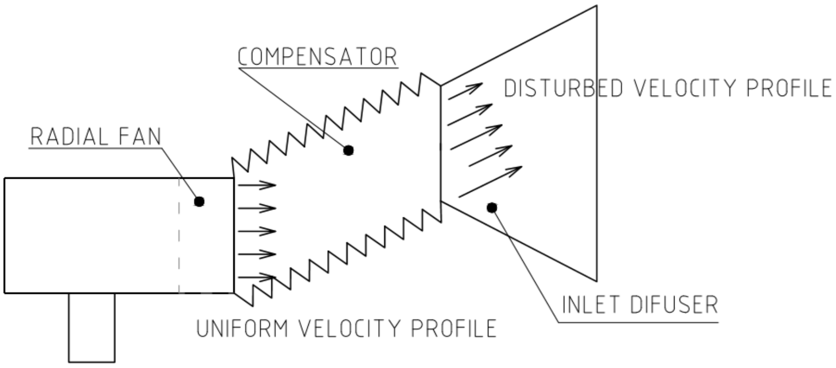

Figure 62 *Influence of compensator on the velocity flow field*

The experiments were performed to investigate the influence of the compensator on the flow quality in the test section. The CTA measurement system was used with two-dimensional probe type 55 R61, measuring two components of velocity, axial component (*U*), and radial component (*V*). In the wind tunnel, one dimensional vector field is required with the ratio *U/V* near zero. Sampling frequency was set to 5 kHz and the measurement duration was 4 s. The set of 20 000 raw data was obtained. The measurement points are illustrated in Figure 63.

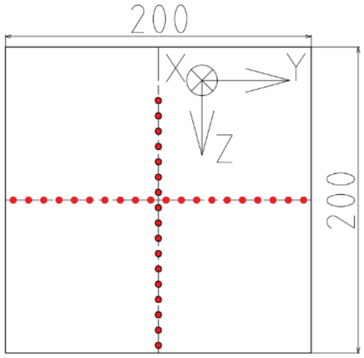

Figure 63 *Measurement points*

Experiments were performed for four different fan rotation speeds, but results are presented only for 40 Hz in Figure 64. The compensator has no impact on the turbulent intensity and velocity profile in the test section. The ratio of axial velocity to radial velocity was under 5% for all cases.

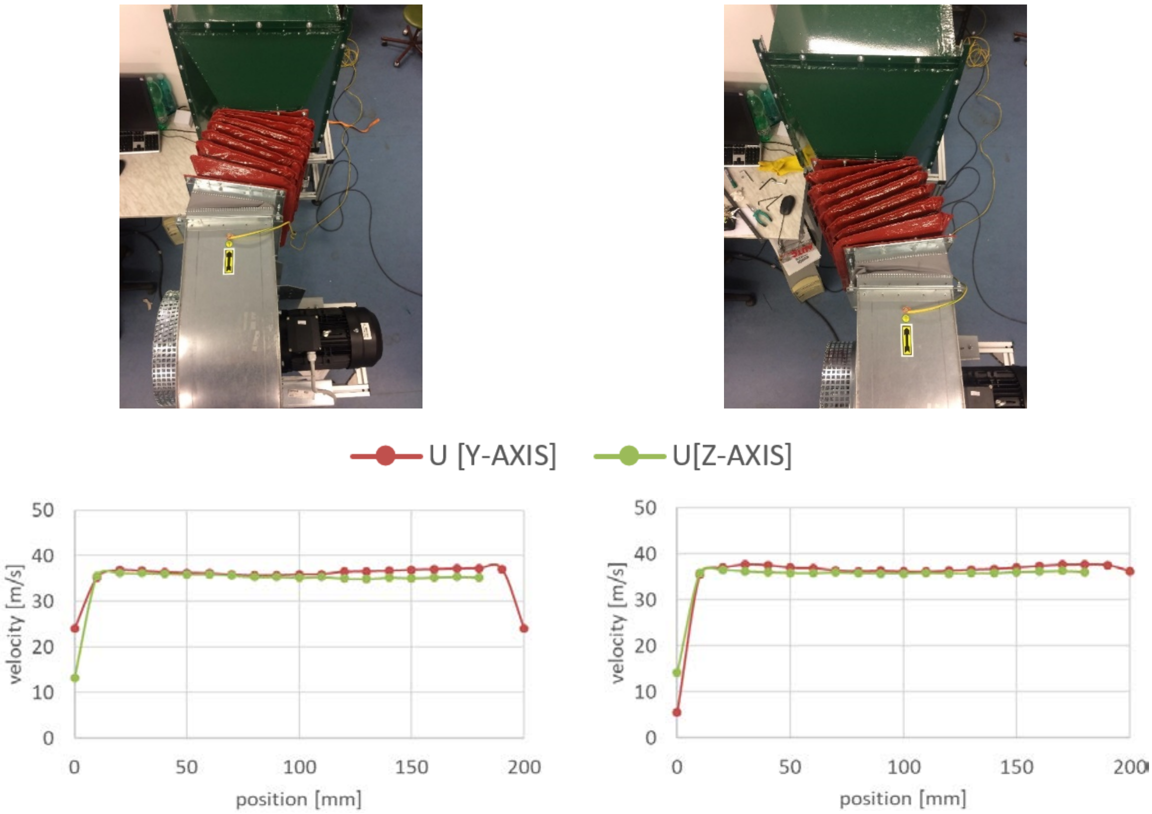

Figure 64 *Velocity profile in Y and Z axes for extreme positions*

5.4 Vibrations

I would like to thank Guilherme Augusto D. da Silva for performing the vibration analysis of the wind tunnel structure. Chapter 5.4 is taken over from his report [77] and slightly modified for the purpose of this thesis. Vibrations of the driving fan or flow-induced vibrations of the wind tunnel construction have an impact on the measurement accuracy. The use of the compensator and rigid material for the wind tunnel construction suppress the vibration propagation.

The airflow source is a motor driven fan; this mechanical conjunct is also a source of large mechanical vibrations that can be transmitted to the wind tunnel construction. The analysis of the source is important as it correlates with the structure vibrations themselves. If the severity of structure vibrations is too high, it can disturb the airflow, inducing measurement errors. The analysis of some flow parameters and their correlation with vibrations are essential to characterize the performance of the device.

Measurements of the wind tunnel vibrations were performed using the data analyser Photon+ and the software RT-Pro and three accelerometers, one 4533-Band, and two 4534 - B. They were positioned on the top of the fan, at the beginning of the settling chamber and at the end of the laminarization section. For monitoring the rotation, a laser tacho probe Type 2981 was used. In order to better analyse the data, the recording function of the RT- Pro was used. Accelerometers were attached to the structure using magnetic holders and connected to the Photon+ channels using coaxial cables of AO-0531 type. The experimental setup is illustrated in Figure 65.

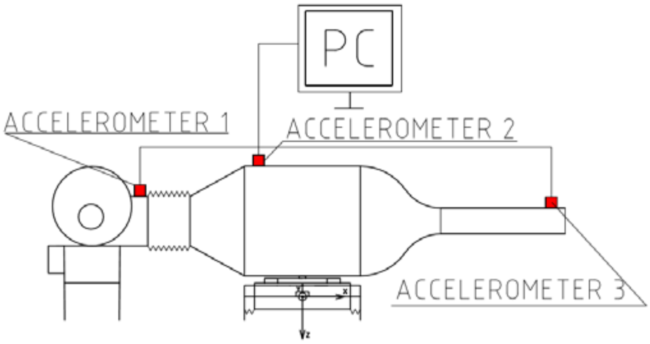

Figure 65 *Experimental setup*

Four different setups (different fan rotation speeds) were tested. For simplicity, only the results for 40 Hz are presented. The signals obtained were temporal series, and all the calculations and processing were made using a MATLAB script.

The fan rotation speed for 40 Hz is 1148 rpm. Higher peaks are present at around the 6th and the 10th order. A vibration order tracking analysis of fan is illustrated in Figure 66.

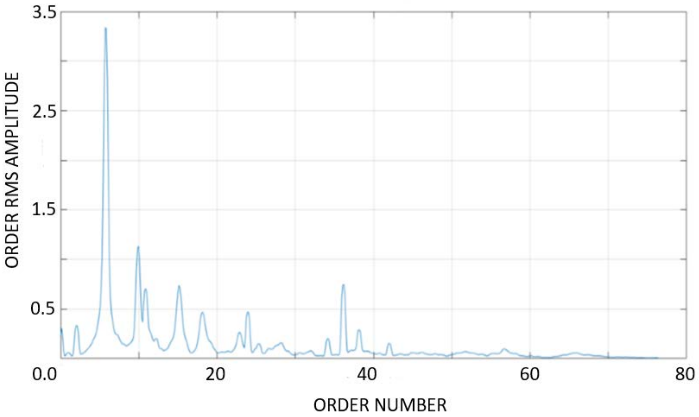

Figure 66 *Order tracking analysis*

It is most likely that peaks are related to the parts of the fan such as bearings, motor coils, stator and rotor, or even the number of shaft keys.

The cross-correlation between the accelerometer signals was evaluated. It is possible to see that the correlation between all possible pairs of accelerometers is still low even though a high correlation was expected between the accelerometers attached to the wind tunnel construction. The cross-correlation function can be seen in Figure 67.

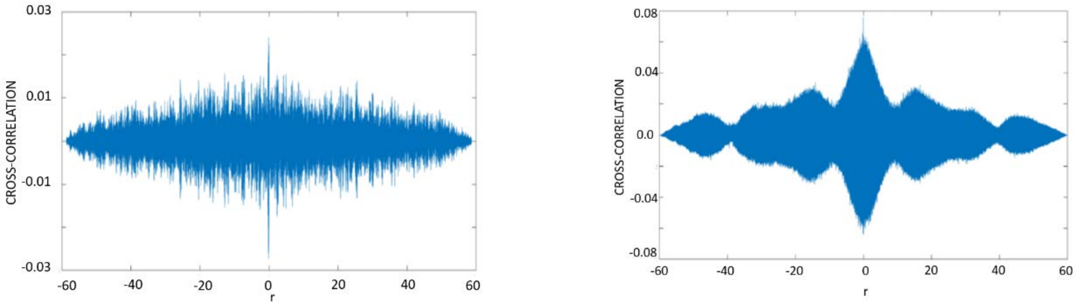

Figure 67 *Cross-correlation of accelerometers 1 and 2 (left), 1 and 3 (right)*

From this result, we can say that vibrations from the driving fan do not spread to the wind tunnel construction. The compensator has a high damping ability.

Using the data analyser Photon+, two accelerometers (type 4534-B), a microphone, and a hotwire anemometer, it was possible to measure vibrations, pressure fluctuations in the tunnel, and the flow velocity. Based on the previous measurements, it was decided that the points for measuring the vibrations should be only in the structure of the wind tunnel as the correlation between the fan vibrations and the structure vibrations is too low. In order to keep the track of the rotation of laser, the tacho probe (type 2981) was used. The accelerometers were positioned on the top of the settling chamber and on the top of the laminarization section of the tunnel. From this setup, flow-induced vibrations can be recognized. The data from the accelerometers are presented in Figure 68. The blue and red lines represent the accelerometers 1 and 2, respectively. Accelerometer 1 is placed at the outlet structure of the laminarization section. Accelerometer 2 is placed at the beginning of the settling chamber.

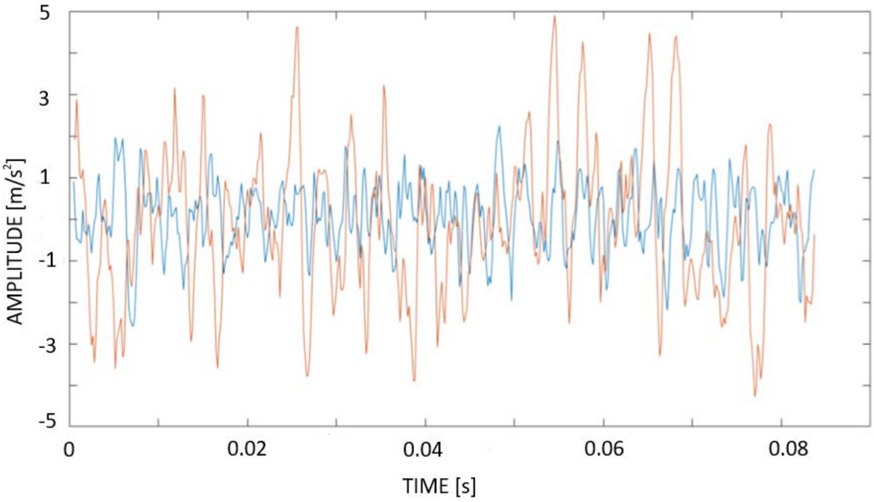

Figure 68 *Data from accelerometers*

The pressure signal obtained during the measurement is illustrated in Figure 69. These experiments were performed at the early design stages (first wind tunnel design) without the design changes. The turbulent intensity in the test section was approximately 5%.

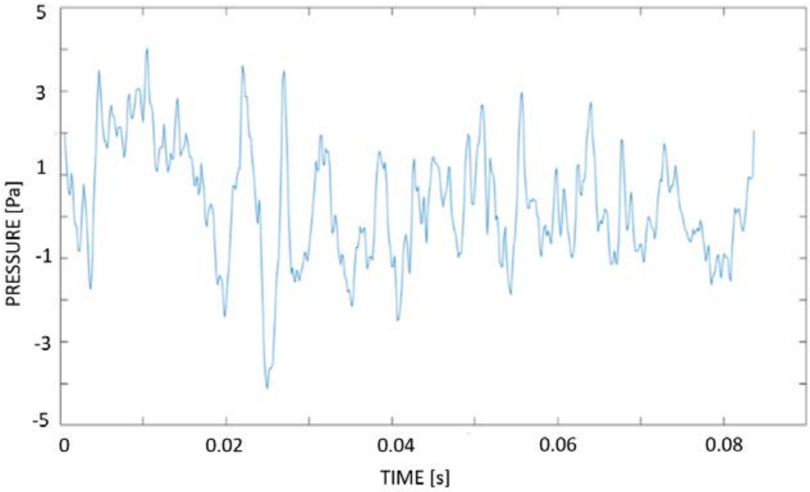

Figure 69 *Pressure fluctuation*

The cross-correlation was performed for the accelerometer 1 and pressure fluctuations. The result is presented in Figure 70.

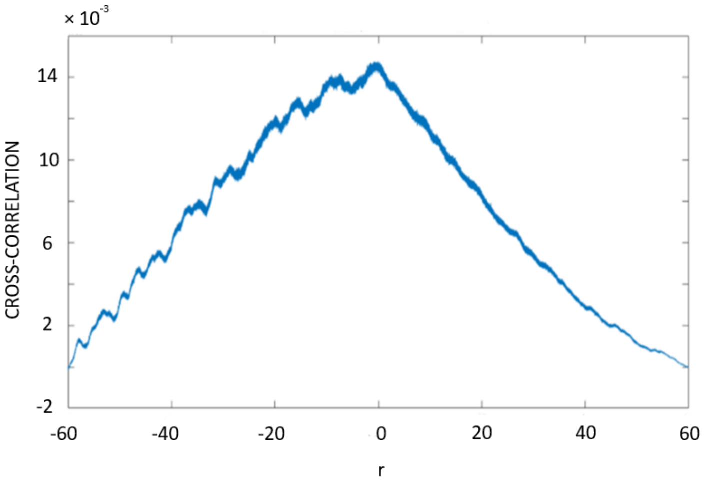

***Figure 70** Cross-correlation between the accelerometer 1 and pressure fluctuations*

From the analysis of the results, it follows that the flow causes vibrations of the wind tunnel construction. This phenomenon can be easily limited by a more rigid structure.

5.5 Turbulence intensity control

The controllable and well-defined turbulence in the test section is required in the wind tunnel. There are several ways how to control (increase/decrease) the turbulence in the test section. Active and passive methods are usually used. The essence of the passive method is the usage of static grids (meshes) illustrated in Figure 71. These grids are used to either decrease the level of turbulence intensity or to increase the turbulence intensity. They generate turbulence if the Reynolds number based on wire mesh diameter is high enough [78]. Active methods are illustrated e.g. in Figure 72. This active control is composed of several axes; every axis is connected to a servomotor and controlled separately. By rotating the axes, it is possible to control the turbulence. This approach is still under development and it is an expensive solution. The first turbulence control was proposed by [79]. Next approach how to generate the user defined turbulence is by using velocity flows with different magnitudes or directions. The fans on the top and bottom of the test section are used. These fans provide a horizontal flow which generates turbulence [80].

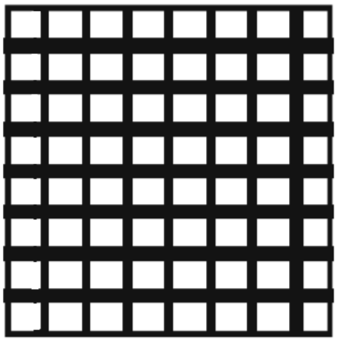

***Figure 71** Passive grids*

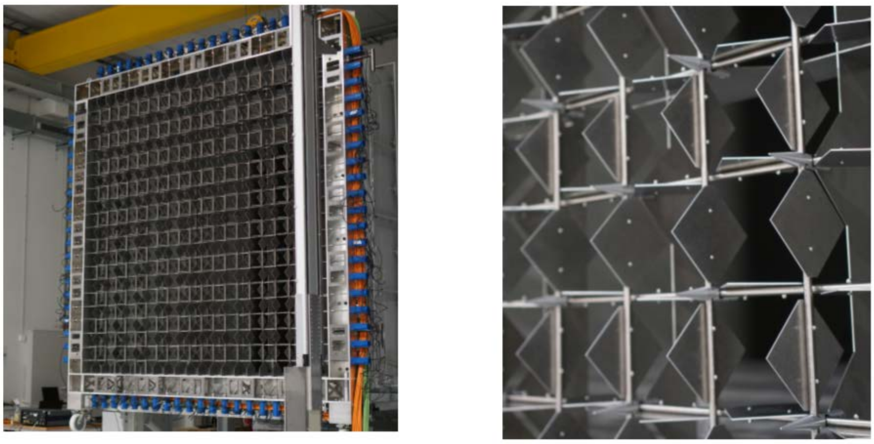

Figure 72 *Active grids [81]*

Static grids were used to generate turbulence in this tunnel. Experiments were performed using PDA measurement system. Two velocity components (*U*, *V*) were measured. The frequency of 10 kHz and duration of 5 s in each position were used. The PDA setup is outlined in Table 5.2. The flow was seeded using a fog generator. Seeding particles with diameter less than 3 μm were used as they follow the flow well. The Stokes number of particles was less than 1, even for maximum velocity. Velocities were measured in two planes. Plane 1 is placed 60 mm away from the test section inlet and plane 2 is placed 160 mm away from the test section inlet. In each plane, 11 measurement points are defined. The schematic layout of measurement points and grids positions are presented in Figure 73. The grids were placed in different positions across the length of the laminarization section, at least 20 times the width of mesh square from the test section inlet.

Table 5.2 *PDA setup*

Laser power output	300 mW	
Wavelength	488 nm	514.5 nm
Focal length of transmitting optics	310 mm	310 mm
Focal length of receiving optics	500 mm	500 mm
Scattering angle	45 °	45 °
Mask	A	A
Spatial filter	0.1 mm	0.1 mm
Sensitivity	980 V	1280 V
SNR	0 dB	0 dB
Signal gain	16 dB	8 dB
Level validation ratio	8	2

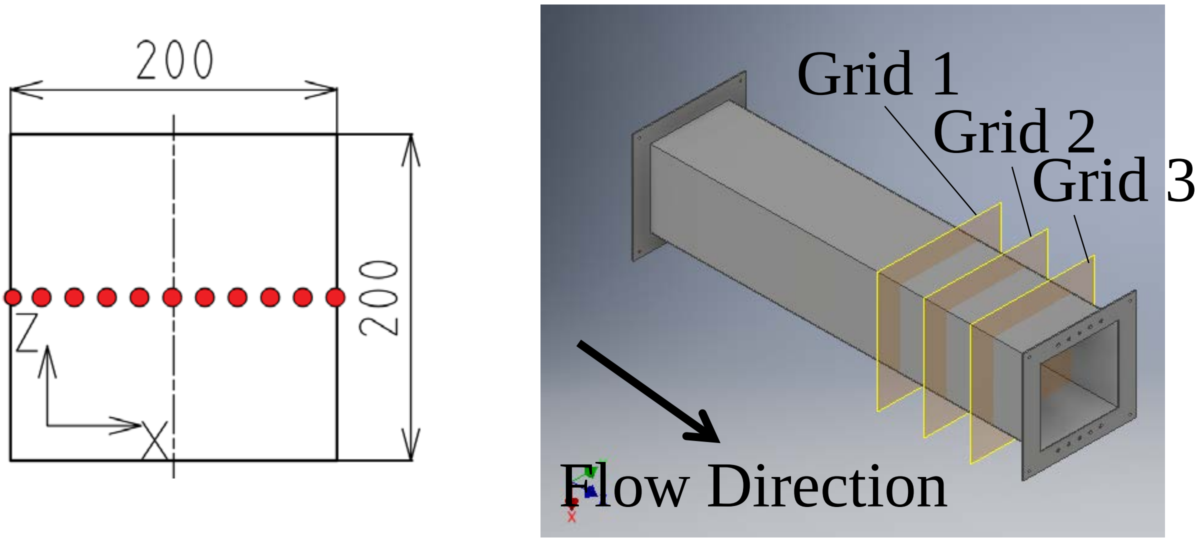

Figure 73 *Measurement points and grid positions*

The goal of these experiments was to assess the turbulence generated by grids of different size. The parameters that describe the grid are the parameter *d* (wire mesh diameter) and the parameter *M* (the width of the grid square). The parameter that usually describes the grid is the grid porosity, defined by equation (5.3). The schematic layouts of the grids are illustrated in Figure 74, and geometrical parameters are outlined in Table 5.3. Grids were tested for different fan rotational speeds (10 Hz, 20 Hz, 30 Hz and 40 Hz).

$$\beta = \left(1 - \frac{d}{M}\right)^2 \tag{5.3}$$

The variables in equation 5.3 are apparent from Figure 74. The grids have almost the same porosity but vary in wire mesh diameter and width of the grid square.

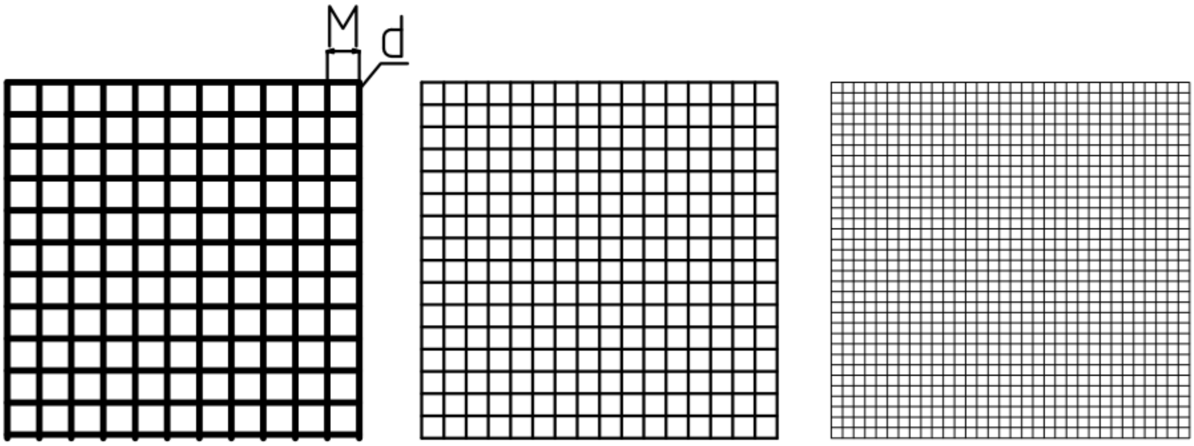

Grid 1 Grid 2 Grid 3

Figure 74 *Grids*

Table 5.3 *Grid parameters*

	Mesh 1	*Mesh 2*	*Mesh 3*
d [mm]	1.3	0.75	0.5
M [mm]	18	12	6
β [mm]	0.86	0.88	0.84

The grids were tested, and a combination of different grids were tested. Test cases are summarized in Table 5.4.

Table 5.4 *Test cases*

***f* [Hz]**	**Plane 1**	**Plane 2**
10	No grid, Grid 1, Grid 2, Grid 3, Grid 1+2, Grid 1+2+3, Grid 2+3	
20		
30		
40		

It is favourable to obtain constant turbulent intensity across the cross-section of the test section and also the constant Turbulent intensity across the length of the test section. The turbulent intensity for different grids and fan rotation speeds is illustrated in Figure 75.

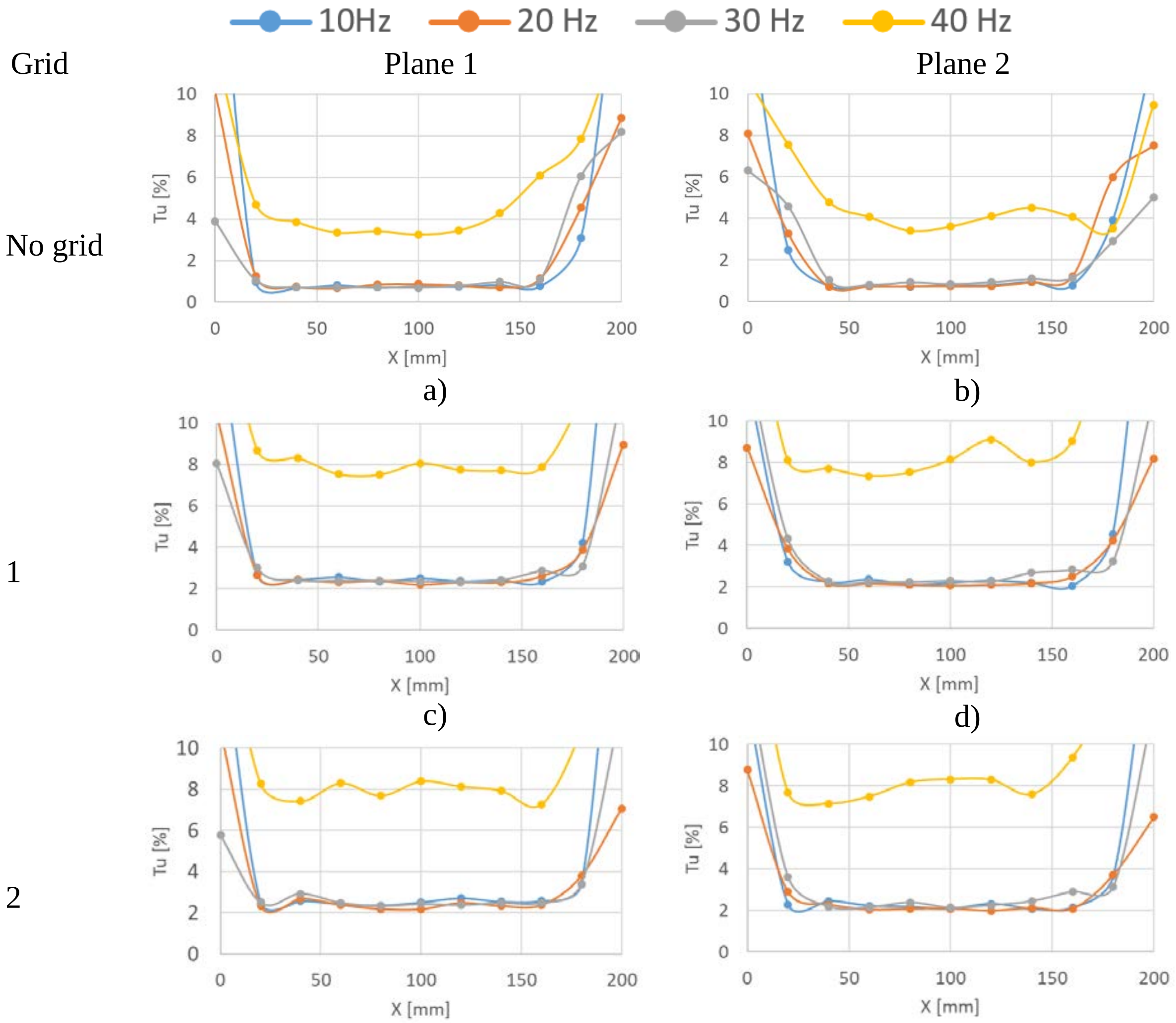

a) b) c) d) e) f)

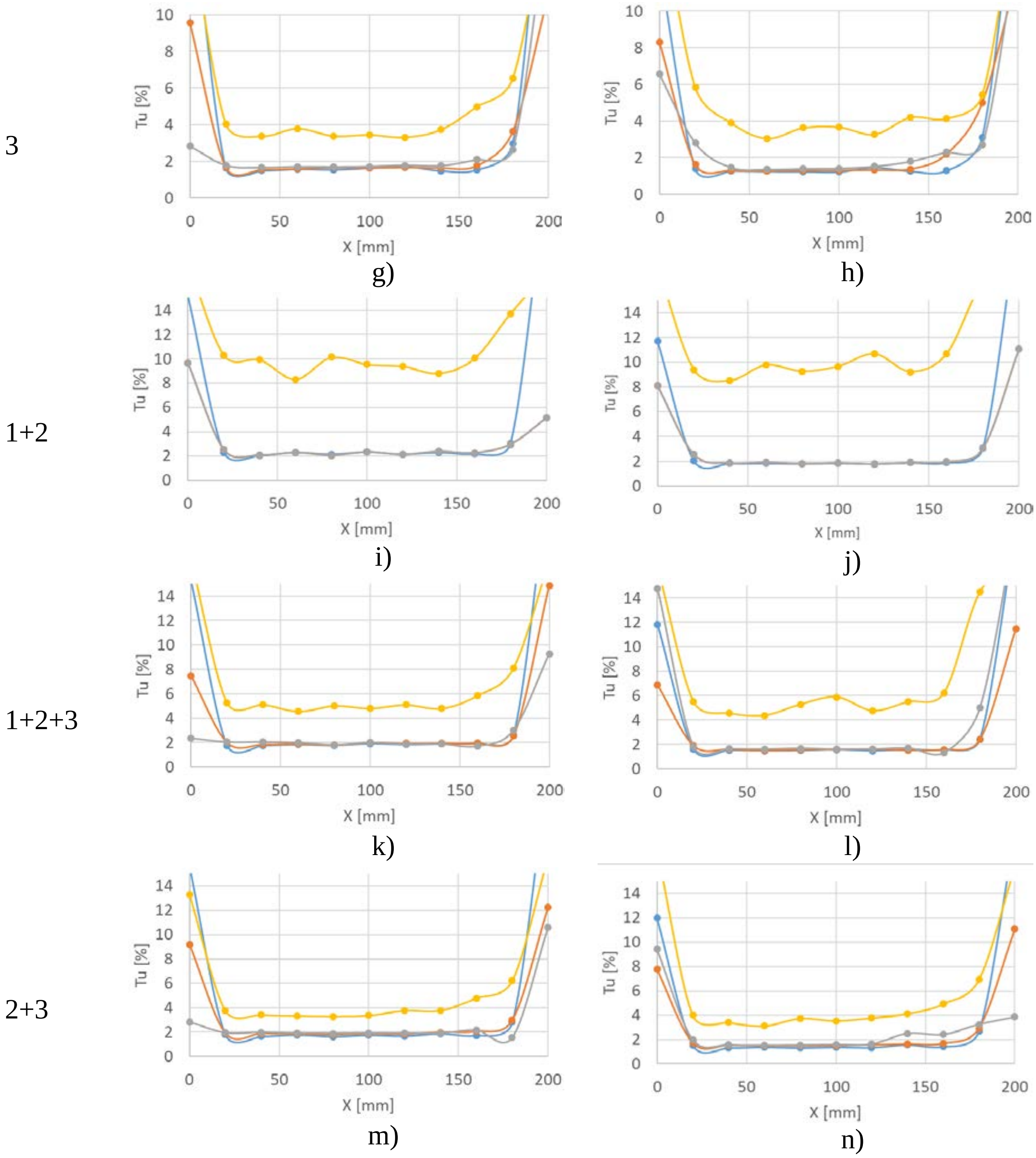

***Figure 75** Influence of grids on turbulent intensity*

From Figure 75, it is apparent that grids influence the turbulent intensity. There is no big difference between the grids alone and a combination of grids in turbulent intensity. The turbulent intensity in each case is approximately 2%. The turbulent intensity without the grids is approximately 0.7%. The relative increase in turbulent intensity is 280%. For 40 Hz, the turbulent intensity is higher than that for other regimes. It is caused by the PDA measurement system; the real turbulent intensity is approximately the same as for other regimes. Higher turbulent intensity can be caused by non-uniform fringe spacing and noise of the PDA processor because the turbulent intensity was measured by the blue beams working on relatively low laser power. This is apparent from Figure 76 where the velocity is plotted against the arrival time of the particle.

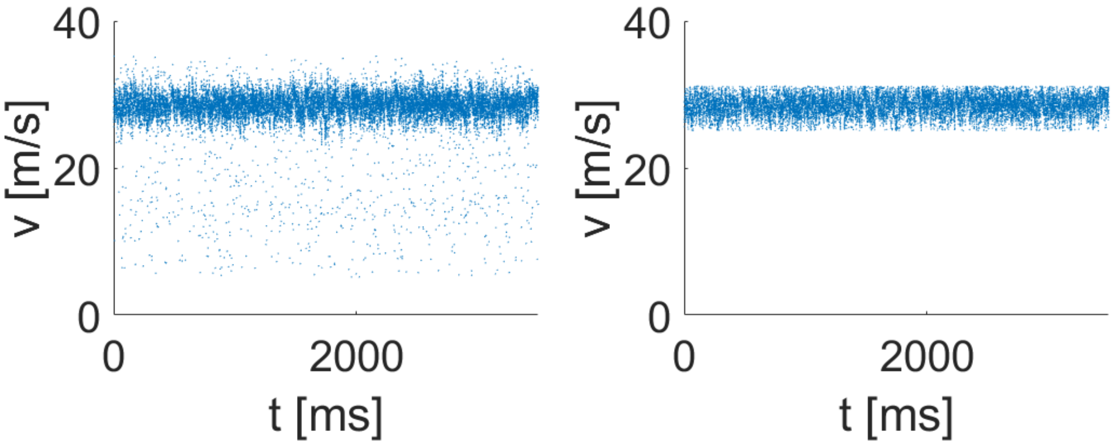

Figure 76 *Unfiltered PDA data (left) and filtered PDA data (right)*

In Figure 76 left, there are a lot of dots created by the PDA system. Basically, it is noise generated by the system. These peaks do not reflect the flow behaviour. The filtered data are presented in Figure 76 right, where velocities higher and lower than three times the standard mean deviations were rejected. Data in Figure 76 represents the 40 Hz regime in the middle of the test section with no grid. In Figure 76 left, the turbulent intensity is higher than 3%, and in Figure 76 right, the turbulent intensity is 0.8%. The turbulent intensity for 40 Hz is similar to the other regimes after data filtration at all regimes.

In Figure 77, the velocity profiles for a different combination of grids and velocity regimes are illustrated. From Figure 77, it is apparent that the combination of grids has a large pressure loss. It is caused by the placement of the grids in the laminarization section with a small hydraulic diameter (high velocity). It is convenient to use only grids 1, 2 or 3 individually. These cases have a small pressure loss. The pressure loss can be computed by equation 5.4, which is similar to equation 1.5.

$$\Delta p = K\rho \frac{U^2}{2} \tag{5.4}$$

Where *K* is the pressure resistance coefficient. *K* is a function of the grid porosity and the Reynolds number (based on the wire diameter) [82]. Equation 5.5 represents the pressure resistance coefficient.

$$K = f(Re_d)\frac{1-\beta^2}{\beta^2} \tag{5.5}$$

● No mesh ● Mesh 1 ● Mesh 2 ● Mesh 3 ● Mesh 1+2 ● Mesh 1+2+3 ● Mesh 2+3

f [Hz]	Measurement plane 1	Measurement plane 2
10	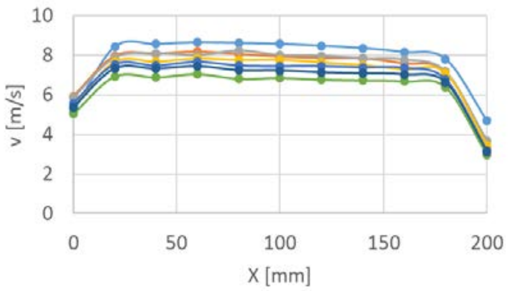 a)	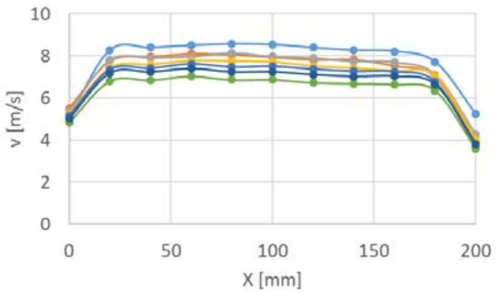 b)

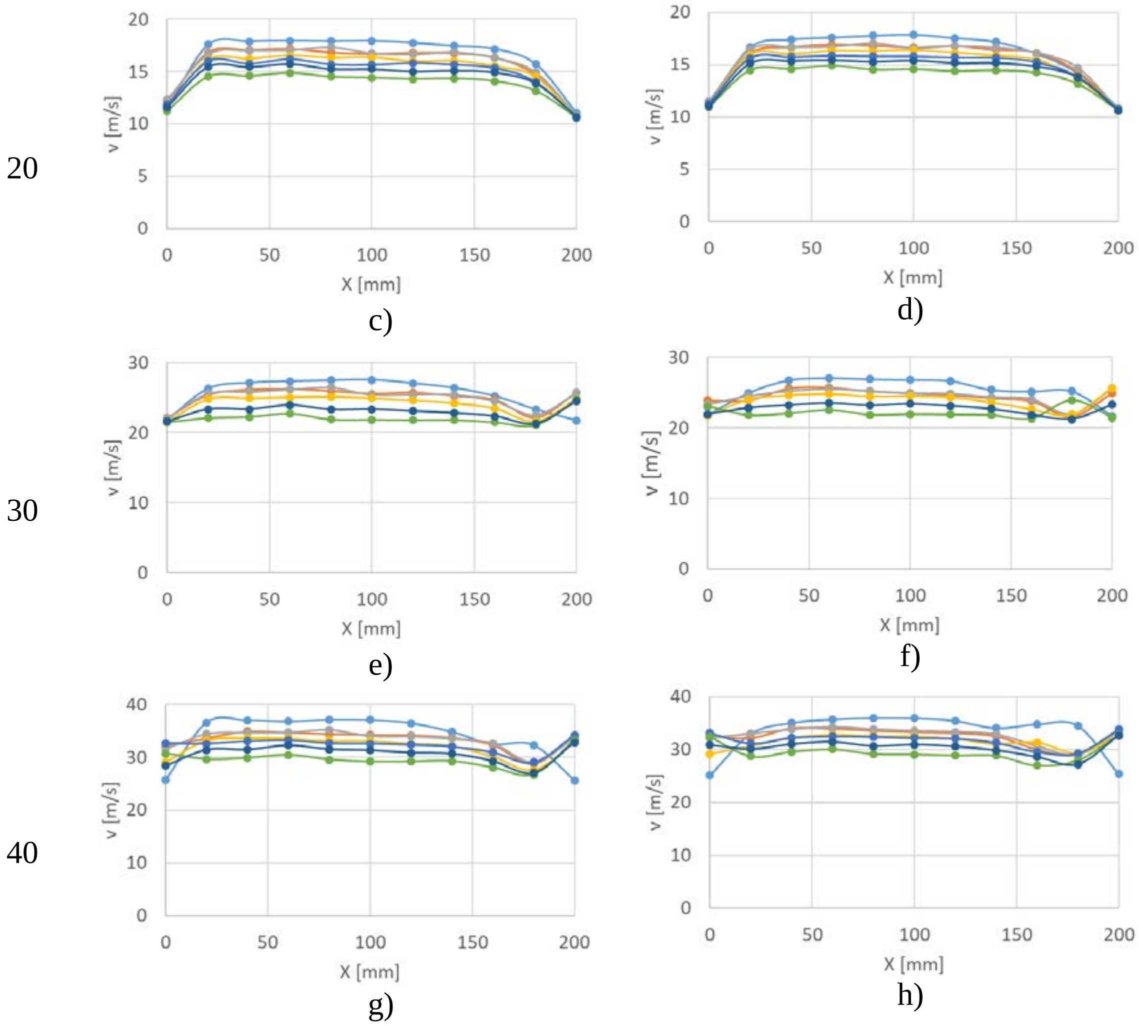

***Figure 77** Velocity profile for different grids and regimes*

For a proper definition of turbulence, the turbulent intensity and length scales are important to define. In this section, two length scales are defined. These scales were determined by the approach described in [83]. Length scales were defined in two planes in the middle of the flow for all cases outlined in Table 5.4.

Integral and dissipation length scales were determined. The integral length scale characterizes the mean dimension of energy containing vortices. Dissipation length scales represent a measure of the smallest vortices, where dissipation processes dominate [84].

The length scales for different regimes, grid combinations, and two measurement planes are outlined in Table 5.5.

***Table** 5.5 Length scales*

		Integral length scale [m]		**Dissipation length scale [m]**	
f [Hz]		Plane 1	Plane 2	Plane 1	Plane 2
10	No mesh	0.0029	0.0029	5.7980e-04	5.7980e-04
	Mesh 1	0.0022	0.0031	5.6196e-04	5.8041e-04
	Mesh 2	0.0021	0.0021	4.5891e-04	4.5891e-04
	Mesh 3	0.0065	0.0038	7.1613e-04	5.5709e-04
	Mesh 1+2	0.0036	0.0027	0.0014	0.0015
	Mesh 1+2+3	0.0023	0.0034	6.7667e-04	6.1653e-04
	Mesh 2+3	0.0029	5.7980e-04	5.7980e-04	5.7980e-04
20	No mesh	0.00465	0.0230	0.0011	0.0013
	Mesh 1	0.0056	0.0075	0.0016	0.0016
	Mesh 2	0.0036	0.0017	0.0015	0.0017
	Mesh 3	0.0064	0.0097	0.0011	8.8316e-04
	Mesh 1+2	0.0053	0.0061	0.0029	0.0032
	Mesh 1+2+3	0.0048	0.0046	0.0011	0.0015
	Mesh 2+3	0.0053	0.0088	0.0010	0.0011
30	No mesh	0.00264	0.0072	0.0014	0.0011
	Mesh 1	0.0054	0.0201	0.0021	0.0023
	Mesh 2	0.0059	0.0113	0.0025	0.0022
	Mesh 3	0.0043	0.0097	0.0017	0.0018
	Mesh 1+2	0.0053	0.0061	0.0029	0.0032
	Mesh 1+2+3	0.0033	0.0074	0.0020	0.0022
	Mesh 2+3	0.0038	0.0111	0.0013	0.0016
40	No mesh	0.0036	0.0078	0.0010	0.0014
	Mesh 1	0.0018	0.0016	0.0016	0.0015
	Mesh 2	0.002	0.002	0.0018	0.0018
	Mesh 3	0.0018	0.0028	0.0013	0.0017
	Mesh 1+2	0.0017	0.0017	0.0014	0.0014
	Mesh 1+2+3	0.0018	0.0026	0.0015	0.0024
	Mesh 2+3	0.0022	0.0043	0.0011	0.0015

There is a difference between the length scales in measurement planes 1 and 2. The dissipation length scale is smaller than the integral length scale.

It is required to obtain isotropic turbulence in the test section. The isotropic turbulence may be present further downstream from the grid. Figure 78 illustrates the ratio of v_{rms} and u_{rms}. From Figure 78, the isotropic turbulence is not obtained and there is almost no improvement for plane 2. The isotropy is illustrated for mesh 1 for two velocity regimes. The turbulence becomes isotropic at the length larger than 100 × M, in this tunnel arrangement, some degree of anisotropy will always be present.

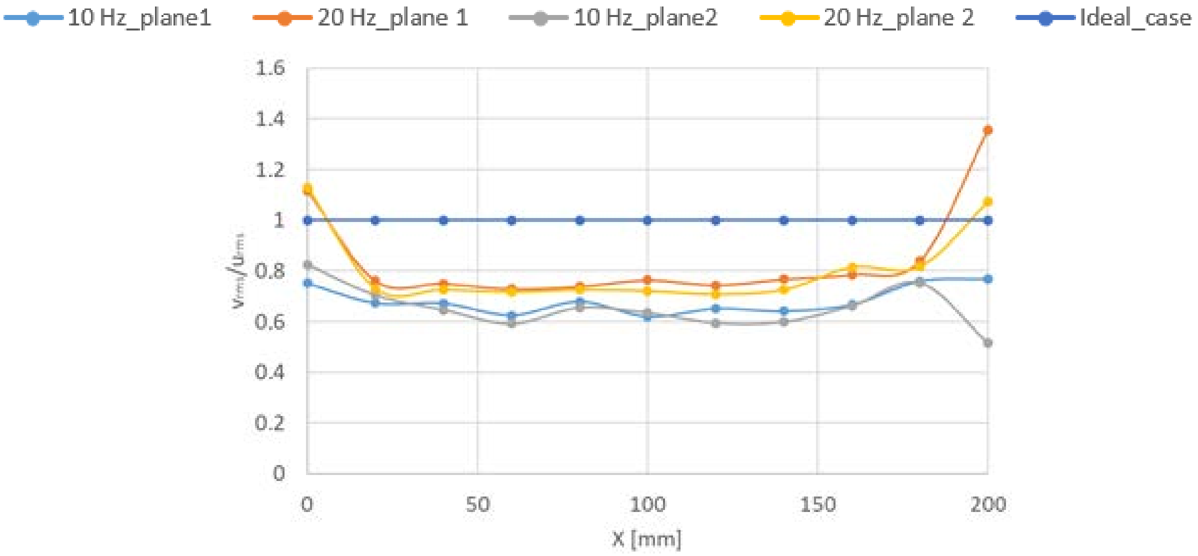

Figure 78 *Isotropy of velocity fluctuations*

6 ALIGMENT OF MEASUREMENT SYSTEMS

This chapter describes the alignment of optical measurement techniques for the measurement of the spray in the wind tunnel. A special care is taken to align the PDA measurement technique. As was mentioned in chapter 4, the test section is equipped with a transparent window from each side. The schematic design of an experimental setup for PDA system, high speed visualization, and PIV method is outlined in Figure 79.

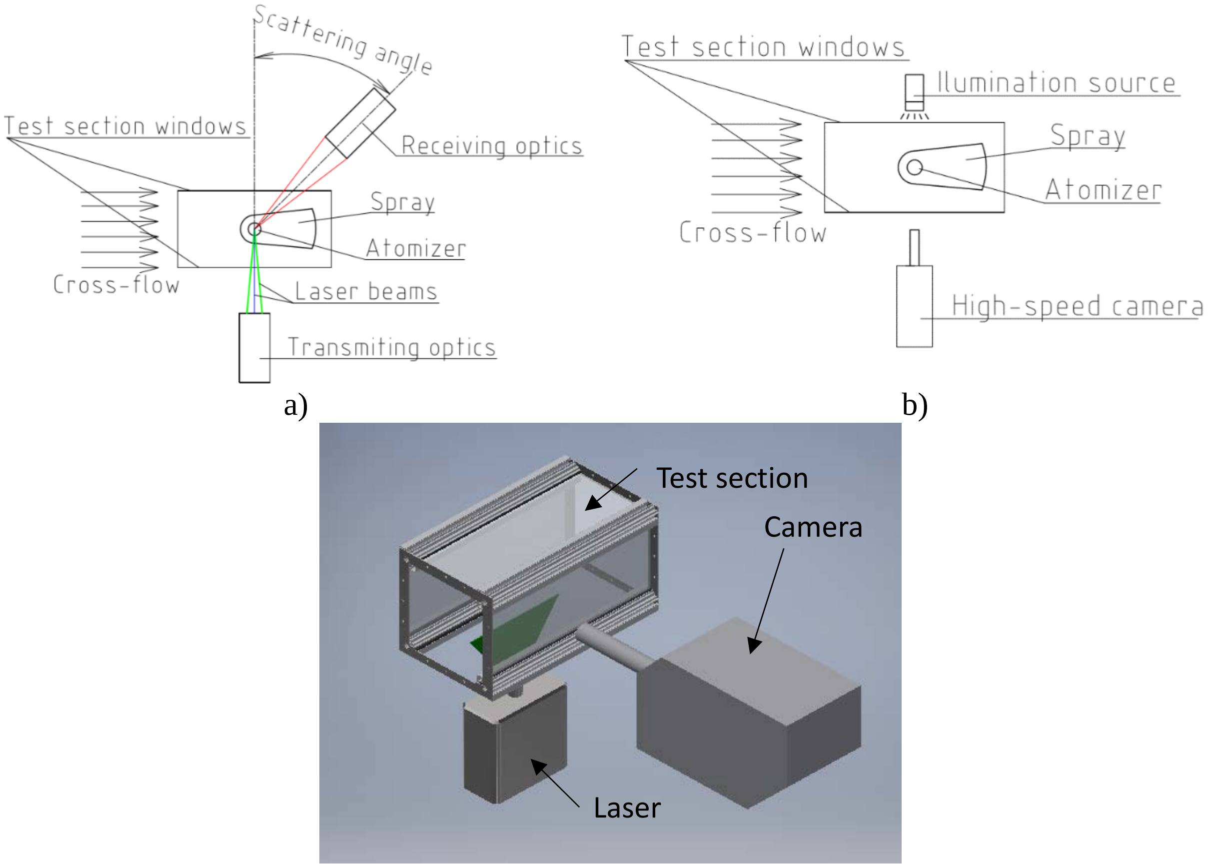

a) b)

c)

Figure 79 *Schematic measurement setups a) PDA setup, b) High–speed visualization, c) PIV setup*

For the PDA measurement system, the influence of test section windows on measurement results and accuracy is investigated. The spray produced by the air-brush nozzle was tested for the setup with and without the test section windows for different scattering angles of 31 °, 41 ° and 59 °. Spray was investigated in two measurement planes. Each plane contains 13 equidistantly spaced dots. The schematic illustration of measurement points can be seen in Figure 80. The axial velocity and the particle diameter for the setups with and without the windows are compared.

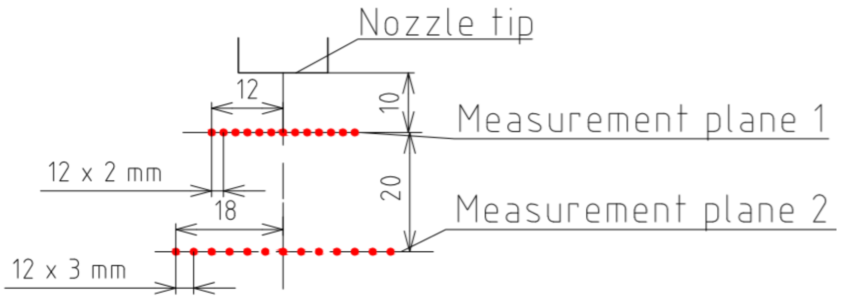

Figure 80 *Experimental setup*

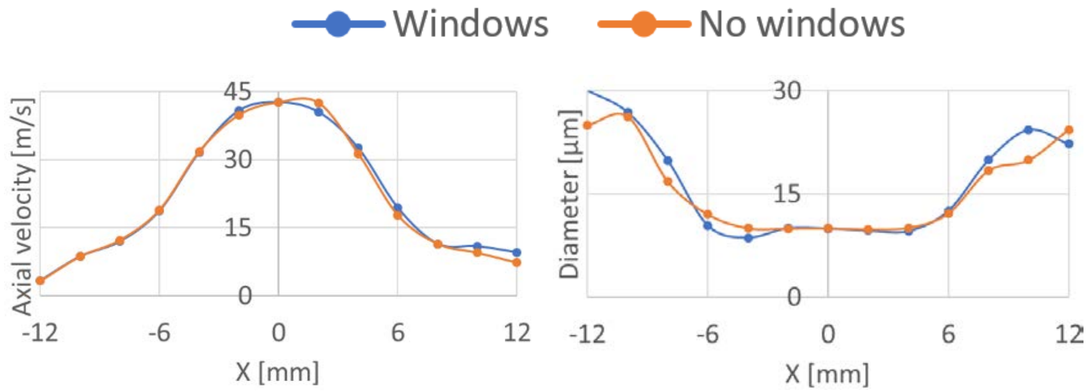

Measurement plane 1

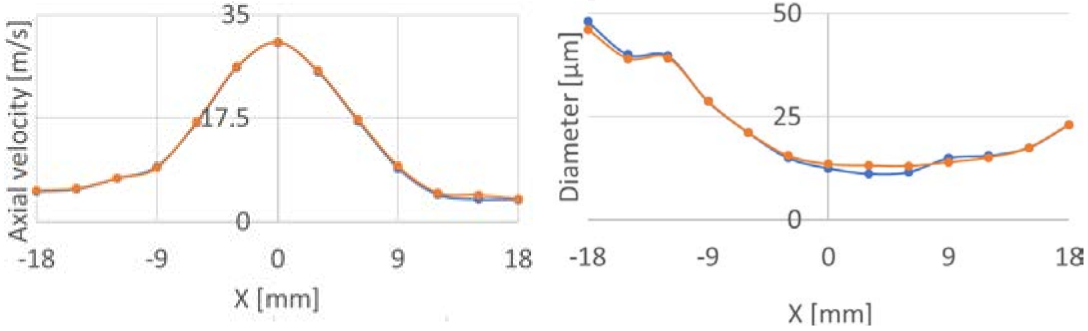

Measurement plane 2

Axial velocity (left) and Particle diameter (right) for 31 °

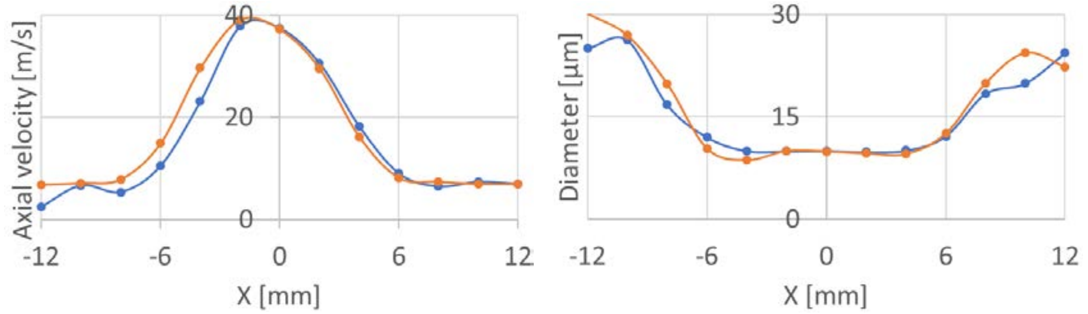

Measurement plane 1

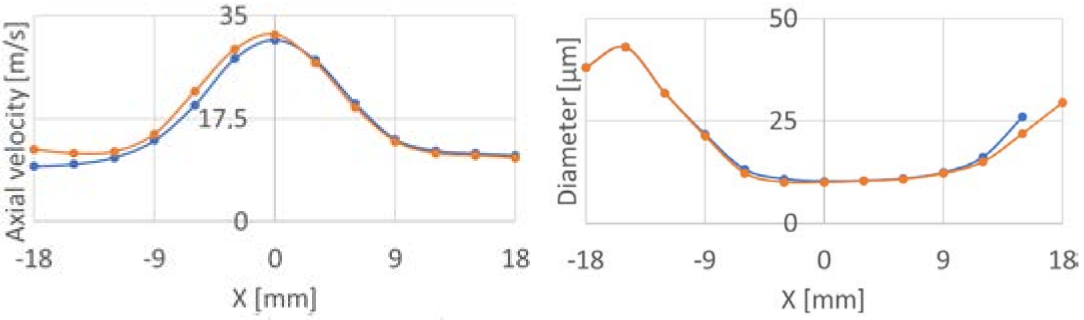

Measurement plane 2

Axial velocity (left) and Particle diameter (right) for 41 °

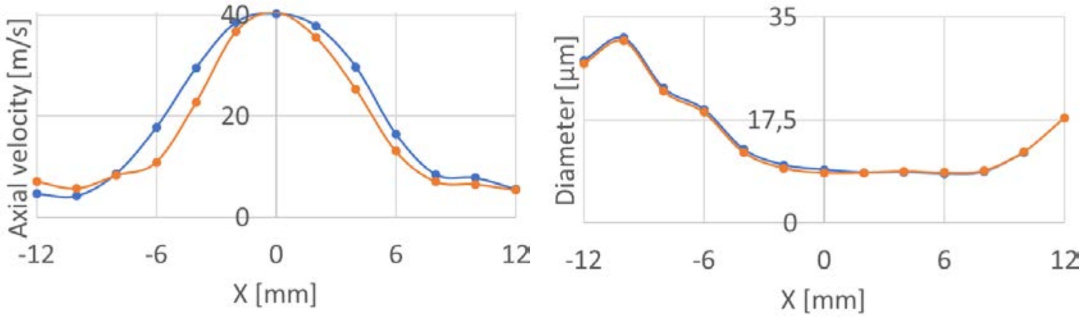

Measurement plane 1

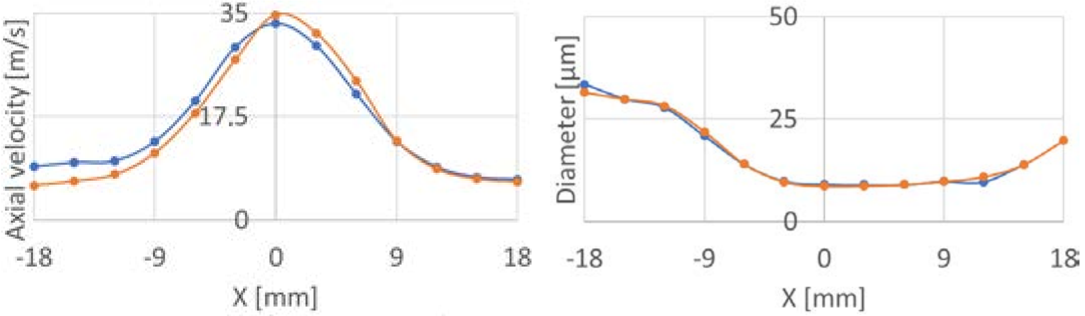

Measurement plane 2

Axial velocity (left) and Particle diameter (right) for 59 °

Figure 81 *Experiment results*

Figure 81 shows that the results are not affected by the presence of windows. The setting of PDA measurement system was the same for every scatter angle setup.

For all measurement techniques, the special care should be taken to reduce fogging of the test section windows and to ensure a good optical access. For high–speed visualization, a fixed holder for the illumination source and a high speed-camera are required. High–speed visualization is a robust measurement technique and no additional care is required. For the PIV measurement technique, it is crucial to ensure that the laser sheet is perpendicular to the test section window and no deflection of a laser sheet is present.

The wind tunnel construction is illustrated in Figure 82. Traverse system is not included. In Figure 83 the wind tunnel in the Spray laboratory is presented. In Figure 84 supporting system is illustrated. In Figure 85 the PDA system and measurement of the spray in wind tunnel is outlined.

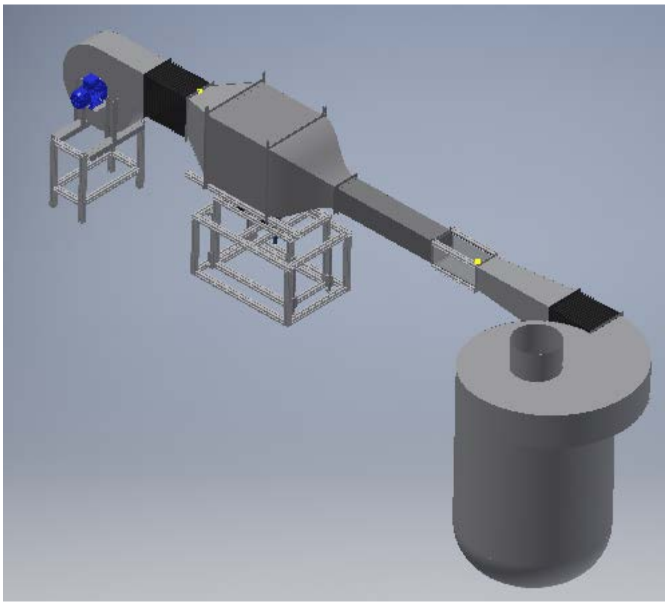

Figure 82 *Wind tunnel construction*

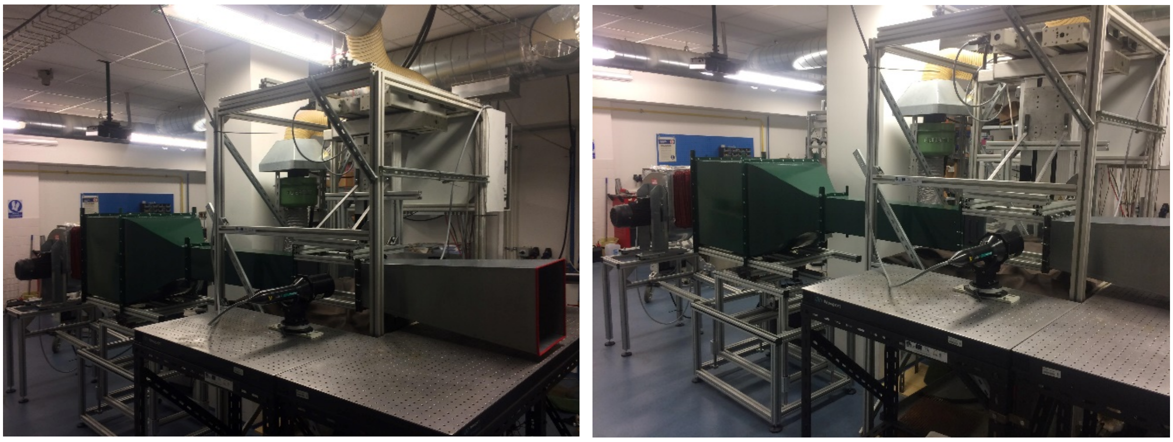

Figure 83 *Wind tunnel construction in Spray research laboratory*

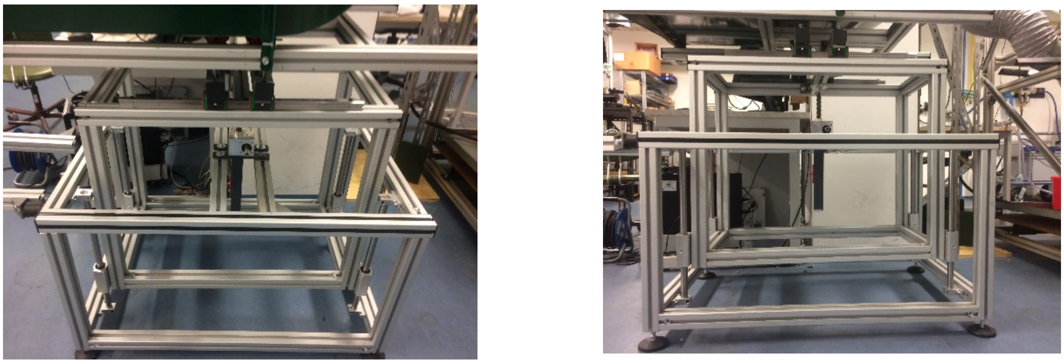

Figure 84 *Detail of supporting system*

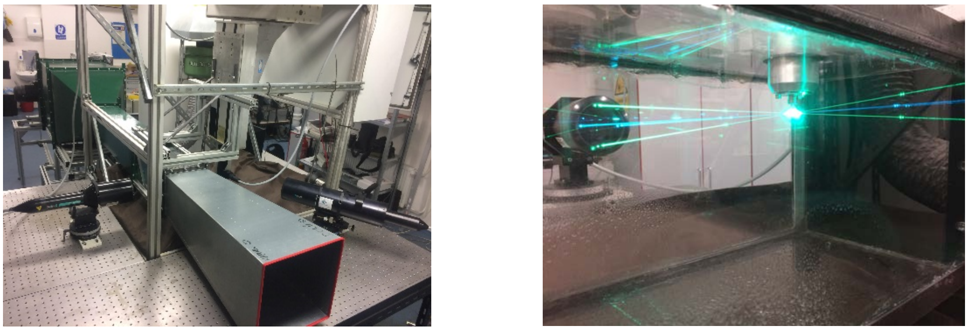

Figure 85 *PDA system arrangement and measurement in wind tunnel*

Wind tunnel is now instrument equipment of the Spray research laboratory at Brno University of Technology [85]. The wind tunnel is a part of patent pending with file number PTC/CZ2020/050012.

7 SPRAY IN CROSS-FLOW EXPERIMENTS

In this chapter, the experiments performed in the wind tunnel to assess the influence of the cross-flow on the spray characteristics are presented.

Formation of hollow cone liquid sheet and spray were investigated by means of high–speed visualization. The effects of the inlet pressure (P_{in} = 2.5, 5 and 10 bar), SFR (SFR is a shortcut for spill-to-feed ratio defined as a ratio of the flow rate through the spill-line to the flow rate through the inlet ports) and the cross-flowing air (velocity in the range 0–25 m/s) on the spray were investigated. The images of the liquid sheet under different cross-flow velocities and *SFR* for the inlet pressure of 2.5 bar are illustrated in Figure 86. The results are shown only for P_{in} = 2.5 bar. The analysis was performed for all assumed inlet pressures (P_{in} = 2.5, 5 and *10* bar).

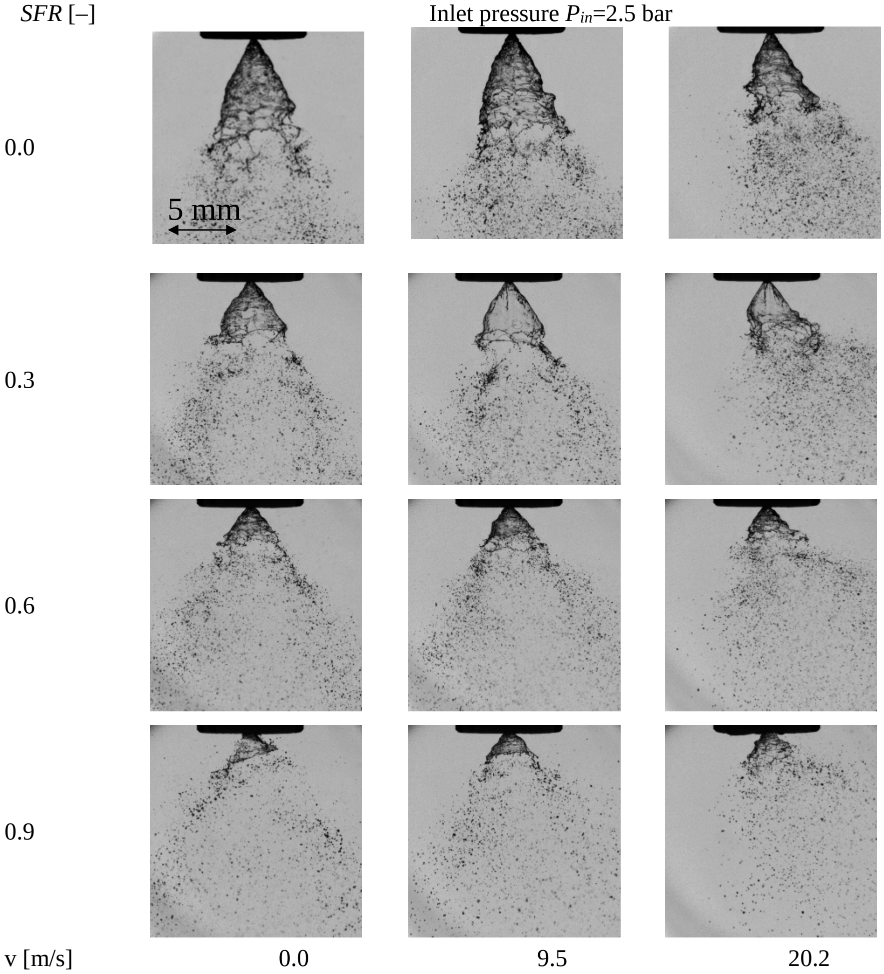

Figure 86 *Spray visualization (experimental data)*

The influence of the flow velocity on the spray behaviour is visible in Figure 86. The momentum of the cross-flow bends the spray in the direction of the cross-flow. The behaviour of the spray is no longer axisymmetric. A higher velocity magnitude bends the spray more rapidly. The smaller droplets are entrained from the spray faster than the larger ones. The larger droplets carry their momentum far downstream from the nozzle tip.

Cone angle

In Figure 87, the influence of cross-flow on the cone angle of the spray is presented. The error bars in Figure 87 represent the standard mean deviation of a cone angle. The increase in the cone angle is caused by the deflection of spray in the direction of cross-flow. The influence of cross-flow on the cone angle is negligible for 10 bars. The initial velocity of a liquid sheet for 10-bar regime is high but the deflection of spray is not so significant.

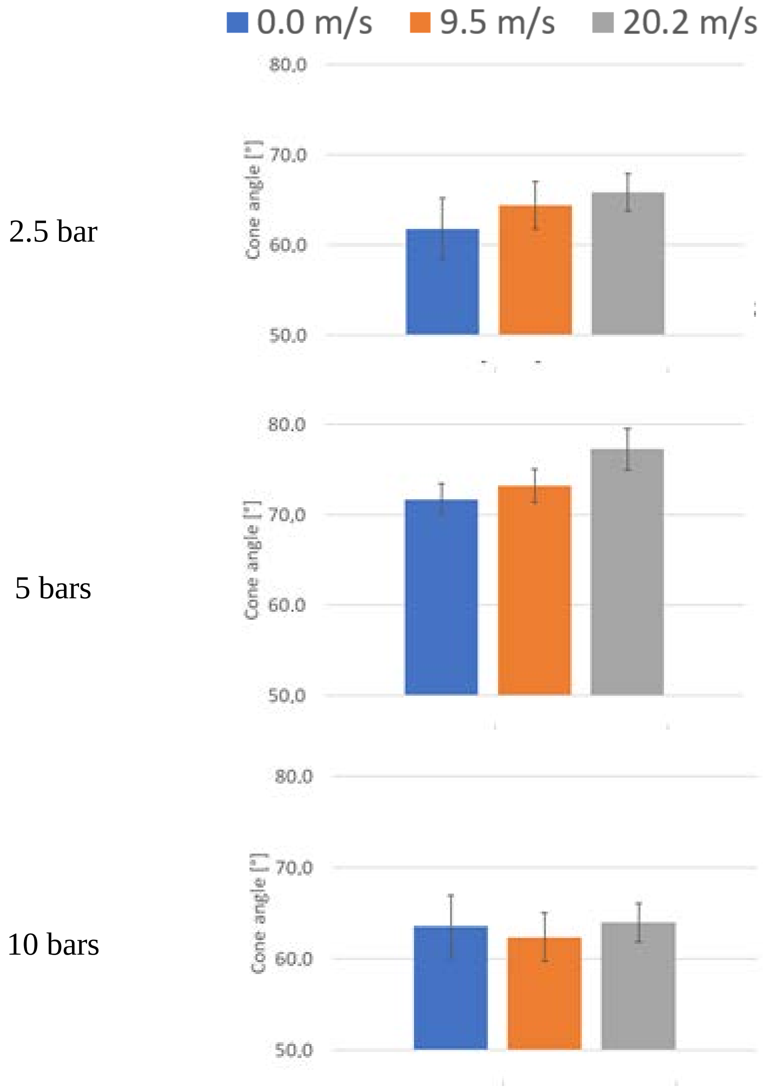

***Figure 87** Cone angle in the cross-flow*

Breakup length

The cross-flow modifies the breakup process of a liquid sheet and can promote the instabilities, which causes a rapid breakup of the liquid film. The promotion of sheet instabilities causes the reduction of breakup length as illustrated in Figure 88. The SFR influences the breakup length of a sheet more than the cross-flow velocity. Increasing SFR reduces the amount of atomized liquid. The sheet has a lower momentum and tends to break up in a shorter distance. A decrease of breakup length with an increase of inlet pressure is also visible.

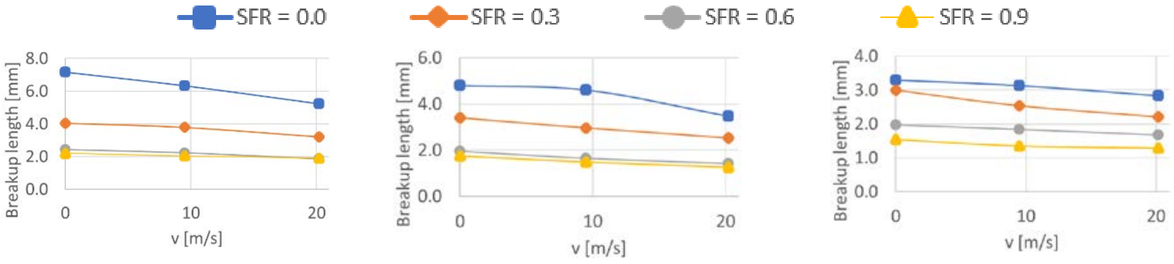

P_{in} = 2.5 Bar P_{in} = 5 Bar P_{in} = 10 Bar

Figure 88 *Breakup length for different P_{in} and SFR*

Spray contour

The cross-flow velocity bends the spray in the direction of the cross-flow. A MATLAB code was written for the detection of the spray boundaries from the mean image. The spray contour for inlet pressure 2.5 bar, *SFR* = 0 and different cross-flow velocities are illustrated in Figure 89.

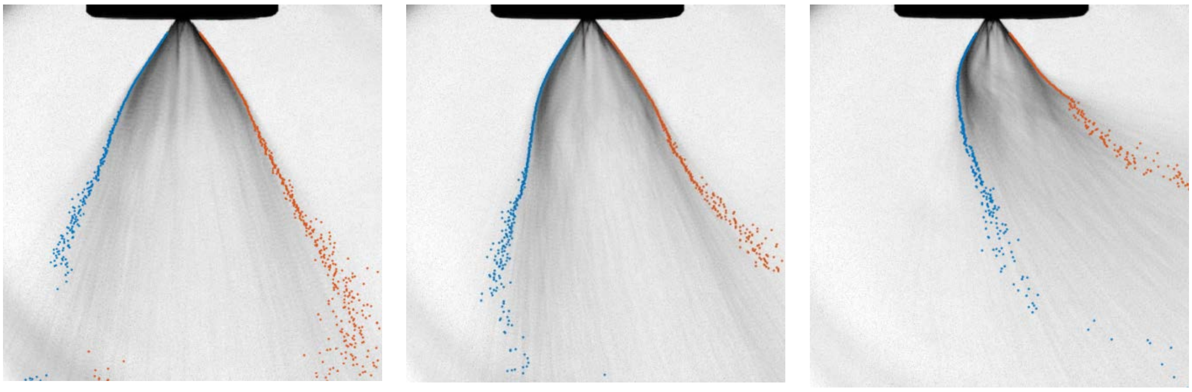

0.0 m/s 9.5 m/s 20.2 m/s

Figure 89 *Spray contour in cross-flow*

The results from high–speed illumination were presented. Further investigation of sprays in cross-flow is needed. A droplet size distribution and velocities of the droplets are measured by the PDA measurement system. The PDA data are not a part of this master thesis.

8 SUMMARY

In the first part of this master thesis, the wind tunnels are introduced and a suitable wind tunnel design for spray investigation is chosen. The most suitable tunnel for spray research is a blowdown wind tunnel. Essential parts of the tunnel are described, and design criteria are outlined. In the second chapter, the measurement techniques are discussed. All the described techniques belong to optical measurement techniques (PDA, PIV and high–speed visualization). Some requirements imposed by these techniques on the wind tunnel design are described (chapter 2.2.1 and 2.2.2). Different atomizers are listed in the chapter 3 and pressure swirl atomizers are described. The basic processes of atomization of the liquid sheet are outlined. Spray characteristics are listed and the influence of different variables on the spray characteristic is presented. At the end of chapter 3, sprays in cross-flow are described and a literature review is carried out. In chapter 4, a design procedure of low speed, small-scale wind tunnel for spray investigation is documented. This chapter deals with a design of crucial wind tunnel parts allowing to investigate the sprays (droplet separator, fuel circuit, traverse system) by optical measurement techniques (test section, compensator, supporting system). A flow quality in the test section is estimated and some design changes are made to ensure the good flow quality (uniform velocity profile with low turbulent intensity). Many experiments were carried out to ensure the influence of different parts of the wind tunnel on the flow quality. These experiments are described in chapter 5 (5.2, 5.3 and 5.4). In 5.5, an attempt was made to control the turbulence intensity in the test section. Different grids were used to control turbulence. The turbulent intensity and length scales are described in this chapter. In chapter 7, the experiment with spray in cross-flow is illustrated using high–speed visualization. Spray characteristics, such as spray cone angle, breakup length, penetration, and shape of the spray, can be recognized. Axial and radial velocities can be derived from instantaneous images. The influence of cross-flow on spray cone angle, breakup length, and spray shape are discussed.

Practical experience from the wind tunnel operation are now briefly described. Optical measurement methods (PDA) require a proper adjustment to obtain high measurement accuracy. The transmitting optics is set perpendicular to the wind tunnel test section. The position of receiving optics has no substantial influence on measurement accuracy. Prior to every spray measurement, the measurement system should be adjusted and checked to minimize the measurement errors. The acceleration of the step motors, used in traverse and supporting systems, should be checked and a low value should be set. Every part of the wind tunnel should be precisely mounted to the other parts. Misalignments can degrade the flow conditions in the test section of the wind tunnel. The velocity profile and turbulent intensity should be checked if some design changes were made in the wind tunnel construction. Design changes modify the pressure drop of the wind tunnel, and different velocities can be present in the test section. When using the oil mist for flow visualization, on the suction side of the driving fan, the oil can adhere to rotor blades. It is convenient to clean the rotor blades before measurement with CTA measurement system.

9 BIBLIOGRAPHY

[1] BARLOW, J., RAE, W., and POPE, A., 1999. *LOW-SPEED WIND TUNNEL TESTING: THIRD EDITION*. THIRD EDITION. New York: John Wiley & Sons. ISBN 0-471-55774-9.

[2] WEERASURIAY, A., TSE, T., ZHANG, X., and LI S., 2018. A wind tunnel study of effects of twisted wind flows on the pedestrian-level wind field in an urban environment. *Building and Environment*. **128**, 225-235.

[3] BEARD, K., and PRUPPACHER, H., 1969. A Determination of the Terminal Velocity and Drag of Small Water Drops by Means of a Wind Tunnel. *JOURNAL OF THE ATMOSPHERIC SCIENCES*. **26**, 1066-1072.

[4] VAZ, J., WOOD, D., BHATTACHARJEE, D., and LINS E., 2018. Drivetrain resistance and starting performance of a small wind turbine. *Renewable Energy*. **117**, 509-519.

[5] GEBBINK, R., WANG, G., and ZHONG, M., 2018. High-speed wind tunnel test of the CAE aerodynamic validation model. *Chinese Journal of Aeronautics*. **31**(3), 439-447.

[6] CARPENTIERY, M., CORTI, A., and ZIPOLI, L., 2004. Wind tunnel experiments of tracer dispersion downwind from a small-scale physical model of a landfill. *Environmental Modelling & Software*. **19**(10), 881-885.

[7] DAMAK, A., DRISS, Z., and ABID, M., 2018. Optimization of the helical Savonius rotor through wind tunnel experiments. *Journal of Wind Engineering and Industrial Aerodynamics*. **174**, 80-93.

[8] KALMBACH, A., and BREUER, M., 2013. Experimental PIV/V3V measurements of vortex-induced fluid–structure interaction in turbulent flow—A new benchmark FSI-PfS-2a. *Journal of Fluids and Structures*. **42**, 369-387.

[9] WEGENER, P., and ASHKENAS, h., 1961. Wind tunnel measurements of sphere drag at supersonic speeds and low Reynolds numbers. *Journal of Fluid Mechanics*. **10**(4), 550-560.

[10] PRAKASH, G., AKHILESH, D., MITRA, P., and ROUT, a. k., 2014. Experimental study of Aero Foil with Wind Tunnel Setup. *Recent Advances In Thermal Engineering (RATE-2014)*. **OSC-366/**, 1-10.

[11] ARIFUZZAMAN, M., and MASHUD, M., 2012. Design Construction and Performance Test of a Low Cost Subsonic Wind Tunnel. *IOSR Journal of Engineering*. **2**, 83-92.

[12] LIU, P., XING, Y., GUO, H., and LI, L., 2017. Design and performance of a small-scale aeroacoustic wind tunnel. *Applied Acoustics*. **116**, 65-69.

[13] CONTRACTION DESIGN FOR SMALL LOW-SPEED WIND TUNNELS, 1988. *JOINT INSTITUYE FOR AERONAUTICS AND ACOUSTICS* [online]. Stanford University Department of Aeronautics and Astronautics [cit. 2020-04-

04]. Dostupné z: https://ntrs.nasa.gov/archive/nasa/casi.ntrs.nasa.gov/19880012661.pdf

[14] FANG, F., CHEN, Ch., and HONG, Y., Experimental and analytical evaluation of flow in a square-to-square wind tunnel contraction. *Journal of Wind Engineering and Industrial Aerodynamics*. **89**(3-4), 247-262.

[15] BRADSHAW, P., 1965. The effect of wind-tunnel screens on nominally two-dimensional boundary layers. *Journal of Fluid Mechanics*. **22**(4), 679-687.

[16] KULKARNI, V., SAHOO, N., and CHAVAN, S., 2011. Simulation of honeycomb–screen combinations for turbulence management in a subsonic wind tunnel. *Journal of Wind Engineering and Industrial Aerodynamics*. **99**(1), 37-45.

[17] SUNNY, K., NALLAPANENI, A., KUMAR, M., MONA, H., and RAI, R., 2017. Development and Performance Investigation of Supersonic Blow-down Wind Tunnel. *International Journal of Earth Sciences and Engineering*. **10**, 18-23.

[18] HOGHOOGHI, H., AHMADABADI, M. N., and MANSHADI, M. D., 2016. Optimization of a subsonic wind tunnel nozzle with low contraction ratio via ball-spine inverse design method. *Journal of Mechanical Science and Technology*. **30**(5), 2059–2067.

[19] GUO, M., 2015. *Characterization of Fuel Spray Injected by Hole-Type Nozzle into Cross-Flow Ambient*. Hiroshima. Dissertation. Hiroshima University.

[20] Design Methodology for a Quick and Low-Cost Wind Tunnel, 2013. *IntechOpen* [online]. London: IntechOpen [cit. 2020-03-16]. Dostupné z: https://www.intechopen.com/books/wind-tunnel-designs-and-their-diverse-engineering-applications/design-methodology-for-a-quick-and-low-cost-wind-tunnel

[21] SCHEIMAN, J., and BROOKS, J. D., 1981. Comparison of Experimental and Theoretical Turbulence Reduction from Screens, Honeycomb, and Honeycomb-Screen Combinations. *Journal of Aircraft*. **18**(8), 638-643.

[22] MAURO, S., LANZAFAME, R., MESSINA, M., BRUSCA, S., FAMOSO, F., and GALVAGNO, A., 2017. Small-Scale Open-Circuit Wind Tunnel: Design Criteria, Construction and Calibration. *International Journal of Applied Engineering Research*. **12**(23), 13649-13662.

[23] MEHTA, R.D., and PBRADSHAW, P., 1979. Design rules for small low speed wind tunnels. *The Aeronautical Journal*. **83**(827), 443-453.

[24] DRYDEN, H. L., and SCHUBAUER, G. B., 1947. The Use of Damping Screens for the Reduction of Wind-Tunnel Turbulence. *Journal of the Aeronautical Sciences*. **14**(4), 221-228.

[25] GROTH, J., and JOHANSSON, A. V., 1988. Turbulence reduction by screens. *Journal of Fluid Mechanics*. **197**, 139-155.

[26] YEH, Y., and CUMMINS, H. Z., 1964. LOCALIZED FLUID FLOW MEASUREMENTS WITH AN HeNe LASER SPECTROMETER. *APPLIED PHYSICS LETTERS*. **4**(10), 176-178.

[27] BOUTIER, A., *Laser Velocimetry in Fluid Mechanics,* 2012. USA: John Wiley. ISBN 978-1-84821-397-5.

[28] LDA and PDA Reference Manual. Dantec Dynamics, 1st edition, 2011.

[29] ĎURDINA, L. Measurement of Spray Characteristics Using Optical Measurement Methods. Brno: Vysoké učení technické v Brně, Fakulta strojního inženýrství, 2012. 81 s. Vedoucí diplomové práce Ing. Jan Jedelský, Ph.D.

[30] ZHANG, Z., *LDA Application Methods*, 2010. New York: Springer Heidelberg Dordrecht London New York. ISBN 978-3-642-13513-2.

[31] HIRLEMAN, D., 1996. History of Development of the Velocimeter. *Particle & Particle Systems Characterization*. **13**, 59-67.

[32] Principles of Phase Doppler Anemometry. Available from: http://www. dantecdynamics.com/Admin/Public/DWSDownload.aspx?File=Files%2fFiler % 2fsupport_and_download%2fresearch_and_education%2fpda.zip.

[33] ADRIAN, R., WESTERWEEL, J., *PARTICLE IMAGE VELOCIMETRY*, 2011. New York: Cambridge University Press. ISBN 978-0-521-44008-0 Hardback.

[34] CEJPEK, O., MALÝ, M., KOCHED, A., SAPÍK, M., LÍZAL, F., and JEDELSKÝ, J., 2019. Suitability of Volumetric 3-Component Velocimetry Method for Measurement of Pressure Swirl Sprays. In: *Topical Problems of Fluid Mechanics 2019*. Praque: Topical Problems of Fluid Mechanics. ISBN 978-80-87012-69-7. ISSN 2336-5781.

[35] Calibration Plates, 2020. *LaVision* [online]. USA: LaVision [cit. 2020-02-10]. Dostupné z: https://www.smart-piv.com/en/products/strainmaster/system-components/calibration-plates/

[36] High-Speed Photography, 2017. *Atomicheritage* [online]. New Mexico: Atomic Heritage Foundation [cit. 2020-02-10]. Dostupné z: https://www.atomicheritage.org/history/high-speed-photography

[37] VERSLUIS, M., 2013. High-speed imaging in fluids. *Experiments in Fluids*. **54**, 1458-1493.

[38] AUCH, M., 2013. Measurements of Three-Dimensional Velocity Fields Under Breaking Waves. *The Journal of Undergraduate Research*. **11**(3), 13-22.

[39] FASTCAM SA-Z – Redefining High Speed Imaging Performance, 2013. In: *Photron* [online]. San Diego: Photron USA [cit. 2020-02-10]. Dostupné z: https://photron.com/fastcam-sa-z-redefining-high-speed-imaging-performance/

[40] BAYVEL, L., ORZECHOVSKY, Z., *Liquid Atomization*, 1993. Washington: Taylor & Francis. ISBN 0-89116-959-8

[41] LEFEBVRE, A. H., 2017. *Atomization and Sprays*. Second edition. USA: CRC Press. ISBN 9781498736268.

[42] LEE, E. J., OH, S. Y., KIM, H. Y., JAMES S., and YOON, S., 2010. Measuring air core characteristics of a pressure-swirl atomizer via a transparent acrylic nozzle at various Reynolds numbers. *Experimental Thermal and Fluid Science*. **34**(8), 1475-1483.

[43] Square spray pattern SSXP series nozzles, 2020. In: *IKEUCHI USA* [online]. USA: IKEUCHI USA [cit. 2020-02-10]. Dostupné z: https://www.ikeuchi.us/eng/products/spray/1ryutai/311.

[44] MALÝ, M., JEDELSKÝ, J., SLÁMA, J., JANÁČKOVÁ, L., SAPÍK, M., WIGLEY, G., and JÍCHA, M., 2017. Internal flow and air core dynamics in simplex and spill-return pressure-swirl atomizers. *ILASS2017 - 28th European Conference on Liquid Atomization and Spray Systems*.

[45] TATE, R. W., Sprays, Kirk-Othmer Encyclopedia of Chemical Technology, Vol. 18, 2nd ed., New York: John Wiley & Sons, 1969, pp. 634–654.

[46] Flat fan nozzle, 2020. In: *Wikimedia Commons* [online]. Wikimedia Commons [cit. 2020-02-14]. Dostupné z: https://commons.wikimedia.org/wiki/File:Flat_fan_nozzle.png

[47] SIRIGNANO, W., and MEHRING, C., 2000. Review of theory of distortion and disintegration of liquid streams. *Progress in Energy and Combustion Science*. **26**(4-6), 609-655.

[48] ETTENENI, N. K., and AVULAPATI, M. M., 2019. Dynamics of liquid sheet breakup due to perforations in impingement atomization. *ILASS–Europe 2019,*. 1-8.

[49] BOSSARD, J. A. and Robert PECK, 1996. Droplet size distribution effects in spray combustion. *Symposium (International) on Combustion*. **26**(1), 1671-1677.

[50] WANG, X. F. and LEFEBVRE, A. H., Paper Presented at the 32nd ASME International Gas Turbine Conference, Anaheim, California, June 1987

[51] RIZK, N. K., and LEFEBVRE, A. H., Spray characteristics of spill-return atomizer, AIAA J. Propul. Power, Vol. 1, No. 3, 1985, pp. 200–204

[52] JEDELSKÝ, J., MALÝ, M., CORRAL, N. P., WIGLEY, G., JANÁČKOVÁ, L., and JÍCHA, M., 2018. Air–liquid interactions in a pressure-swirl spray. *International Journal of Heat and Mass Transfer*. **121**, 788-804.

[53] MALÝ, M. Kvalita rozprašování paliv u malých tlakových vířivých trysek. Brno: Vysoké učení technické v Brně, Fakulta strojního inženýrství, 2014. 52 s. Vedoucí bakalářské práce doc. Ing. Jan Jedelský, Ph.D.

[54] DIKSHIT, S., KULSHRESHTA, D., and CHANNIWALA, S.A., 2018. Factors Affecting Spray Cone Angle of Pressure Swirl Atomizer for Gas Turbine

Combustion Chamber: Theoretical and Experimental Analysis. *Indian Journal of Science and Technology*. **11**(8).

[55] AALBURG, Ch., LEER, B., FAETH, G. M., and SALLAM, K., 2004. Properties of Nonturbulent Round Liquid Jets in Uniform Crossflows. *42nd AIAA Aerospace Sciences Meeting and Exhibit*.

[56] BAI, B. F., ZHANG, H., LIU, L., and SUN, H. J., 2009. Experimental study on turbulent mixing of spray droplets in crossflow. *Experimental Thermal and Fluid Science*. **33**(6), 1012-1020.

[57] LEE, J., SALLAM, K. A., LIN, K.-C., and CARTER, C. D., 2009. Spray Structure in Near-Injector Region of Aerated Jet in Subsonic Crossflow. *Journal of Propulsion and Power*. **25**(2), 258-266.

[58] BEHZAD, M., ASHGRIZ, N., and KARNEY, B. W., 2016. Surface breakup of a non-turbulent liquid jet injected into a high pressure gaseous crossflow. *International Journal of Multiphase Flow*. **80**, 100-117.

[59] WU, P. K., KIRKENDALL, K. A., FULLER, R. P., and NEJAD, A. S., 1997. Breakup Processes of Liquid Jets in Subsonic Cross flows. *Journal of Propulsion and Power*. **13**(1), 64-73.

[60] BUNCE, K., LEE, J., and SANTAVICCA, D., 2006. Characterization of Liquid Jets-In-Crossflow Under High Temperature, High Velocity Non-Oscillating and Oscillating Flow Conditions. *Collection of Technical Papers - 44th AIAA Aerospace Sciences Meeting*. **20**(10).

[61] ESLAMIAN, M., AMIGHI, A., and ASHGRIZ, N., 2014. Atomization of Liquid Jet in High-Pressure and High-Temperature Subsonic Crossflow PT - Journal Article. *AIAA Journal*. **52**(7), 1374-1385.

[62] GUO, M., NISHIDA, K., OGATA, Y., MARSHALL, Ch., and FAN, Q., 2016. Experimental study on fuel spray characteristics under atmospheric and pressurized cross-flow conditions. *FUEL*. **184**, 846-855.

[63] COSTA, M., MELO, M. J., SOUSA, J. M. M. and LEVY, Y. 2006. Spray Characteristics of Angled Liquid Injection into Subsonic Crossflows. *AIAA Journal*. **44**(3), 646-653.

[64] BEHZAD, M. and ASHGRIZ, N., 2012. An Analysis of the Surface Breakup Mechanism of a Liquid Jet in Cross-flow. *ICLASS 2012, 12th Triennial International Conference on Liquid Atomization and Spray Systems*. 1-8.

[65] LI, P., WANG, Z., SUN, M. B., and WANG, H., 2016. Numerical simulation of the gas-liquid interaction of a liquid jet in supersonic crossflow. *Acta Astronautica*. **134**.

[66] PRAKASH, S., GADGIL, H. P., and RAGHU, B. N., 2014. Breakup processes of pressure swirl spray in gaseous cross-flow. *International Journal of Multiphase Flow*. **66**, 79-91.

[67] LEE, S., WONHO, K., and YOON, W., 2010. Spray formation by a swirl spray jet in low speed cross-flow. *J Mech Sci Technol*. **24**, 559–568.

[68] RACHNER, M., BECKER, J., HASSA, Ch., and DOERR, T., 2002. Modelling of the atomization of a plain liquid fuel jet in crossflow at gas turbine conditions. *Aerospace Science and Technology*. **6**(7), 495-506.

[69] ZHANG, H., BAI, B. F., LIU, L., SUN, H., and YAN, J., 2013. Droplet dispersion characteristics of the hollow cone sprays in crossflow. *Experimental Thermal and Fluid Science*. **45**, 25-33.

[70] MEHTA, R.D., and BREDSHAW, P., 1979. Design rules for small low speed wind tunnels. *The Aeronautical Journal*. **83**(827), 443-453.

[71] BRADSHAW, P., and PANKHURST, R. C., 1964. The design of low-speed wind tunnels. *Progress in Aerospace Sciences*. **5**, 1-69.

[72] RFC a RFE radiální ventilátory s přímým pohonem, 2008. *Alteko* [online]. Czech Republic: Alteko [cit. 2020-03-16]. Dostupné z: http://www.alteko.cz/upl/download/100003s_TD_10.8_Cz_RFC-RFE.pdf

[73] KUDO, T., KOMATSU, Y., MAEDA, K., and NISHIMURA, M., 2009. Techniques for Reducing Low-Frequency Fluctuations in Aeroacoustic Wind Tunnels. *Journal of Environment and Engineering*. **4**(2), 289-301.

[74] BREIDERHOFF, B., BARTZ, B. T., NAUJOKS, B., et al., 2013. Simulation and Optimization of Cyclone Dust Separators. *Proceedings 23. Workshop Computational Intelligence*. 177-197.

[75] Cyclone separator, 2019. *ENERGY EDUCATION* [online]. Calgary: University of Calgary [cit. 2020-03-16]. Dostupné z: https://energyeducation.ca/encyclopedia/Cyclone_separator#cite_note-1

[76] GAS/LIQUID SEPARATORS - TYPE SELECTION AND DESIGN RULES, 2007. *DESIGN AND ENGINEERING PRACTICE* [online]. [cit. 2020-04-04]. Dostupné z: https://www.academia.edu/34740393/LIQUID_LIQUID_AND_GAS_LIQUID_LIQUID_THREE-PHASE_SEPARATORS_-TYPE_SELECTION_AND_DESIGN_RULES

[77] Guilherme Augusto D. da Silva, Wind Tunnel Vibration Measurements

[78] KURIAN, T., and FRANSSON, J. H. M, 2009. Grid-generated turbulence revisited. *Fluid Dynamics Research*. **41**(2).

[79] HIDEHARU, M., 1991. Realization of a large-scale turbulence field in a small wind tunnel. *Fluid Dynamics Research*. **8**(1-4), 53-64.

[80] TORRES, A., TAPIA, R., and RAMOS, A., 2016. Generation and Control of Turbulences in a Wind Tunnel. *Open Journal of Fluid Dynamics*. **6**, 453-471.

[81] KRÖGER, L., FREDERIK, J., WINGERDEN, J. W., PEINKE, J., and HÖLLING, M., 2018. Generation of user defined turbulent inflow conditions by

an active grid for validation experiments. *Journal of Physics Conference Series*. **1037**.

[82] LAWS, E. M., and LIVESEY, J. L., 1978. Flow Through Screens. *Annual Review of Fluid Mechanics*. **10**(1), 247-266.

[83] EL-GABRY, THURMAN, L.A., THURMAN, D. R., and POINSATTE, P. E., *Procedure for Determining Turbulence Length Scales Using Hotwire Anemometry*.

[84] URUBA, V., Turbulence, ČVUT Praha, Počet stran: 130, 2., přeprac. vyd., ISBN: 978-80-0105-600-4, EAN: 9788001056004, 2014.

[85] Aerodynamický tunel, 2020. In: *PŘÍSTROJOVÉ VYBAVENÍ* [online]. Brno: VYSOKÉ UČENÍ TECHNICKÉ V BRNĚ [cit. 2020-05-27]. Dostupné z: https://eu.fme.vutbr.cz/o-nas-laboratore-ottp-pristrojove-vybaveni#21

LIST OF SYMBOLS

Roman symbols

c	Speed of light	[m/s]
D	Characteristic dimension	[m]
D_f	Beam waist diameter	[m]
d_h	Hydraulic diameter	[m]
D_i	Droplet diameter	[m]
d_x	Height of measurement volume	[m]
d_y	Width of measurement volume	[m]
d_z	Length of measurement volume	[m]
e_i	Unite vector of incoming light	[–]
e_s	Unite vector of scattered light	[–]
e_1	Unite vector of incoming light (laser beam 1)	[–]
e_2	Unite vector of incoming light (laser beam 2)	[–]
f	Required frame rate	[fps]
f_D	Doppler-frequency	[Hz]
f_f	Frequency of fan	[Hz]
f_i	Frequency of incoming light	[Hz]
f_s	Frequency of scattered light	[Hz]
$f_{s,1}$	Frequency of scattered light (laser beam 1)	[Hz]
$f_{s,2}$	Frequency of scattered light (laser beam 2)	[Hz]
f_v	Frequency of vanes	[Hz]
f_1	Frequency of incoming light (laser beam 1)	[Hz]
f_2	Frequency of incoming light (laser beam 2)	[Hz]
H	Height of inlet duct	[m]
K	Contraction ratio	[–]
K_s	Pressure loss coefficient	[–]
l	Typical length scale	[m]
L	Length of pipe	[m]
L_b	Length of cyclone body	[m]
L_c	Length of cyclone cone	[m]
$\dot{m}_{liquid}$	Mass flow rate of liquid	[kg/s]
$\dot{m}_{air}$	Mass flow rate of ambient air	[kg/s]
N	Number of samples	[–]
n_i	Number of droplets	[–]
n_v	Number of vanes	[–]
RPM_{fan}	Revolutions per minute of fan	[1/min]
S	Test section cross section	[m^2]
S_{all}	Flow cross section	[m^2]
S_{free}	Free flow cross section	[m^2]
S_{in}	Input cross-section of nozzle	[m^2]
S_{out}	Output cross-section of nozzle	[m^2]
Tu	Turbulent intensity	[%]
U	Velocity vector of particle	[m/s]
u	Velocity of event	[m/s]
u_{mean}	Mean velocity	[m/s]
u_{rms}	Root mean square of velocity	[m/s]
u_x	Particle velocity perpendicular to measurement volume	[m/s]
$\dot{V}$	Volume flux	[m^3/s]

V_i	Inlet gas velocity	[m/s]
v	Fluid flow velocity	[m/s]
v_{air}	Velocity of ambient air	[m/s]
v_{liquid}	Velocity of liquid sheet close to the nozzle	[m/s]
W	Width of inlet	[m]

Greek symbols

Δt	Time lag between signals	[s]
$\Delta\Phi_{12}$	Phase shift	[–]
δ_f	Distance between fringes	[m]
ζ_m	Local pressure loss coefficient	[–]
θ	Angle between two incident light beams	[°]
λ	Wavelength of light	[m/s]
λ_f	Friction coefficient	
λ_i	Wavelength of incoming light	[m]
μ	Gas viscosity	[kg/ms]
μ_l	Kinematic viscosity of liquid	[m/s^2]
ρ	Density of fluid flow	[kg/m^3]
ρ_{air}	Density of air	[kg/m^3]
ρ_l	Density of liquid	[kg/m^3]
ρ_p	Density of particle in the flow	[kg/m^3]
σ_l	Surface tension of liquid	[N/m]

LIST OF ATTACHMENTS

A. Conference paper at EFM 2019

Reference:

CEJPEK, O.; ŠÍP, J.; MALÝ, M.; JEDELSKÝ, J.; TOMÁŠ, Z. Analysis of velocity profile measurements obtained by different methods in low-speed, small-scale wind tunnel. 2020. s. 72-79.

Drawing documentation

WIND_TUNNEL

WIND_TUNNEL_BOM

DROPLET_SEPARATOR

DROPLET_SEPARATOR_BOM

EXIT_DIFUSER

EXIT_DIFUSER_BOM

INLET_DIFUSER

INLET_DIFUSER_BOM

KONFUSER

KONFUSER_BOM

LAM_SECTION

SETLING_CHAMBER

TEST_SECTION

TEST_SECTION_BOM

FAN_SUPPORT

FAN_SUPPORT_BOM

TUNNEL_SUPPORT

TUNNEL_SUPPORT_BOM

Analysis of velocity profile measurements obtained by different methods in low-speed, small-scale wind tunnel

Ondřej Cejpek[1,*], *Jan* Šíp[1], *Milan* Malý[1], *Jan* Jedelský[1], and *Zdeněk* Tomáš[2]

[1]Energy Institute, Faculty of Mechanical Engineering, Brno University of Technology, Technická 2896/2, 616 69 Brno, Czech Republic
[2]Provyko s.r.o., Vinařská 558/3a, Pisárky, 603 00 Brno, Czech Republic

Abstract. A low-speed small-scale wind tunnel was designed for spray investigation under cross and co-flow conditions. Precisely defined profiles of mean velocity and turbulent intensity in the wind tunnel test section are crucial parameters for any rigorous flow study. Different velocity measurement techniques were used to evaluate the velocity and turbulent intensity profiles in the test section. Two non-intrusive techniques, Phase-Doppler Anemometry and Laser-Doppler Anemometry (PDA, LDA), and two intrusive techniques, Constant Temperature Anemometry (CTA) and pitot static tubes of S and L-type were applied. The velocity was measured in 19 equidistantly spaced positions in a centrally placed horizontal plane. The data were obtained for four different mean velocities in the test section (7, 14, 21, 28 m/s). Results of different measurement techniques were mutually compared, and repeatabilities and uncertainties of PDA and CTA measurements were assessed. Turbulent velocity spectra measured by the CTA were analysed. The effect of declination of the pitot static tubes (L-type and S-type) was briefly discussed and compared with an industrial velocity probe QuadraTherm® 640i In-Line Mass Flow Meter with a measuring range of 5–300 m/s. Velocity and declination of pitot static tubes were analysed only in the central point of the test section. The results show that a fully turbulent and uniform flow is developed 15 mm upstream the test section area. Mean velocity and turbulent intensity profiles obtained by different techniques are in a good agreement. Uncertainties of type B of PDA and CTA measurement method are below 5%. Turbulent intensity in the main stream is under 5%. Advantages and drawbacks of the presented measurement techniques were discussed. The PDA was found to be the most suitable measurement technique due to its precision and non–intrusive flow probing.

1 INTRODUCTION

Wind tunnels have been used for more than a century. Their size can range from several meters to more than ten meters. Two designs of a wind tunnels used are closed and open loop wind tunnels [1, 2]. The wind tunnels can be also divided according to the velocity in the test section into four groups to subsonic, transonic, supersonic, and hypersonic wind tunnels [3, 4, 5]. Each wind tunnel design is suitable for different types of experiments and required flow characteristics in the test section. Wind tunnels can simulate velocity conditions in combustion chambers, turbines, conditions in the atmosphere and in many other situations related to air movement and air-structure interaction.

Precisely defined velocity profiles and controllable and sufficiently low turbulent intensity in the test section of the wind tunnel are crucial parameters for any rigorous flow study. A new small-scale low-speed wind tunnel was built at Energy Institute, Faculty of Mechanical Engineering, Brno University of Technology, Spray laboratory.

Together with Phase-Doppler Anemometry (PDA), Laser-Doppler Anemometry (LDA), Constant Temperature Anemometry (CTA) and other velocity measurement techniques, wind tunnels create a tool for investigation of high complex, spatially and temporally unstable flows, i.e. flow around the turbine blades, velocity profile around a car, investigation of fluid structure interaction, and spray flows in cross and co-flow.

Laser-Doppler Velocimetry (LDV) or Laser-Doppler Anemometry (LDA) were first implemented and described in 1964 [6]. After this publication, various systems of LDV were proposed. Over a decade, new systems were probed, and improvements of the system were made. The first commercial system was available in 1970. Because of a wide field of application of LDV, many set-ups of the system arise during the LDV commercial use [7].

The PDA measurement system is an extension of LDA concept used for velocity measurement. A need to measure the velocity and the size of the particles in investigated flows simultaneously resulted in the development of PDA measurement system. PDA is a very

---

[*] Corresponding author: 182752@vutbr.cz

complex system, hence the process of invention, development, and acceptance of laser–based system took a long time. Crucial was the invention of laser in the 1960s, a measurement concept in 1975, and extensive work done by many research groups during 1980s. [8]. The PDA measurement system was not fully accepted at the early stage; the results were verified by other well-known measurement techniques to prove the PDA system accuracy and measurement abilities. After almost 30 years of application of PDA, this measurement technique becomes a standard for the experimental fluid flow studies, and a major part of the flow research is done by the PDA system. Nowadays, PDA is used to validate newly designed techniques, i.e. Particle Image Velocimetry (PIV) [9]. PDA can be also used to validate volumetric measurement methods.

LDA and PDA are optical-based non-intrusive measurement techniques. These techniques identify velocities of the seeding particles introduced into the flow, based on the scattered light by the particles. These techniques can provide results with high spatial and temporal resolution and with high accuracy. LDA measures the velocity of the tracer particles; in addition, PDA is capable of measuring the particle/droplet diameter. The inspected flow had to be seeded with particles which will scatter sufficient light and will follow the flow with high accuracy to identify the finest vortices in the flow. An optical access to the flow is also required [10]. The PDA and LDA system responses are a liner function of the fluid flow velocity in contrast with CTA which is sensitive to the ambient temperature.

Two used intrusive techniques are pitot static tube and CTA. The pitot static tube is a well-known measurement device which has been used in industry for more than two centuries. A simple and robust design, function principle, and accurate results ensure the pitot static tube a wide range of applications in industry (racing cars, aircraft speed measurement, measurement of the flow velocity in duct or pipes, laboratory use). The pitot static tube was initially used only in laboratory for more than a century. After the improvements by Henry P.G. Darcy, the pitot static tube started to be used in industry. [11]

CTA is a measurement technique based on a principle of hot-wire anemometry, where the constant temperature of the measurement element is maintained. A cooling effect of the flow is compensated by the Wheatstone bridge, and the temperature of the element is kept constant. The voltage drop across the circuit is proportional to the inspected fluid flow velocity. The CTA system needs to be calibrated prior to every measurement. CTA is a very useful tool for measurement of the turbulent flow because this system has a very high response to the fluid flow change and can capture the finest vortices in the flow. The probe is usually a thin wire with a diameter of several micrometres; therefore, it has a low thermal inertia.

A fundamental principle of CTA was discovered in 1888, when the relation between the convection and the fluid velocity was experimentally derived. In 1907, cooling of a thin wire in the air stream was observed, and the first suggestion for measuring of the fluid flow velocity appeared. Experimental work continued for the next 30 years; during this period, 2D and 3D probes were designed, and two main principles of hot-wire anemometry emerged (CCA, CTA). Many other improvements of the CTA system arose during this period [12]. Further work was devoted mainly to maximisation of the response of the electrical circuit in the CTA measurement system [13]. The first CTA system was commercially available in 1950s.

1 EXPERIMENTAL SETUP

Experiments were performed at Spray Laboratory, Faculty of Mechanical Engineering, Brno University of Technology. Mean velocity profiles and turbulent intensities were measured in a newly designed small-scale low-speed wind tunnel test section with cross-section of 200×200 mm. The measurement of mean velocity flow was performed in one plane and in 19 equidistantly spaced positions. Figure 1 shows the schematic layout of the measurement points in the wind tunnel test section.

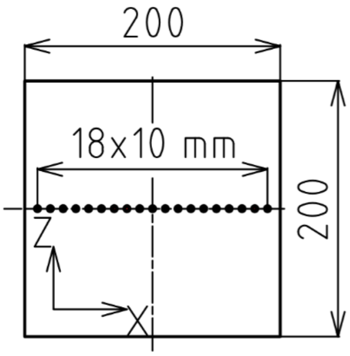

Fig. 1. Measurement points

1.1 PDA Experimental Setup

Particle sizes and velocities were probed by two-component Phase Doppler anemometer (PDA) Dantec Dynamics A/S, see a schematic layout in Figure 2. In each position, 5 kHz sampling frequency was used, and the measurement took 5 s in each point. Information about the PDA are outlined in Table 1.

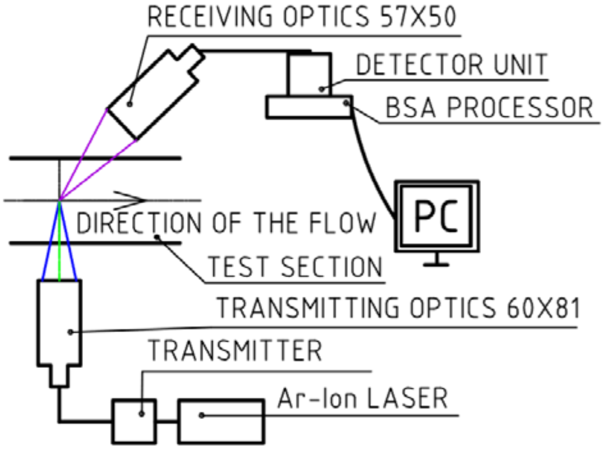

Fig. 2. PDA experimental setup

Table 1. PDA experimental setup

Parameter	Value
Laser power output	1 W
Wavelength	514.5 nm
Focal length of transmitting optics	310 mm
Focal length of receiving optics	500 mm
Scattering angle	45 °
Mask	A
Spatial filter	0.1 mm
Sensitivity	1100 V
SNR	0 dB
Signal gain	20 dB
Level validation ratio	6

1.2 CTA Experimental Setup

A thermoanemometry method was applied (HWA), specifically the CTA measurement technique. StreamLine hot-wire anemometry from Dantec Dynamic was used. Velocity measurement was performed with the wired 1D 55R01 probe. The length of the wire was 3 mm, the measuring part of the wire was 1.25 mm long.

Calibration was performed prior to the measurement. The Dantec streamline Pro Automatic calibrator was used. The wire probe was calibrated in the velocity range of 1–45 m/s in fifteen points. A sampling frequency was set to 10 kHz, and the duration of the measurement was set to 5 s in each point.

The Linear traverse system (ISEL AUSTRIA GMBH & CO. KG) was used to traverse the probe. The span of 3 s was set before the measurement to suppress the vibration of the traverse. The CTA experimental setup is illustrated in Figure 3.

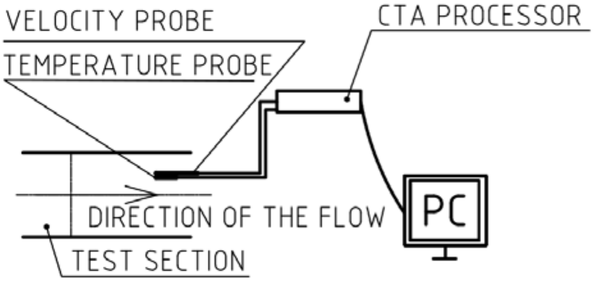

Fig. 3. CTA experimental setup

1.3 LDA Experimental Setup

FlowExplorer (Dantec Dynamics A/S, Skovlunde, DK) 1D LDA system with Diode Pumped Solid State (DPSS) laser was used. Wavelength of the laser was 660 nm. The system was working in backscatter mode; the receiver and the transmitter were placed in one body. The beam was split into two parallel beams with the power of 30 mW each. One of the beams was shifted by 80 MHz. A converging transmitting/receiving lens with the focal length of 300 mm was used. Dantec BSA P80 signal processor was used to process the measured signal. BSA flow software v5.20 was used to control the data acquisition. A schematic layout of the LDA measurement system is shown in Figure 4.

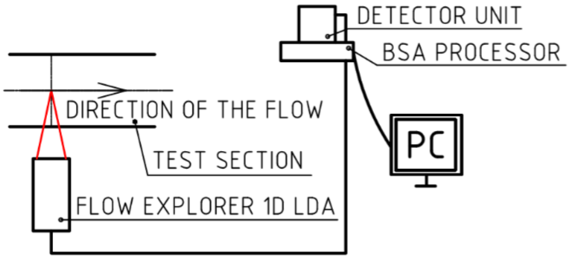

Fig. 4. LDA experimental setup

1.4 Seeding Particles

A fog generator was used to generate seeding particles. The particles with a diameter D [μm] in the range of 1-3.5 μm were applied on the suction side of the driving fan. The diameter of particles was measured by the PDA measurement system. The particles are small enough to follow the flow reasonably well; the particle Stokes number was below 0.1. A histogram of the particles diameter measured by the PDA is shown in Figure 5.

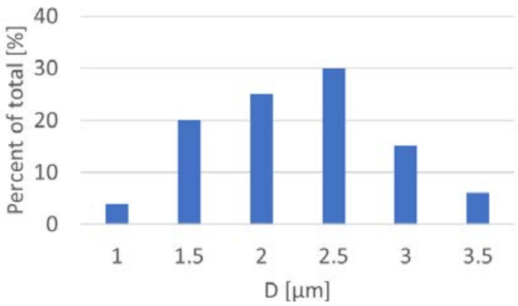

Fig. 5. Histogram of seeding particles diameter measured by PDA system

1.4 Experimental Setup of Pitot static tube

The L-type pitot static tube was used. The measuring device with accuracy of ±0.1% of measurement value was used. A pressure difference measurement range was 0–1000 Pa. The measurement system does not allow for PC connection or data export; the values were read on the device display. The measurement system can be seen in Figure 6.

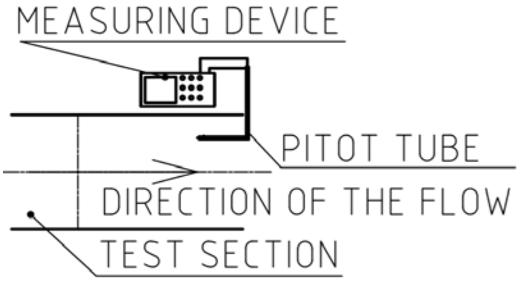

Fig. 6. Pitot static tube experimental setup

2 RESULTS AND DISCUSION

Important characteristics of every wind tunnel are the velocity profile and turbulent intensity in the tunnel test section. Uniform velocity profile and low turbulence are required in the test section of almost all kinds of wind tunnels. As was mentioned before, velocity and turbulent intensity measurement were performed by different measurement systems, which were described in the foregoing section.

2.1 Velocity Profiles

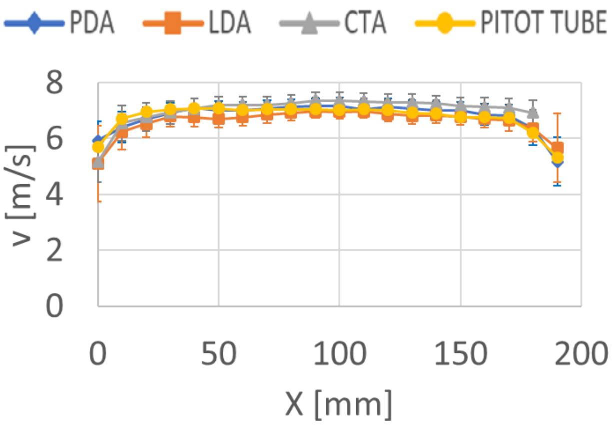

Fig 7. Velocity profile, mean velocity of 7 m/s

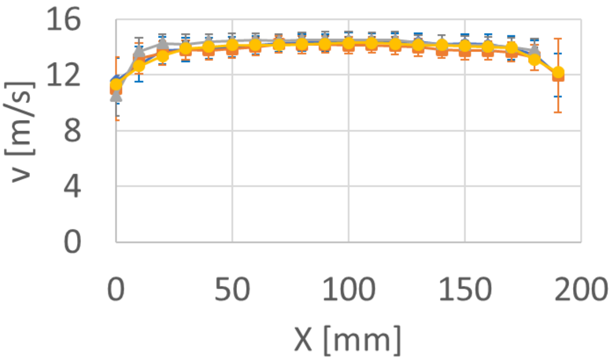

Fig 8. Velocity profile, mean velocity of 14 m/s

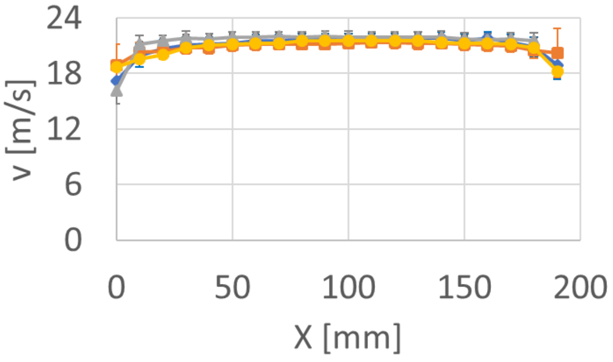

Fig. 9. Velocity profile, mean velocity of 21 m/s

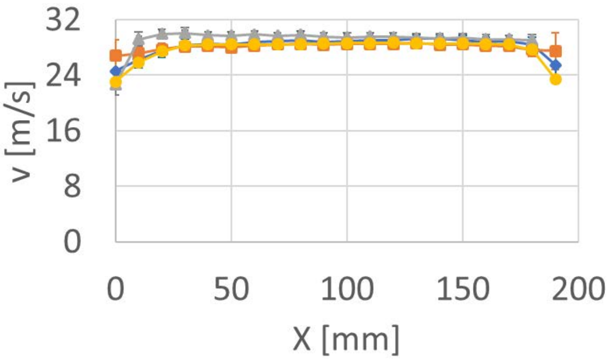

Fig. 10. Velocity profile, mean velocity of 28 m/s

Figures 7–10 show velocity profiles for different mean velocities in the test section and for different measurement systems. As seen in these images, the results obtained by different measurement methods are in a good agreement. Velocity profiles in Figures 7 to 10 are uniform across the cross-section of the test section. The thickness of boundary layer is defined as the distance from the wall, to the point, where the velocity magnitude reaches value of 99% of free stream velocity. A boundary layer thickness is represented in Table 2. In the boundary layer region, velocity decreases and the largest deviations between the measurement systems are observed.

Table 2. Boundary layer thickness

Mean velocity [m/s]	Free stream velocity [m/s]	Boundary layer thickness [mm]
7	7,02	15
14	14,31	18
21	21,42	20
28	28,2	23

2.2 Turbulent Intensity

The pitot static tube did not allow to measure the turbulent intensity; a comparison of turbulent intensity is performed only for the PDA, LDA and CTA measurement techniques. Turbulent intensity of four different regimes is illustrated in Figures 11–14. Turbulent intensity in the main flow reaches the values under 5%*. In the boundary layer, turbulent intensity is higher. It is caused by the spatial and temporal instabilities in the boundary layer near the surface. As seen in Figures 11–14, turbulent intensity is slightly different when measured by different techniques, which is most visible in Figure 14. The CTA measurement system measures a lower turbulent intensity than the LDA or PDA systems. According to [14], turbulent intensity measured by the PDA and LDA measurement systems will always be higher (broadening effect).

A lot of improvements of the flow quality can be obtained in the test section. Turbulent intensities in well-designed wind tunnels are under 0.1% [15]. At Tokohu University in Japan, a closed loop wind tunnel with 0.02% turbulent intensity in the free stream was designed [16]. Steps to reduce the turbulent intensity in the test section will be taken in the future.

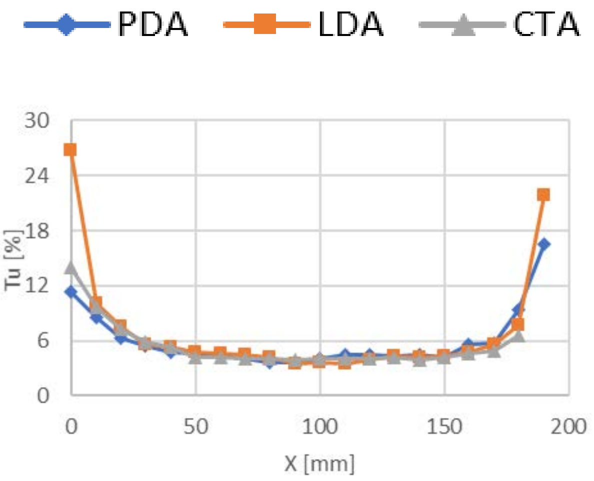

Fig 11. Turbulent intensity, mean velocity of 7 m/s

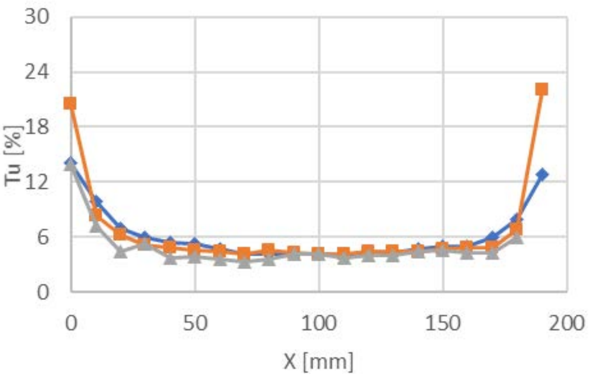

Fig. 12. Turbulent intensity, mean velocity of 14 m/s

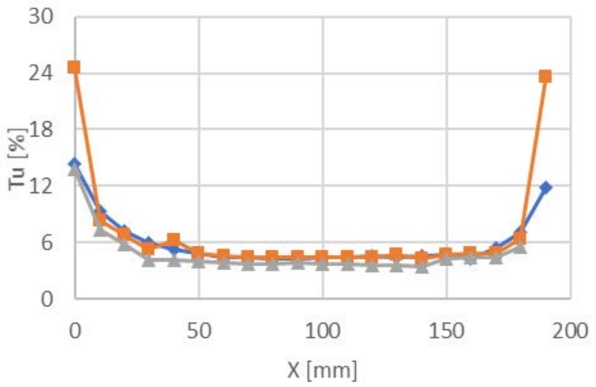

Fig. 13. Turbulent intensity, mean velocity of 21 m/s

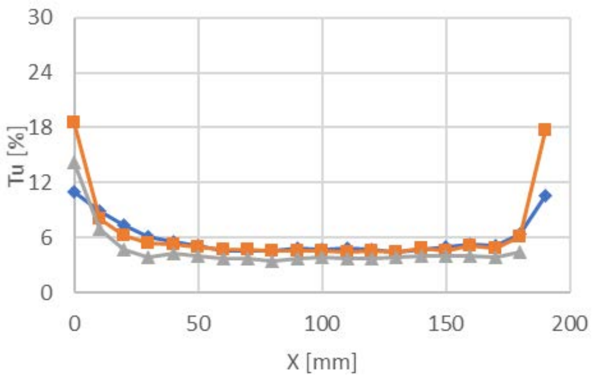

Fig. 14. Turbulent intensity, mean velocity of 28 m/s

2.3 PDA and CTA Repeatability and Uncertainties

Six measurements were made to determine the PDA and CTA measurement system repeatability. The attempt was made to assess systematic and random errors of measurement. Combined uncertainty for the PDA measurement system was determined according to [17] to be 1% of the measured value for the velocity measurement. Combined uncertainty of the CTA measurement was determined to be 3.5% of the measured value. Uncertainty was determined according to the procedure described in [18]. There are incorporated uncertainties of the calibration (2%), anemometers (0.2%), linearization (0.5%), resolution of A/D converter (0.02%), uncertainty of position of the probe (0.01%). Uncertainty of temperature change of hot wire, ambient temperature change, atmospheric pressure change and humidity of air change are low comparing to aforementioned uncertainty and are not incorporated. In Figures 15 and 16, the uncertainty for one regime of the velocity and turbulent intensity measurement can be seen (mean velocity of 21 m/s). According to the results shown in Figures 15 and 16, the PDA and CTA velocity, turbulent intensity results can be declared to be the same. The uncertainties are higher in the boundary layer region, where the flow has an unstable and unpredictable behaviour. Also, the uncertainties are lower for the PDA measurement system.

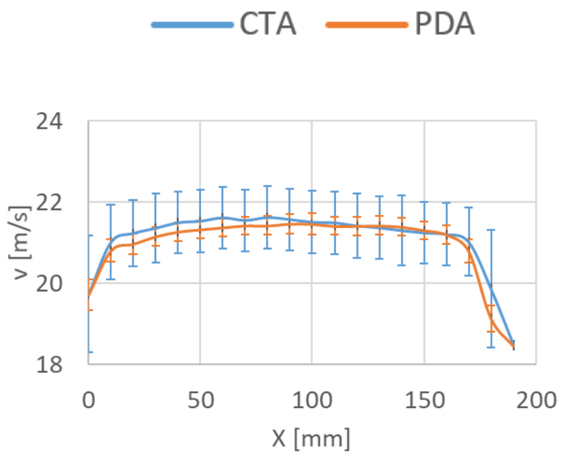

Fig. 15. Uncertainty of velocity measurement for PDA and CTA systems

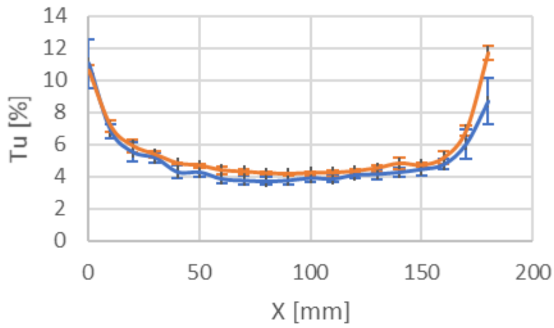

Fig. 16. Uncertainty of turbulent intensity measurement for PDA and CTA systems

2.4 Turbulent Spectra

Turbulent spectra for the CTA measurement were analysed. The shape of the Fast Fourier transform (FFT) is pictured in Figure 17. Results in Figure 17 contains a dissipation range, the inertial subrange with slope of −5/3, and the energy-containing range. The difference in the dissipation range and the energy-containing range between the regimes is caused by different Reynolds numbers.

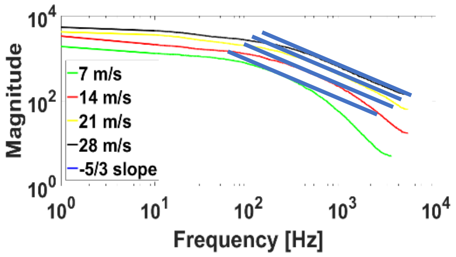

Fig. 17. Results obtained by FFT analysis for different velocity regimes

2.5 Pitot static tube Declination

Declination α [°] of the pitot static tube from the velocity vector direction and its influence on the flow velocity was measured. The L-type and S-type pitot static tubes were investigated for two regimes (mean velocity of 7 and 28 m/s). A schematic drawing of the pitot static tubes can be seen in Figure 18 and the experimental setup in Figure 19.

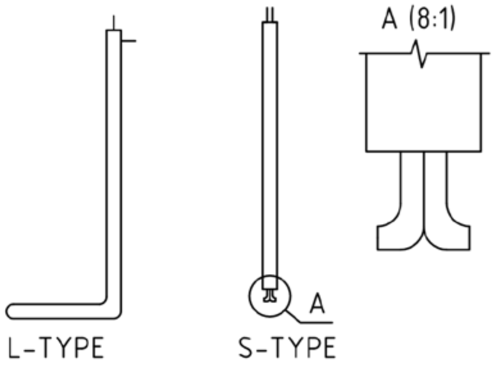

Fig. 18. L-type and S-type pitot static tubes design

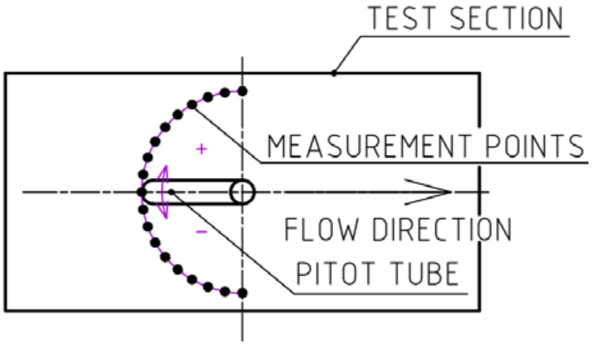

Fig. 19. L-type and S-type pitot static tube experimental setup

Both types of pitot static tubes are relatively insensible to the probe declination because the first declination derivative of velocity is zero when the declination reaches 0´°. As indicated in Figures 20 and 21, the characteristics are symmetrical. There are small asymmetries on mean velocity of 28 m/s; this asymmetry can be caused by the flow instability or inaccurate measurement. Velocities measured by the S-type Pitot static tube need to be calibrated by the factor of 0.84 according to the standard ČSN ISO 10780. Both S-type and L-type measured the velocity very precisely when there was no declination of the probe. A comparison with the industrial measurement system, QuadraTherm® 640i In-Line Mass Flow Meter, referred here as a “QuadraTherm”, can be also seen in Figures 20 and 21. The data obtained by QuadraTherm® 640i In-Line Mass Flow Meter are not symmetrical and the measurement system shows a sensitivity to the probe declination because the first declination derivative of velocity is not zero when the declination is 0 °. This asymmetrical behaviour is caused by non-symmetrical probe location of the measurement system. On the other hand, the measurement range of this industrial system is in the range of 1–300 m/s, and the system is very robust and stable for a wide velocity range. The system can be used in the flow with relatively large polluting particles because of robust probes. The system is able to measure the volume and mass flux.

According to ČSN ISO 10780 S and L-type pitot static tubes accuracy is under 3% of measurement value for declination in range of ±15 ° from velocity vector direction. For higher declination accuracy is under 5% of measurement value. QuadraTherm® 640i has an accuracy in range of ±0.5 of readings plus 0.5% of full scale, when the measured velocity is bellow 50% of full scale. Accuracy of QuadraTherm® 640i measuring the velocity above 50% of full scale is ±0.5 of readings. QuadraTherm® 640i is not suitable for measuring velocities bellow 150 m/s. The results in Figures 20 and 21 show a relatively good agreement with S and L-type Pitot static tubes for zero declination.

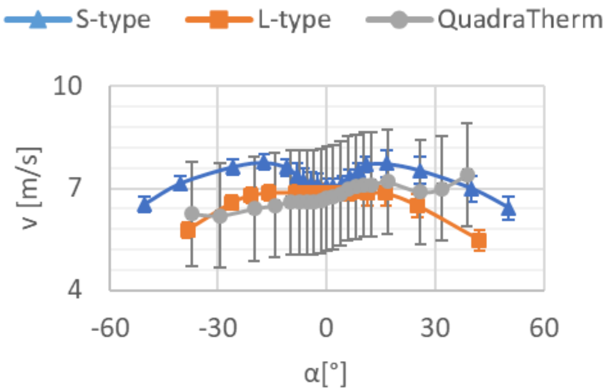

Fig. 20. S, L-type and QuadraTherm velocity probe declination measurement, mean velocity7 m/s

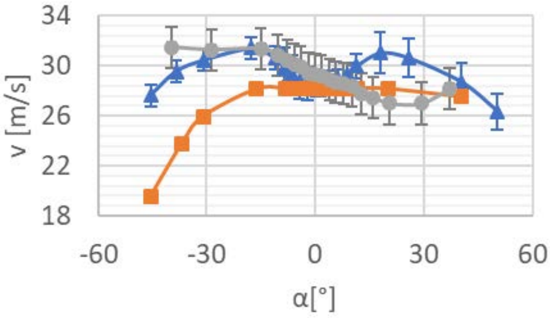

Fig. 21. S, L-type and QuadraTherm velocity probe declination measurement, mean velocity 28 m/s

3 CONCLUSIONS

The average velocity in the newly designed low-speed small-scale wind tunnel was measured by different velocity measurement techniques (PDA, LDA, CTA, and the pitot static tube.) PDA, LDA, CTA and pitot static tube experimental setups are briefly discussed in the first section. Velocity profiles in the test section are uniform across the cross-section area for all the assumed cases. A uniform flow is developed 15 mm from the test section sides. Turbulent intensity measured by PDA, LDA and CTA in the free stream is under 5% with an increase near the wall where the velocity gradients are present. Turbulent intensities measured by PDA and LDA show expectably higher values than for the CTA measurement system.

The uncertainties of PDA and CTA measurement systems was assessed to be 1% and 4.8%, respectively, and it is worse in the boundary layer region. Both techniques are in a good agreement for both the average velocity and the turbulent intensity.

Declination of different types of pitot static tubes (S and L-type) and its influence on the flow velocity measured was briefly discussed. The experimental setup is briefly described and the comparison with Industrial QuadraTherm® 640i is provided. The results show the independence of S and L-type Pitot static tubes of declination, and the probes have a symmetrical behaviour. The industrial probe shows a dependence on the probe declination and a non-symmetrical dependence on the probe declination. Systems measures the average velocity with relatively high accuracy when declination of the probes is 0 °.

The results obtained by different measurement systems are in a good agreement. For the velocity measurement in the transparent test section of the wind tunnel, the PDA measurement system can be readily used because of the measurement abilities and easy introduction of the measurement volume into the flow. Another advantage of PDA is non-intrusive measurement which does not disturb the flow in the test section.

Acknowledgements

The authors acknowledge the financial support from the project No. 18-15839S funded by the Czech Science Foundation and the project “Computer Simulations for Effective Low-Emission Energy engineering” funded as project No. CZ.02.1.01/0.0/0.0/16_026/0008392 by Operational Programme Research, Development and Education, Priority axis 1: Strengthening capacity for high-quality research and project No. RV9090000335 founded by Faculty of Mechanical Engineering, Brno University of Technology. Authors would like to express their gratitude to Radek Kalík, Provyko s.r.o, Petr Komp and Milan Hladký, KROHNE for their effective support during probes testing.

References

1. S. Mauro, S. Brusca, R. Lanzafame, F. Famoso, A. Galvagno, M. Messina, IJAER, **12**, pp. 13649-13662 (2017)
2. Rahman, Md. Ali, Md. Sidique, F. Pabel, IJERT, **3** (2014)
3. O. Almeida, F. Miranda, O. Neto, F. Saad, JATM, **10** (2018)

4 T. Kumaraswamy, V. V. S. Nikhil Bharadwaj, P. Garre, GJRE-D, **14** (2014)

5. Y. Dwivedi, B. PARVATHAVADHANI, N. Mishra, IJTP, **1**, pp. 14-23 (2012)
6. Y. Yeh, H. Z. Cummis, Appl. Phys. Lett., **4**,176 (1964)
7. A. Boutier, Laser Velocimetry in Fluid Mechanics, **21,** (2012)
8. E. D. Hirleman, Part. Part. Syst. Charact., **13**, pp. 59-67 (1996)
9. B. Husted, P. Peterson, I. Lund, G. Holmstedt, FIRE SAFETY J., **44**, pp. 1030-1045 (2009)
10. F. Lízal, J. Jedelský, K. Morgan, K. Bauer, J. Llop, U. Cossio, S. Kassinos, S. Verbanck, J. Ruiz-Cabello, A. Santos, E. Koch, Ch. Schnabel, Eur. J. Pharm. Science, **113,** pp. 95-131 (2018)
11. Glenn O. Brown, Third National Congress on Civil Engineering History and Heritage, pp. 360-366, (2001)
12. G. Comte-Bellot, ANNU REV FLUID MECH, **8**, pp. 209-231 (2003).
13. Knoblock, Frederick Delbridge (1939) Investigations on the applications of the hot wire anemometer for turbulence measurements. Dissertation (Ph.D.), California Institute of Technology. http://resolver.caltech.edu/CaltechETD:etd-04252008-094935
14. Zh. Zhang, LDA Application Methods - 2010, Laser Doppler Anemometry for Fluid Dynamics, pp. 224-226 (2010)
15. D. Quinn, A. Watts, T. Nagle, D. Lentink, R. Soc. Open sci., **4**, (2017)
16. Y. KOHAMA, R. KOBAYASHI, H. ITO, 28th Joint Propulsion Conference and Exhibit, (1992)
17. Particle Dynamic Analyser (PDA) User´s manual, Skovlunde, Denmark, Dantec Measurement Technology, 1992.
18. F. JØRGENSEN, How to measure turbulence with hot-wire anemometers: a practical guide. 1st edition. Dantec Dynamics A/S, pp. 40-45 (2001)

16. Y. KOHAMA, R. KOBAYASHI, H. ITO, 28th Joint Propulsion Conference and Exhibit, (1992)

17. Particle Dynamic Analyser (PDA) User´s manual, Skovlunde, Denmark, Dantec Measurement Technology, 1992.

18. F. JØRGENSEN, How to measure turbulence with hot-wire anemometers: a practical guide. 1st edition. Dantec Dynamics A/S, pp. 40-45 (2001)